UNIVERSITY OF SOUTHAMPTON

A HYBRID MICROWAVE HETERODYNE RECEIVER DESIGN FOR USE IN DISTRIBUTED FIBRE SENSING OF SPONTANEOUS BRILLOUIN BACKSCATTER

by Nicholas P. Lawrence

A thesis submitted for the degree of
MASTER OF PHILOSOPHY

FACULTY OF ENGINEERING AND APPLIED SCIENCE

DEPARTMENT OF ELECTRONICS AND COMPUTER SCIENCE

SEPTEMBER 2002

Errata

Name: LAWRENCE, N.P.

Qualification for which thesis is being submitted: Master of Philosophy

Year of submission: 2002

Page 82

X-axis of figure 4.2 should read:	Pulsewidth (s)
Y-axis of figure 4.2 should read:	P0crBr (pulsewidth)
	P0crRaabove30ns (sensinglength)
	P0crRabelow30ns (pulsewidth)

Page 135

Title of figure 5.35 should read:	Heated section (100ns)

Page 137

Title of figure 5.37 should read:	Heated section (40ns)

Page 138

Title of figure 5.38 should read:	Strained section (40ns)

UNIVERSITY OF SOUTHAMPTON

ABSTRACT

FACULTY OF ENGINEERING AND APPLIED SCIENCE
DEPARTMENT OF ELECTRONICS AND COMPUTER SCIENCE

Master of Philsophy

A HYBRID MICROWAVE HETERODYNE RECEIVER DESIGN FOR USE IN DISTRIBUTED FIBRE SENSING OF SPONTANEOUS BRILLOUIN BACKSCATTER

by Nicholas P. Lawrence

Optical fibre sensing has long made use of direct detection methods in order to detect a Brillouin backscatter signal which, due to its very nature, is able to divulge information pertaining to the temperature and strain being applied to an optical fibre over a distance of many tens of kilometres. As the resolution of both these measurands has improved, physical limits have been approached which have necessitated research into other forms of detection such as coherent detection. In this instance a weak backscatter signal is effectively amplified by an optical local oscillator signal generating a beat frequency at 11GHz with all the information needed for temperature and strain sensing remaining ever present. This beat frequency is then detected before being subsequently analysed. At the University of Southampton previous work on this detection method has proved fruitful with the upshot being that research in this area is now being carried out both in an academic and industrial environment.

The research conducted in this thesis takes what has been demonstrated in previous coherent detection of Brillouin backscatter at the University of Southampton and builds upon its weakest point, namely that of having a spatial resolution of only 20m as determined by the resolution bandwidth of the electronic spectrum analyser incorporated as the previous sensor's receiver.

In order to improve this spatial resolution the electronic spectrum analyser has needed to be removed from the fibre sensor and to be replaced with purpose built microwave electronics in the form of a hybrid microwave heterodyne receiver. This has meant a stage of microwave heterodyning being incorporated via this new receiver in order to bring the 11GHz beat frequency down to a more amenable 1GHz second beat frequency, still with all the information necessary for temperature and strain sensing remaining on this signal. The subsequent incorporation of a bandwidth-tuneable bandpass filter centred at 1GHz has then allowed for improved spatial resolution to be observed. This 1GHz intermediate frequency was chosen as components at this frequency have better specifications in terms of noise figure and gain flatness than those at a higher frequency.

Theoretical models have been developed for noise and signal to noise evaluation of this new optical fibre sensor both before and during construction.

Results are highlighted in this thesis which demonstrate that the new hybrid receiver is efficient and powerful in its ability to improve the spatial resolution of the coherent optical fibre sensing technique. Simultaneous sensing of strain and temperature at a section 20km distant along a sensing fibre has demonstrated a temperature and strain resolution of <7.3K and <190$\mu\varepsilon$ when employing the sensor for 10m spatial resolution sensing together with <9.5K and <240$\mu\varepsilon$ when employing it for 4m spatial resolution sensing.

Table of Contents

List of Illustrations

Acknowledgements

I would like to thank my supervisor, Dr.Trevor Newson, for his guidance and expertise during this period of research. I would also like to thank Dr. Arthur Hartog and Dr. Peter Wait for their assistance, gained through project meetings with them.

I am also thankful to my colleagues at the ORC, namely Mohamed Al-Ahbabi and Yuh-Tat Cho, with whom many ideas and discussions have been shared.

Friends at the ORC such as Denis Guilhot and Dr. Stuart Russell are also thanked for their assistance, both morally and technically.

Finally, special thanks is paid to Margot and my family for their unstinting encouragement during this research.

Glossary

AO	Acousto-Optic
AOM	Acousto-Optic Modulator
ASE	Amplified Spontaneous Emission
BPF	Bandpass Filter
COTDR	Coherent Optical Time Domain Reflectometry
CRN	Coherent Rayleigh Noise
CW	Continuous Wave
dB	Decibel
dBm	dBm denotes a logarithmic power scale with 1mW as its reference
DOFS	Distributed Optical Fibre Sensing/Sensor
EDFA	Erbium-Doped Fibre Amplifier
EMI	Electromagnetic Interference
LO	Local Oscillator
LPR	Landau-Placzek Ratio
OFS	Optical Fibre Sensor
OTDR	Optical Time Domain Reflectometry
SBS	Stimulated Brillouin Scattering
SRS	Stimulated Raman Scattering
SSPA	Solid State Power Amplifer
VCO	Voltage Controlled Oscillator
WDM	Wavelength Division Multiplexor
YIG	Yttrium Iron Garnet

Chapter 1 Introduction.

For many years now, the fundamental properties of optical fibre have been found to lend themselves to an operation whereby temperature and strain are readily able to be investigated along a fibre length. The technique used in order to carry out this investigative measurement is a branch of distributed optical fibre sensing and, during recent times has been the subject of great interest due to its ability to allow measurements to be taken of temperature and strain in places where previously this was not possible [1,2,3].

Since the optical scattering properties of the fibre itself are dependent on ambient temperature and strain this type of sensing effectively enables detection of the scattered light from such a fibre which, through analysis, gives information on the temperature and strain along the fibre as a function of distance. Moreover, the ability to carry out such measurements using just one end of the fibre, since both the backscattered light and pulse used to interrogate the environment under question travel down the same single sensing fibre, means that this type of sensor has been adopted over sensors previously studied where dual-end interrogation of the sensing fibre was required. This type of system naturally lends itself to temperature and strain measurement within dangerous or difficult environments. These may range from deep oil wells running far underground where measurements taken of the ambient temperature and strain can divulge clues as to whether the oil is ready for extraction or not to power cables in which hot spots caused by excessive demand of electricity during certain peak times can cause the cable in question to break connection hence causing great inconvenience to the consumer as well as vast additional expense for the power company owning the cable. There are many other possibilities for this type of sensor that are not so obvious. These include the measurement of strain in bridges where the sensing fibre could easily be housed within the concrete or steel frame taking the strain during adverse traffic or weather conditions as well as the measurement of strain in sailing boat masts where the ability to measure strain would allow preventative action to be taken so as port could be reached safely. Virtually any environment where temperature and strain are major influences can be interrogated and analysed using such a sensor. And although two measurands, namely temperature and strain, are the focus of many of today's sensing systems, there is no reason not to suppose that others may be sensed in the future.

The benefits of such a sensor, apart from the single end access already mentioned, include the fact that optical fibre is lightweight and flexible together with a small cross-sectional area as well as being relatively immune to electromagnetic interference (EMI). The low heat capacity per unit length makes it an ideal material for use in temperature sensing. Finally, the low loss of optical fibre allows long distance sensing to be performed over many kilometres.

Within the properties of optical fibres, the process of Brillouin scattering is significantly sensitive to allow for both temperature and strain measurements to be performed. In this scattering process both the intensity of the interrogated backscattered signal and the frequency shift due to the physical nature of the backscatter process are altered to varying degrees by these two measurands. Previously, optical time domain reflectometry (OTDR) has been employed to perform measurements on the state of an optical fibre; this process makes use of Rayleigh backscatter which in optical terms is the dominant backscatter process seen within any optical structure. As its presence is far more readily detectable than Brillouin backscatter this has posed problems in the past for temperature and strain measurements. However, high performance interferometers have allowed spontaneous Brillouin backscatter to be optically distinguished from Rayleigh backscatter with the inevitable result that as progress has been made on improving the state of the art as far as interferometers are concerned so improvements have been made to the resolution of temperature and strain as a function of distance along an optical fibre.

In 1998, a temperature error of 0.9K was demonstrated by Lees et al. for a spatial resolution of 3.5m and a sensing length of 16km [4]. For the purposes of temperature and strain sensing, the Brillouin frequency shift has been measured and calibrated using direct detection, heterodyne detection and Brillouin gain/loss methods. To date the best frequency shift results have been obtained using heterodyne detection. In 1996, Izumita et al. demonstrated a 20με resolution for a spatial resolution of 100m and a sensing length of 30km [5] by heterodyne detection of spontaneous Brillouin backscatter. To measure both temperature and strain simultaneously, however, the change in Brillouin backscatter power and the frequency shift imparted on the backscatter need to be

measured with reference to known quantities of backscatter power and frequency shift on an unheated and unstrained section of optical fibre.

With heterodyne work having been performed prior to this research [1,2] the principal aim of this work was to develop a new sensor which improves upon limitations previously experienced. Prior results [1] have demonstrated through simultaneous sensing a strain resolution of 100με together with a temperature resolution of 4K over a 30km sensing length. However these measurements have only demonstrated a spatial resolution of 20m. The work in this thesis was embarked upon to demonstrate that, through a new type of receiver system placed in the sensor still based on the heterodyne detection technique, spatial resolution could be improved upon without comprising on the other major parameters essential to optical distributed fibre sensing, namely sensing length together with temperature and strain resolution. Results from previous research [1,2] were used as goals together with an improvement in spatial resolution from 20m to 10m or less.

All heterodyne systems used in research prior to this thesis have been arranged for the Brillouin/optical local oscillator (OLO) beat frequency to lie within the detection bandwidth of a conventional receiver [6]. This was done by deriving both the pulses and the OLO from a single source and optically shifting one component in frequency; the use of two separate sources would result in inherent frequency instability. This thesis builds upon work carried out using heterodyne sensing at the 11GHz unshifted beat frequency by using a 20 GHz optical bandwidth detector together with a newly developed receiver based on microwave superheterodyne technology. Prior research has made use of a 26GHz electronic spectrum analyser effectively limiting the spatial resolution of any measurement made to 20m due to the 5MHz bandwidth intermediate frequency (IF) filter within the analyser itself. The development of the new superheterodyne receiver allows for a far wider IF bandwidth to be established allowing for greater resolution. Characterisation of the new receiver is important in analysing how the sensor works and this research has also taken this element into consideration. The replacement of the electronic spectrum analyser by the new superheterodyne receiver in the sensor hence establishes the sensor as being dual-heterodyne in nature as heterodyning both in the optical realm and microwave realm is seen to occur. The

ability to select components for inclusion into the new receiver allows for future upgrading at a relatively modest cost, something which has clearly not been available previously.

Chapter Two of this work is intended as an overview of the background to this research. A theory of optical heterodyning is presented with the view to enlightening the reader on the fundamental optical process made use of in this piece of work. The phenomena of Rayleigh, Raman and Brillouin scattering within an optical fibre are described as well as their characteristics and suitability for distributed sensing. A brief review of previous research into sensing techniques is also presented, with particular emphasis given to Brillouin-based sensors.

Chapter Three describes the components that were necessary in the construction of the sensor. Basic theory concerning the sensor is also embarked upon in this chapter including microwave superheterodyne theory and an example of how the sensor is used to collect data and interpret it. Emphasis in this chapter is given to the microwave receiver since the optical section of the fibre sensor uses constituents that have been discussed and analysed in previous research [3,4]. Indeed the optical section of the system, apart from a complete rebuild, does not significantly vary from that established in previous research at the university. Options available as to the type of microwave receiver design are demonstrated together with an overview of the various microwave components chosen in the final design.

Chapter Four focuses on the theoretical analysis of the sensor including the noise analysis necessary for the ability to determine through modelling the sensing capability of the new sensor. The different types of noise anticipated at the receiver are highlighted and where applicable estimates as to the performance are made. These estimates include signal to noise ratios together with those of frequency shift errors, noise on the backscatter signal and the expected output from the sensor.
Non-linear effects such as stimulated Raman scattering (SRS) and stimulated Brillouin scattering (SBS) are discussed and calculated for the new optical fibre sensor. Estimates of temperature and strain resolution for the new sensor are within this chapter.

Chapter Five can be perceived as putting the theory of Chapter Four into practice. The first section of this chapter deals with measurements made allowing for sensor performance to be verified together with measurements enabling for calibration of the sensor to be performed. Once again emphasis is given to the new microwave receiver since the optical section of the sensor has been well documented in prior work.

Work highlighted in previous chapters is brought to fruition in this chapter since the sensor is used to collect two sets of data both undetectable using previous heterodyne techniques. This data is detected from a heated and strained section placed at 20km down the sensing fibre. Naturally following on from this, the data is subsequently analysed and graphical information is generated for the effect of temperature and strain on the backscatter intensity and frequency shift seen to occur within the optical fibre.

Calibration coefficients showing the evolution of backscatter intensity and frequency shift as a function of temperature and strain are generated from this graphical information. Other information is also extracted through analysis of the detected data such as the Brillouin linewidth variation as a function of distance and as a function of temperature and strain. A calibration coefficient for the effect of temperature on linewidth is also found. Where applicable, brief comparisons are made between information extracted from the new sensor and information found during previous research.

Chapter Six takes information generated through this research and brings it together in a summarised form. Where appropriate, conclusions are drawn that enable comparisons to be generated between this work and previous work conducted. This then forms the basis of a discussion on future work using the sensor.

The work contained within this thesis consists primarily of the author's own research. Any material used from other sources in the production of this thesis is referenced accordingly.

References

[1] S.M.Maughan, H.H.Kee and T.P.Newson, 'Simultaneous Distributed Fibre Temperature and Strain Sensor Using Microwave Coherent Detection of Spontaneous Brillouin Backscatter', IOP, *Measurement Science and Technology*, 12, pp. 834-842, (February 2001)

[2] S.M. Maughan, "Distributed Fibre Sensing Using Microwave Heterodyne Detection of Spontaneous Brillouin Backscatter", Doctor of Philosophy Thesis, Department of Electronics and Computer Science, *University of Southampton*, (September 2001)

[3] T.R.Parker, M.Farhadiroushan, V.A.Handerek and A.J.Rogers, 'A Fully Distributed Simultaneous Strain and Temperature Sensor using Spontaneous Brillouin Backscatter', *IEEE Photonics Technology Letters*, Vol.9, No.7, pp.979-981, (1997)

[4] G. Lees, P. Wait and T. Newson, "Distibuted Temperature Sensing using the Landau-Placzek ratio", *Proc. ICAPT98, ICAPT98T234*, Ottawa, Ontario, Canada (July 1998)

[5] H. Izumita, T. Sato, M. Tateda and Y. Koyamada, "Brillouin OTDR Employing Optical Frequency Shifter Using Side-Band Generation Technique with High-Speed LN Phase Modulator", *IEEE Photonics Tehnology Letters*, Vol. 8, No. 12, pp. 1674-1676 (December 1996)

[6] K.Shimizu, T.Horiguchi, Y.Koyamada, T.Kurashima, 'Coherent Self-Heterodyne Brillouin OTDR for Measurement of Brillouin Frequency Shift Distribution in Optical Fibers', *Journal of Lightwave Technology*, Vol.12, No.5, pp 730-736, (1994)

Chapter 2 Distributed Optical Fibre Sensing.

As stated in Chapter One, distributed optical fibre sensing (DOFS) makes use of the properties of the optical fibre itself in order to allow for extraction of information about a measurand, such as temperature or strain, continuously along the length of the sensing fibre.

In a distributed fibre sensor, this measurand imposes a variation in the interrogating or probe signal as a continuous function of distance. The accuracy of the data returned by this process, most commonly seen in Optical Time Domain Reflectometry (OTDR), is limited by a receiving system's spatial resolution and the signal to noise ratio that is incumbent on it.

OTDR in itself forms the basis for the work to be performed in this research and as such it is informative to understand how the basic principle works.

2.1 Optical Time Domain Reflectometry

This type of distributed optical fibre sensing (DOFS) is the simplest of its kind and has been used for almost 30 years now. It is used to measure the optical loss continuously along a fibre under test [1]. It was first propsed by Barnoski and Jensen [2] in the mid 1970s and is today used for verifying the condition of virually all optical networks. Figure 2.1 demonstrates a typical optical time domain reflectometer (OTDR).

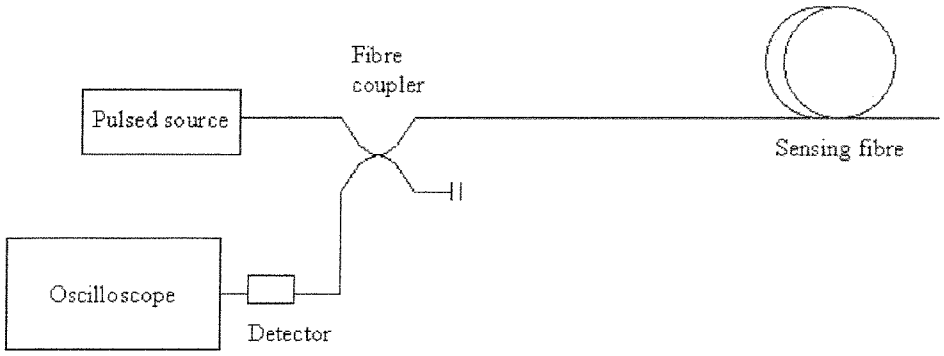

Figure 2.1 A Typical Optical Time Domain Reflectometer System.

In OTDR, a probe pulse is sent down the fibre and through the continuous interaction of this probe with the fibre itself, a profile of the state of the fibre can be obtained by measuring the backscattered light within the fibre's numerical aperture with the time between sending the pulse and receiving the backscatter corresponding to the distance along the fibre. In equation form this is given as,

$$x=(v_g t)/2=(ct)/2n \qquad \{2.1\}$$

if t=0 is set to be the time at which the first backscatter radiation is detected Here x is the distance along the fibre, v_g is the velocity of light within the fibre, t is the backscatter detection time, c is the velocity of light in vacuo and n is the average of the refractive index in the fibre.

The backscattered power, which is Rayleigh backscatter, detected at the input of the fibre as a function of time is [1]:

$$\text{Backscattered Power}=0.5\{P_{in}W_o\gamma_R\upsilon_g S\exp(-\upsilon_g\gamma_R t)\} \qquad \{2.2\}$$

where P_{in} is the input optical power to a single mode fibre, W_o is the input pulse width, υ_g is the group velocity of the pulse in the fibre, γ_R is the Rayleigh scattering coefficient, t is time after the pulse launch and S is the capture fraction of the backscattered signal within the numerical aperture.

In {2.2} S is the fraction of captured optical power and is given as,

$$S=(NA)^2/4n^2 \qquad \{2.3\}$$

where NA is the numerical aperture of the fibre.

For a pulse with an average power of 150mW and of 40nS duration the backscattered Rayleigh signal that can be expected at the front end of the fibre is typically of the order of 60nW or 64dB down on the input pulse. It is hence clearly desirable to send high optical pulse powers down the fibre in order to obtain the highest Rayleigh backscatter signal possible. However as will be seen later in Chapter 3 non-linear effects become a threshold limit to increasing the power exponentially effectively creating a power window for the OTDR sensor; too high a launched pulse power and non-linear effects occur; too low and the signal to noise ratio detected does not permit the distinction to be made between the backscatter signal and noise within the sensor itself.

The spatial resolution of an OTDR system is affected by both the input pulse duration and the detection bandwidth. For the work performed in this thesis a 40nS and 100nS pulse were used together with a 50MHz bandwidth detector. This is to ensure that all of the backscatter signal is captured with as little noise being detected as possible. The expressions for the spatial resolution implied by both the pulse width, ΔT, and detector bandwidth, $\Delta\nu$, individually are given below by Δx_{pulse} and $\Delta x_{detector}$ respectively,

$$\Delta x_{pulse}=(c\Delta T)/2n$$

$$\Delta x_{detector}=(c)/(4n\Delta\nu) \qquad \{2.4\}$$

for a flat gain bandwidth with instantaneous cut-off at $\Delta\nu$. With n=1.5 for standard silica telecommunications fibre, this gives,

$$\Delta x_{pulse}(m)=(\Delta T(ns))/10$$

$$\Delta x_{detector}(m)=(50)/(\Delta\nu(MHz)) \qquad \{2.5\}$$

However as will be seen later this is exacerbated with the use of microwave heterodyne detection since for both intensity changing sidebands to be captured the bandwidth must effectively be doubled once more.

For optimum signal to noise $\Delta x_{detector}=\Delta x_{pulse}$ and so a pulse length of ΔT requires a detector bandwidth of

$$\Delta\nu(MHz)=500/\Delta T(ns)$$

for a standard OTDR sensor or

$$\Delta\nu(MHz)=1000/\Delta T(ns) \qquad \{2.6\}$$

should the detection of both sidebands be required while using a microwave superheterodyne-based receiver as this work has done.

Many types of OTDR have used longer wavelength radiation at 1.6μm as it undergoes higher fibre bend loss so allowing for easy detection of damage in the interrogated fibre. However OTDRs at 1.55μm, with a longer sensing length due to the fibre loss being a minimum at this wavelength, have recently become more popular. The work performed in this research is predominantly based on sensors operating at 1.55μm.

Broadband sources such as light emitting diodes (LEDs) may also be used in OTDRs as the source signal although dispersion of this signal along the fibre causes the detected

backscatter pulse to be widened if long sensing lengths are being employed. This effectively reduces the spatial resolution of any such sensor at longer sensing lengths. A broadband signal does have one distinct advantage over a narrowband signal in that Coherent Rayleigh Noise (CRN) is not observed.

Coherent Rayleigh Noise, commonly known as 'fading noise', is observed as noise on the backscattered signal and is due to the coherent interference of a large number of scatter elements which generate random intensity fluctuations in the backscattrered signal. These effects can be overcome by either switching to a broadband source or averaging over a number of frequencies with a tuneable narrow linewidth source [3].

In this instance the backscattered signal generated at a particular frequency does not correlate with that at another frequency due to the backscattered signal being generated from the interference of different groups of scattering centres. Although evidently observable on Rayleigh backscattered signals, fading noise is not seen on Brillouin backscatter as the random phase fluctuations due to the spontaneous propagating density fluctuations result in the noise being averaged over the scatter elements.

Conventional OTDR may be improved upon by the use of coherent or heterodyne detection. Briefly described the backscattered signal can effectively be amplified to improve the signal to noise ratio of the sensor by mixing it with an optical local oscillator signal (OLO) with a fixed frequency difference between them known as the beat or intermediate frequency. Figure 2.2 demonstrates the principle.

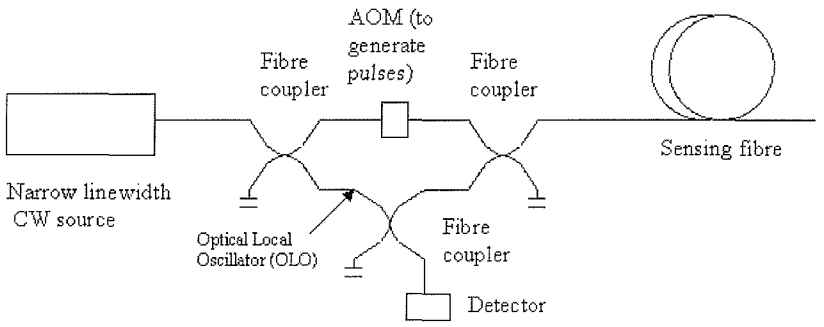

Figure 2.2 Coherent Optical Time Domain Reflectometry. This Forms the Basis of the Design Generated in This Research. A Frequency Shift (IF) is Generated by the Modulation of the AOM While Pulsing. Some of the Original CW Signal Acts as an OLO Signal.

It is usual to generate the OLO and sensing pulses used to obtain the backscattered signal from one single optical source wavelength with the acousto-optic modulator used to generate the pulses acting to generate the intermediate frequency between them. Optical mixing of the OLO and the backscattered signal on the photodetector results in a component I_S of the output current with an amplitude proportional to $(P_S P_{LO})^{1/2}$ where P_S is the power of the backscatter signal and P_{LO} is the power of the OLO. This component oscillates at the intermediate frequency.

This component of current is then converted to baseband through first selecting it with a bandpass filter centred on the intermediate frequency and then heterodyning it once again with a signal at the intermediate frequency to generate a final DC output.
The advantages of coherent detection over direct detection are that greater dynamic range of the sensor can be obtained since the OLO acts as an amplifier stage for the backscattered signal effectively boosting its intensity as shown by the useful current

component being proportional to $(P_S P_{LO})^{1/2}$. The disadvantage of such a sensor is that a narrow linewidth must be used hence provoking CRN as previously mentioned.

The Rayleigh backscatter itself, made use of in OTDR sensors, is insensitive to temperature and as such is not useable in a temperature and strain sensor. However, the temperature sensitive processes of both Brillouin and Raman scattering occur in addition to the Rayleigh backscatter, albeit at far lower powers as far as spontaneous scattering is concerned. Both Brillouin and Raman scattering, contrary to Rayleigh scattering , are inelastic three-wave interactions involving an incident wave, backscattered wave and thermal molecular vibrations within the fibre itself. These molecular vibrations, due to the energies involved, are deemed to be due to acoustic phonon interaction for Brillouin scattering while for Raman scattering they are due to optical phonon interaction. Since phonon density is, by its very nature, dependent on temperature so both Brillouin and Raman scattering can be considered for use in distributed temperature sensors, provided that distinction is made between these signals and the ever-present Rayleigh signal within any fibre sensor. In addition, the Brillouin scattering process may also be used to measure distributed tensile strain since the acoustic velocity at the region of the fibre being interrogated is dependent on this quantity [4].

2.2 Types of Scattering Interaction

The interaction of a pulse with an optical fibre is now considered in more detail with reference to the three differing types of backscatter mentioned above.

- Rayleigh Scattering

  Rayleigh scattering is relatively insensitive to changes in temperature, this scattering process results from inhomogeneities of a random nature occurring on a small scale compared with the wavelength of the pulse light used. It is the dominant intrinsic loss mechanism in the low absorption window between the ultraviolet and infrared absorption tails. The inhomogeneities mentioned above manifest themselves as refractive index fluctuations and arise from density and compositional variations which are

frozen into the glass lattice on cooling [5] [6]. The scattering mechanism is elastic in nature as no frequency shift is observed in the backscattered light to that of the incident probe pulse light.

Rayleigh scattering is used in OTDR systems for detection of damage and attenuation in fibres but is not able to measure strain, temperature or other measurands in conventional silica optical fibre.

- Raman scattering

Within any molecular structure quantised molecular vibrational modes or phonons are found to exist. These phonons can be either high frequency 'optical' phonons or low frequency 'acoustic' phonons. It is the interaction of any pulse sent down a fibre with these phonons that produces two types of inelastic scattering process. High frequency 'optical' phonon interaction results in Raman scattering with low frequency 'acoustic' phonon interaction resulting in Brillouin scattering. For the 'optical' phonons, lying at far higher frequencies than those of an 'acoustic' nature means that the inelastic Raman scattering process creates an effective gain in the fibre medium which occurs, for fused silica, at $440cm^{-1}$ away from the wavelength of the incident light or approximately 13THz away from an incident wavelength of 1550nm [7]. In silica glass, Raman scattering occurs over a wide range of frequencies. This is due to the fact that molecules in a glass lattice are non-crystalline in nature, leading to different vibrational energies for different groups of molecules within the glass structure.

Both frequency upshifted and downshifted scattering processes known respectively as anti-Stokes and Stokes shifting can result due to the inelastic nature of the scattering process. This is demonstrated in figure 2.3.

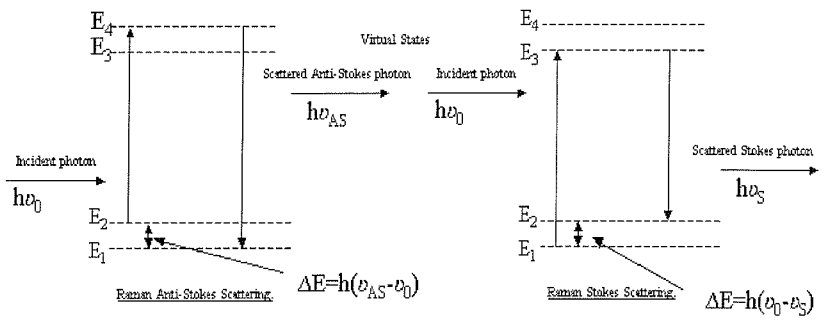

Figure 2.3 Raman Anti-Stokes and Stokes Scattering.

When anti-Stokes shifting occurs, the photon resulting from the scattering process has more energy, hence a higher frequency, than the incident photon. The converse is true for Stokes shifting. It is apparent that anti-Stokes shifting is far less likely to occur due to the fact that higher energy states must already be occupied by molecules in the interrogated material for this process to manifest itself. With the population density of states being controlled by the phonon distribution that varies with increasing or decreasing temperature, it is this thermal sensitivity which permits the use of Stokes/anti-Stokes Raman backscattered signals in distributed temperature sensing systems; an absolute temperature measurement being able to be made by taking the ratio of the Stokes to anti-Stokes components [6].

- Brillouin Scattering [7,8].

Brillouin scattering results from what may be regarded as the modulation of light through thermal molecular vibrations or acoustic waves within a fibre which cause a periodic change of refractive index along it. This pump-induced index grating scatters the pump light through Bragg diffraction. The resulting backscattered light, through a Doppler shift associated with the index grating moving at the acoustic velocity, undergoes a frequency shift. Hence, quantum mechanically, an incident photon in this scattering process produces a phonon, or acoustic vibrational mode, of acoustic frequency as well as a scattered photon. This produces an optical frequency shift which varies with the scattering angle because the frequency of the sound wave varies with acoustic wavelength. This frequency shift, for an unstrained, unheated silica fibre and using a pulse probe in the 1550nm low-loss window, is of the order of 11GHz. Only when the incoming optical wave is phase matched to the acoustic wave does Bragg reflection occur satisfying {2.7} resulting in Brillouin scattering.

$$2n\lambda_a \sin(\theta/2)=\lambda_p \qquad \{2.7\}$$

where n is the refractive index in the fibre, λ_a and λ_p are the acoustic and pump wavelengths respectively and θ is the angle between the incident and scattered light as shown in figure 2.4.

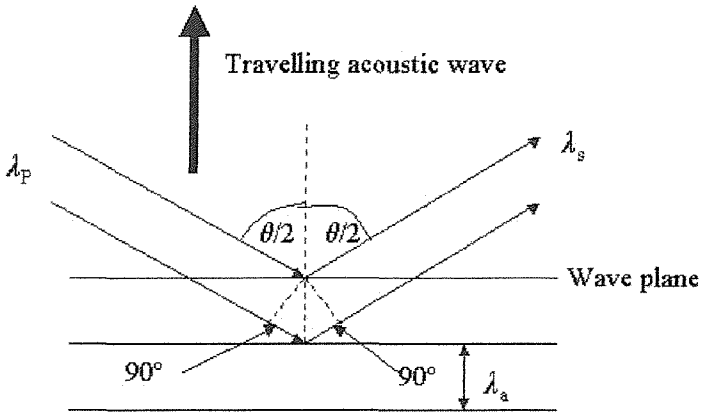

Figure 2.4 Brillouin Scattering From An Acoustic Wave.

Since energy and momentum must be conserved,

$$\omega_a=\omega_p-\omega_s$$

$$\mathbf{k}_a=\mathbf{k}_p-\mathbf{k}_s \qquad \{2.8\}$$

where ω_p and ω_s are the frequencies and $\mathbf{k}_p$ and $\mathbf{k}_s$ are the wave vectors of the pump and Stokes waves, respectively. The frequency ω_a and the wave vector $\mathbf{k}_a$ of the acoustic wave satisfy the dispersion relation,

$$\omega_a=|\mathbf{k}_a|v_a=2v_a|\mathbf{k}_p|\sin(\theta/2) \qquad \{2.9\}$$

where θ is the angle between the pump and Stokes waves, v_a is the acoustic velocity in the fibre and $|\mathbf{k}_p|$ is approximately equal to $|\mathbf{k}_s|$. Hence the frequency shift is dependent on the scattering angle. It is maximum in the backward direction and zero in the forward direction.

Hence in the backward direction, the Brillouin frequency shift is given as,

$$\nu_b=\omega_a/2\pi =2n\nu_a/\lambda_p \qquad \{2.10\}$$

For n=1.46, ν_a=5960m/s, the shift is as mentioned before around 11GHz for a pump wavelength of 1550nm.

The fact that Brillouin scattering is caused by thermally generated acoustic waves gives it its temperature and strain dependence allowing for these measurands to be measured.

Brillouin scattering is approximately 15dB weaker than Rayleigh scattering but is over two orders of magnitude greater than Raman scattering[7].

The three fundamental parameters of Brillouin scattering that need to be considered for distributed temperature and strain measurements are:

- Brillouin natural linewidth. Any change in temperature or strain along a fibre will produce a new backscatter signal which is shown to be of typically 35MHz [9] in width and with an optical frequency shift determined by the temperature and strain at the region along the fibre from where the backscatter originated. The Brillouin natural linewidth provides a measure of the phonon lifetime and it has been demonstrated that this linewidth does not vary with strain and its temperature dependence is small, being of the order of –0.1MHz/K [10].

- The variation of scattering coefficient can be considered to be caused primarily by its direct dependence on temperature. There is a slight variation in the scattering coefficient with applied strain, due to the change in fibre elastic properties.

- The Brillouin frequency shift variation with temperature and strain follows from {2.10} and a matrix has been generated which gives the change in

Brillouin frequency shift and backscattered power with strain and temperature.

In order to determine applied temperature, and strain on a region of optical fibre, the following coefficients give the change in Brillouin frequency shift due to applied heating or strain and likewise the change in Brillouin backscatter power,

$$\Delta\nu_b = C_{\nu b\varepsilon}\Delta\varepsilon + C_{\nu bT}\Delta T$$
$$\Delta P_b = C_{Pb\varepsilon}\Delta\varepsilon + C_{PbT}\Delta T \qquad \{2.11\}$$

where

$\Delta\nu_b$ =change in Brillouin frequency shift due to applied heat and strain

ΔP_b =change in Brillouin backscatter intensity due to applied heat and strain

$\Delta\varepsilon$=applied strain (in microstrain)

ΔT=applied temperature

$C_{\nu b\varepsilon}$ =coefficient for change of Brillouin frequency shift with strain=0.048MHz/$\mu\varepsilon$ [11]

$C_{\nu bT}$ =coefficient for change of Brillouin frequency shift with temperature=1.1MHz/K [11]

$C_{Pb\varepsilon}$ =coefficient for change of Brillouin backscatter intensity with strain= -0.000903%/$\mu\varepsilon$ [12]

C_{PbT} =coefficient for change of Brillouin backscatter intensity with temperature=0.32%/K [13]

The equations given in {2.11} can be inverted in their matrix form in order to give the applied temperature and strain provided that $C_{v b \varepsilon} C_{P b T} \neq C_{v b T} C_{P b \varepsilon}$ [11].

$$\Delta\varepsilon\ (\mu\varepsilon) = (|C_{v b \varepsilon} C_{P b T} - C_{P b \varepsilon} C_{v b T}|)^{-1} [(C_{P b T} \Delta\nu_b) + (-C_{v b T} \Delta P_b)]$$

$$\Delta T\ (K) = (|C_{v b \varepsilon} C_{P b T} - C_{P b \varepsilon} C_{v b T}|)^{-1} [(-C_{P b \varepsilon} \Delta\nu_b) + (C_{v b \varepsilon} \Delta P_b)] \qquad \{2.12\}$$

The associated errors or resolutions of applied temperature and strain are given as [9],

$$|\ \delta\Delta\varepsilon\ (\mu\varepsilon)| = (|C_{v b \varepsilon} C_{P b T} - C_{P b \varepsilon} C_{v b T}|)^{-1}\ [(|C_{P b T}| \delta\Delta\nu_b) + (|C_{v b T}|\ \delta\Delta P_b)]$$

$$|\ \delta\Delta T\ (K)| = (|C_{v b \varepsilon} C_{P b T} - C_{P b \varepsilon} C_{v b T}|)^{-1}\ [(|C_{P b \varepsilon}| \delta\Delta\nu_b) + (|C_{v b \varepsilon}|\ \delta\Delta P_b)] \qquad \{2.13\}$$

where δ denotes the measured error on the variable in question.

2.3 Brillouin Backscatter Detection Methods

To date, several designs of Brillouin-based distributed sensing systems have been created ranging from direct optical detection using Mach-Zehnder Interferometry [14] [15] [16] to systems incorporating conversion of the backscattered light signal to an electronic signal through optical heterodyning and subsequent lightwave conversion [17]. With the signal then down at microwave frequencies the signal can then be detected or microwave heterodyned and then processed [18].

In brief, using Mach-Zehnder interferometry, use has been made of the Landau-Placzek ratio [13]; this being merely the ratio of a Rayleigh backscatter signal with a Brillouin backscatter signal in order to compensate for splice/bend losses.

The Landau-Placzek ratio can be used in determining applied temperature (if the backscatter frequency shift is known) and strain on a fibre by firstly generating two Brillouin backscattered signals from a fibre, one with the probe pulse frequency tuned to the minimum of a Mach-Zehnder transfer function and the other with it tuned to the maximum of a Mach-Zehnder transfer function [19]. The two backscatter profiles

hence generated are then added together to form a profile that represents the intensity changes of the Brillouin signal along the fibre and is independent of any frequency shift. Then dividing this new profile by a Rayleigh backscatter profile, so as to create a Landau-Placzek ratio, allows a profile dependent only on backscatter intensity changes to be made.

To obtain frequency shift information, the profile generated with the probe pulse frequency tuned to the minimum of the Mach-Zehnder transfer function is also normalised by the Rayleigh profile and is subsequently normalised again by the profile dependent only on backscatter intensity changes described above. The resulting profile is hence intensity independent.

Using the coefficients given above for calculating applied heat and strain on a fibre given the LPR intensity change and backscatter frequency shift allows for an accurate picture of the state of a fibre to be built.

The sensor that is the basis of this particular research is the optical coherent detector used for OTDR measurements as described in 2.1. The sensor in this research obviously differs from any OTDR sensor in that Brillouin backscatter, due to its sensitivity to temperature and strain, is being detected rather than Rayleigh backscatter.

It is informative to consider the theory behind optically heterodyned detection systems as this was used in order to generate the Brillouin backscattered signal that the new microwave receiver, covered more fully in subsequent chapters, had been designed to detect with an improved spatial resolution to that previously demonstrated.

2.4 Theory Of Optical Heterodyning

With the advantages of coherent detection already given in 2.1 the following is a brief theory of optical heterodyning in order to introduce some of the more pertinent principles involved in this process [8].

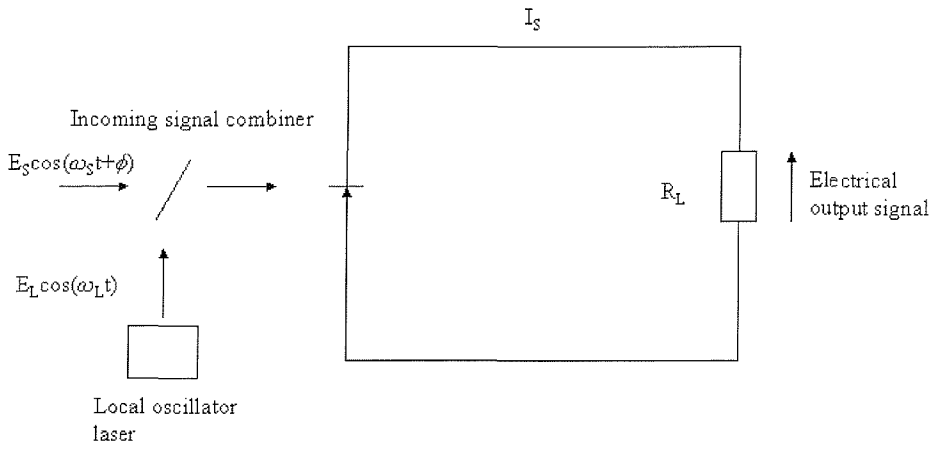

Figure 2.5 Basic Coherent Receiver Model

Figure 2.5 demonstrates a basic coherent receiver model used in optical heterodyning applications. The low level incoming signal field e_S is combined with a second much larger signal field e_L derived from a local oscillator laser. It is assumed that the electromagnetic fields obtained from the two lasers (i.e. the incoming signal and local oscillator devices) can be represented by cosine functions and that the angle $\phi(t)=\phi_S(t)-\phi_L(t)$ represents the phase relationship between the incoming signal phase $\phi_S(t)$ and the local oscillator signal phase $\phi_L(t)$ defined at some arbitrary point in time. Hence as depicted in figure 2.5 the two fields may be written as [20]:

$$e_S=E_S\cos(\omega_S t+\phi(t))$$

and

$$e_L=E_L\cos(\omega_L t) \qquad \{2.14\}$$

where E_S is the peak incoming signal field and ω_S is its angular frequency, E_L is the peak of the local oscillator field and ω_L is its angular frequency and $\phi(t)$ is the phase

angle between the two signals. The information in this instance is contained in the variation of E_S.

For heterodyne detection , the local oscillator frequency ω_L is offset from the incoming signal frequency ω_S by an intermediate frequency (IF) such that

$$\omega_S=\omega_L+\omega_{IF} \qquad \{2.15\}$$

where ω_{IF} is the angular frequency of the IF. The IF is designed to fall within the radio frequency region and for this research is based at 11GHz. By contrast, within homodyne detection there is no offset between ω_S and ω_L and hence $\omega_{IF}=0$. In this case the combined signal is therefore recovered in the baseband.

In the case of both heterodyne and homodyne detection the optical detector produces a signal photocurrent I_P which is proportional to the optical intensity (i.e. the square of the total field for the square law photodetection process) so that

$$I_P \propto (e_S + e_L)^2 \qquad \{2.16\}$$

Substitution in {2.16} from equations {2.13} and {2.14} gives

$$I_P \propto [\, E_S\cos(\omega_S t+\phi) + E_L\cos(\omega_L t)]^2 \qquad \{2.17\}$$

Assuming perfect optical mixing, expansion of the right hand side of the expression shown in {2.17} gives

$$\begin{aligned}&[E_S^2\cos^2(\omega_S t+\phi) + E_L^2\cos^2(\omega_L t)+2E_SE_L\cos(\omega_S t+\phi(t))\cos(\omega_L t)]\\ &=[0.5E_S^2 + 0.5E_S\cos(2\omega_S t+\phi(t))\\ &+0.5E_L^2+0.5\cos(2\omega_L t)+E_SE_L\cos(\omega_S t+\phi(t)-\omega_L t) +\\ &E_SE_L\cos(\omega_S t+\phi(t)+\omega_L t)] \qquad \{2.18\}\end{aligned}$$

Removing the higher frequency terms oscillating near the frequencies of $2\omega_S$ and $2\omega_L$,which are beyond the response of the detector and therefore do not appear in its output, gives

$$I_P\propto[0.5E_S^2 + 0.5E_L^2 + E_SE_L\cos(\omega_St-\omega_Lt+\phi(t))] \qquad \{2.19\}$$

Then recalling that the optical power contained within a signal is proportional to the square of its electrical field strength, {2.19} may be written as

$$I_P\propto[P_S + P_L + 2\{(P_SP_L)^{0.5}\}\cos(\omega_St-\omega_Lt+\phi(t))] \qquad \{2.20\}$$

where P_S and P_L are the optical powers in the incoming signal and local oscillator signal respectively.

Furthermore, a well known relationship exists between the output photocurrent from an optical detector and the incident optical power of the form [8]

$$I_P= P_O.\eta e/(hf) \qquad \{2.21\}$$

where I_P is the detected photocurrent, P_O is the incident optical power, η is the quantum efficiency of the photodetector, e is the charge of an electron, h is Planck's constant and f is the optical frequency of the photon.

Hence {2.20} becomes

$$I_P=\{\eta e[P_S + P_L + 2\{(P_SP_L)^{0.5}\}\cos(\omega_St-\omega_Lt+\phi(t))]\}/hf \qquad \{2.22\}$$

When the local oscillator signal is much larger than the incoming signal, the third ac term in {2.22} may be distinguished from the first two dc terms and I_P can be replaced by I_S where

$$I_S=\{\eta e[2\{(P_SP_L)^{0.5}\}\cos(\omega_St-\omega_Lt+\phi(t))]\}/hf \qquad \{2.23\}$$

{2.23} allows the two coherent detection strategies to be considered. For heterodyne detection $\omega_S \gamma \omega_L$ and substituting from {2.15} gives

$$I_S=\{\eta e[2\{(P_S P_L)^{0.5}\}\cos(\omega_{IF}t+\phi(t))]\}/hf \qquad \{2.24\}$$

indicating that the output from the photodetector is centred on an intermediate frequency. This IF is stabilised by incorporating the local oscillator laser in a frequency control loop. This is however not necessary should the local oscillator signal be from the same source as the incoming signal since both signals in this instance will be subject to the same changes. The stabilised IF current is usually separated from the dc current by filtering prior to electrical amplification and demodulation.

For the special case of homodyne detection, however, $\omega_S=\omega_L$, and so {2.23} reduces to

$$I_S=\{\eta e[2\{(P_S P_L)^{0.5}\}\cos(\phi(t))]\}/hf \qquad \{2.25\}$$

or

$$I_S=[2R\{(P_S P_L)^{0.5}\}\cos(\phi(t))] \qquad \{2.26\}$$

where R is the responsivity of the optical detector. In this case the output from the photodiode is in the baseband and the local oscillator laser needs to be phase locked to the incoming optical signal.

It may be observed from the expressions given in {2.24} &{2.25} that the signal photocurrent is proportional to $P_S^{0.5}$ rather than P_S as in the case of direct detection. Moreover, the signal photocurrent is effectively amplified by a factor $P_L^{0..5}$ proportional to the local oscillator field. This local oscillator gain factor has the effect of increasing the optical signal level without affecting the receiver preamplifier thermal noise or the photodetector dark current noise; hence the reason why coherent detection provides improved receiver sensitivities over direct detection. However, this effect is limited by relative intensity noise, (RIN), which becomes the dominant noise for local oscillator powers above a value dependent on the type of laser source being used. This is covered in more detail in the noise analysis in Chapter 4.

The requirement for coherence between the incoming signal and local oscillator signals in order to obtain coherent detection is important. For successful mixing to occur, some correlation between the two signals in figure 2.5 must exist. Care must be taken to ensure that this is the case when two separate laser sources are employed to provide the signal and local oscillator beams. It may be noted that this problem, as mentioned earlier, is reduced when a single source is used with an appropriate path length difference as, for example, when taking measurements by interferometric techniques.

Prior to the observation of RIN becoming the dominant noise source above a certain level of local oscillator power, which can be attributed in this thesis to research undertaken by P.C.Wait, local oscillator quantum noise was taken as the dominant noise source in the case of coherent detection where the local oscillator signal power is much greater than the incoming backscattered signal power. It is instructive to include this noise in this instance since this was used as the limiting noise for much of the early work in this thesis. In the limit of the local oscillator power far exceeding that of the incoming backscattered power the quantum noise may be expressed as shot noise where the mean square shot noise current from the local oscillator is given by

$$\text{Mean of } (i_{SL}^2)=2eBI_{PL} \qquad \{2.27\}$$

Where B is the receiver bandwidth. Through substitution of {2.21} into{2.27}, while remembering that in this instance the photocurrent generated by the local oscillator signal is assumed to be by far the major contribution to the photocurrent, gives

$$\text{Mean of } (i_{SL}^2)=2e^2\eta P_L B/hf \qquad \{2.28\}$$

The detected signal power S being the square of the average signal photocurrent (assuming a unity gain device) is given as,

$$S=(\eta e/hf)^2 P_S P_L \qquad \{2.29\}$$

Hence the SNR for the ideal heterodyne detection receiver when the local oscillator power is large (ignoring any preamplifier thermal noise or photo detector dark current noise terms) may be obtained as

$$(S/N)_{het\text{-}lim}=[(\eta e/hf)^2 P_S P_L]/(2e^2\eta P_L B)/hf$$
$$=\eta P_S/hf2B$$
$$=\eta P_S/hfB_{IF} \qquad \{2.30\}$$

Equation {2.30} provides the so-called shot noise limit for optical heterodyne detection in which the amplifier bandwidth B_{IF} is assumed to be equal to 2B or twice the receiver bandwidth (constituting the maximum bandwidth requirement for optical heterodyne detection) [21]. It is also interesting to note that this heterodyne shot noise limit corresponds to the quantum noise limit for analogue direct detection. Optical heterodyning allows a much closer approach to this limit than direct detection due to the amplifying effect of the local oscillator on the backscatter signal.

Homodyne detection, where the signal received and local oscillator signal are of the same frequency, effectively provides a 3dB improvement on the heterodyne shot noise floor limit. This is because the receiver bandwidth can be reduced from B_{IF} to just B as the output signal from the photo detector appears in the baseband when using the homodyne scheme. Hence the SNR limit for optical homodyne detection is

$$(S/N)_{hom\text{-}lim}=\eta P_S/hfB \qquad \{2.31\}$$

Although homodyne detection exhibits an apparent 3dB improvement in the shot noise limit over heterodyne detection, the need to effectively perfectly match the incoming signal and local oscillator signal make this type of system difficult to operate correctly in reality.

2.5 Conclusions

In this chapter an introduction to the theoretical background behind the research has been conducted in order to introduce the reader to some of the issues that need to be understood if an effective distributed fibre optic sensor is to be built. The theory of optical backscatter has been introduced along with an insight into optical heterodyning theory. An equation for a shot noise limit has been given, this being the defining noise limit that was used in this research before the observation made by P.C.Wait that RIN becomes the dominant noise source for local oscillator powers above a certain level.

2.6 References

[1] S.D.Personick, 'Photon-probe- An optical-fiber time domain reflectometer', *Bell System Technical Journal*, Vol.56, No.3, pp.355-366, (1977)

[2] M.K. Barnoski and S.M. Jensen, 'Fiber waveguides: a novel technique for investigating attenuation characteristics', *Applied Optics*, Vol.15, No.9, pp.2112-2115 (September 1976)

[3] K.Shimizu, T.Horiguchi, Y.Koyamada, 'Characteristics and Reduction of Coherent Fading Noise in Rayleigh Backscattering Measurement for Optical Fibers and Components', *Journal of Lightwave Technology*, Vol.12, No.5, pp 730-736, (1994)

[4] M.Kamikatano, H.Sawano, M.Miyamoto and N.Sano, 'Fiber strain measurement in optical cables employing Brillouin gain analysis', *Proc. IWCS '92,* pp 176-182, Reno, (1992)

[5] F.L.Galeener, J.C.Mikkelsen, R.H.Geils and W.J.Mosby, 'The relative Raman cross section of vitreous SiO_2, GeO_2, B_2O_3 and P_2O_5', *Applied Physics Letters*, Vol.32, No.1, pp.34-36, (1978)

[6] J.Schroeder, R.Mohr, P.B.Macedo and C.J.Montrose, 'Rayleigh and Brillouin scattering in K_20-SiO_2 glasses', *Journal of American Ceramic Society*, Vol.56, No.10, pp.131, (1973)

[7] G.P.Agrawal, 'Nonlinear Fiber Optics. Second Edition', *Academic Press*, ISBN 0-12-045142-5, 1995

[8] J.M. Senior, 'Optical Fiber Communications: Principles and Practice. Second Edition', *Prentice Hall International Series In Optoelectronics*, ISBN 0-13-635426-2, 1992.

[9] S.M. Maughan, "Distributed Fibre Sensing Using Microwave Heterodyne Detection of Spontaneous Brillouin Backscatter", Doctor of Philosophy Thesis, Department of Electronics and Computer Science, *University of Southampton*, (September 2001)

[10] T.Kurashima, T.Horiguchi and M.Tateda, 'Thermal effects of Brillouin gain spectra in single-mode fibers', *IEEE Photonics Technology Letters*, Vol.2, No.10, pp. 718-720, (1990)

[11] T.R.Parker, M.Farhadiroushan, V.A.Handerek and A.J.Rogers, 'A Fully Distributed Simultaneous Strain and Temperature Sensor using Spontaneous Brillouin Backscatter', *IEEE Photonics Technology Letters*, Vol.9, No.7, pp.979-981, (1997)

[12] K.De Souza, P.C.Wait and T.P.Newson, 'Characterisation of Strain Dependence of the Landau-Placzek ratio for distributed sensing', *Electronics Letters*, Vol.33, No.7, pp. 615-616, (1997)

[13] P.C.Wait and T.P.Newson, 'Landau-Placzek ratio applied to Distributed Fibre Sensing', *Optics Communications*, Vol.122, No.4-6, pp. 141-146, (1996)

[14] H.H.Kee, G.P.Lees, T.P.Newson, 'Technique for measuring distributed temperature with 35cm spatial resolution utilising the Landau-Placzek ratio', *Photonics Technology Letters*, Vol.12 (7), pp.873-5, (2000)

[15] H.H.Kee, G.P.Lees, T.P.Newson, 'An all-fiber system for simultaneous interrogation of distributed strain and temperature sensing using spontaneous Brillouin scattering', *Optics Letters*, Vol.25 (10), pp.695-697, (2000)

[16] H.H.Kee, G.P.Lees, T.P.Newson, 'Simultaneous independent distributed strain and temperature measurements over 15km using spontaneous Brillouin scattering', *ISAP 2000 Glasgow,* (22-24 May 2000)

[17] K.Shimizu, T.Horiguchi, Y.Koyamada, T.Kurashima, 'Coherent Self-Heterodyne Brillouin OTDR for Measurement of Brillouin Frequency Shift Distribution in Optical Fibers', *Journal of Lightwave Technology*, Vol.12, No.5, pp 730-736, (1994)

[18] S.M.Maughan, H.H.Kee and T.P.Newson, 'Simultaneous Distributed Fibre Temperature and Strain Sensor Using Microwave Coherent Detection of Spontaneous Brillouin Backscatter', IOP, *Measurement Science and Technology*, 12, pp. 834-842, (February 2001)

[19] H.H.Kee, "The Design and Application of Optical Sources for Distributed Fibre Sensing Systems", Doctor of Philosophy Thesis, Department of Electronics and Computer Science, *University of Southampton*, (September 2001)

[20] D.W. Smith, 'Coherent fiberoptic communications', *Laser Focus*, pp. 92-106, November 1985

[21] T.Okoshi, 'Ultimate performance of heterodyne/coherent optical fiber communications', *Journal of Lightwave Technology*, LT-4 (10), pp.1556-1562, 1986

Chapter 3 Development of a Coherent Brillouin Sensor Incorporating Microwave & Optical Components.

3.1 Introduction

The emphasis of this chapter will be to describe the optical and electrical components required within the construction of an optical fibre sensor demonstrating coherent detection of spontaneous Brillouin scattering at 11GHz. Heterodyne theory used in the application of this design will also be investigated along with a description of how useful information concerning the measurements of Brillouin power and frequency shift can be extracted.

Both the advantages and disadvantages of the system developed during this research will be discussed with regard to systems that have previously been developed, both here at the university or elsewhere in other establishments.

To give an idea of the optical wavelengths that are considered in this thesis, figure 3.1 shows a typical spontaneous backscatter spectrum including the Rayleigh and both Brillouin components. The total Brillouin power is typically a factor of approximately 30 smaller than the Rayleigh power [1].

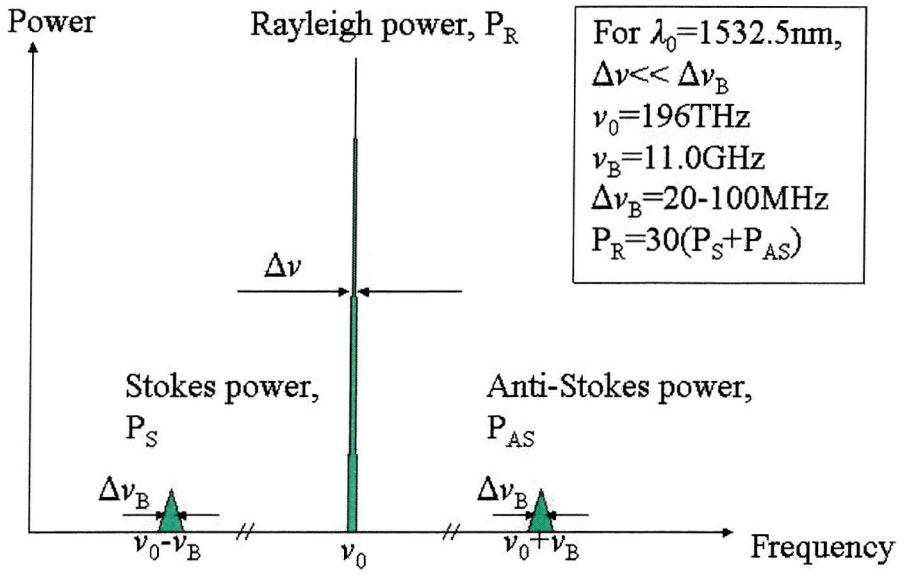

Figure 3.1 A Typical Spontaneous Backscatter Spectrum Including the Rayleigh and Both Brillouin Components.

From {2.10}, it can be seen that, for a given incident wavelength, the Brillouin frequency shift depends solely upon the acoustic velocity and fibre refractive index. In turn, these two quantities are dependent upon both intrinsic characteristics such as fibre composition and environmental factors such as temperature and strain. The intensities of Brillouin scattered waves are also temperature and strain dependent. Brillouin intensity is given by the formula [2],

$$I_B = [I_R T] / T_F[\rho(\nu_A^2)B_T - 1] \qquad \{3.1\}$$

where I_B and I_R are respectively the Brillouin and Rayleigh intensities, T_F is the fictive temperature of the glass, ρ is the density, B_T is the isothermal compressibility, ν_A is the acoustic velocity and T is the absolute temperature. It can be seen in this equation that the Brillouin intensity is explicitly temperature-dependent, but additional temperature and also strain effects also exist via the dependence of the density and acoustic velocity on these quantities.

3.2 Why Optically Heterodyne The Backscatter Signal Down To A Microwave Beat Frequency?

There are several advantages to detection of Brillouin backscatter at microwave frequencies. These can be identified as:

- Optical heterodyning is a means of improving the SNR at the front end of a detection system in order that greater resolution can be achieved providing a more accurate representation of strain and temperature along the length of an optical fibre. This is achieved by the optical LO power effectively acting as an amplifier for the backscattered signal with the amplification factor being [3],

$$2\sqrt{(P_{BackSig}P_{LO})} \qquad \{3.2\}$$

  where $P_{BackSig}$ is the backscattered optical signal and P_{LO} is the optical local oscillator signal.

- Optical heterodyning then allows detection to be continued in the microwave realm after lightwave conversion to an electrical signal as the backscatter signal is now in a frequency range between 10.5-11.5GHz, a range easily handled by modern electronic spectrum analysers.

- Any optical heterodyne detection system used will have a good gain flatness typically less than 1dB over the entire frequency range of interest (~700MHz), since this is only a small proportion of the whole detector bandwidth.

- The beat frequency is shifted away from any local oscillator self-beat noise[4], which is prevalent at low frequencies.

- Independent measurement of both Stokes and and anti-Stokes backscatter is possible since both beat frequencies lie within the detector bandwidth. If a first order acousto-optic modulator or AOM is used as a pulse modulator, the Stokes an anti-stokes separation will be twice the AOM frequency shift.

- Any optics incorporated in the design of an optically heterodyned system is simplified and frequency-stable since optical frequency shifting of 11GHz is not required.

3.3 Work Carried Out Prior To This Research

The university, prior to this research, has employed a method of optically heterodyning the backscatter signal which has yielded extremely good results. The system, as it stood, made use of a modern electronic spectrum analyser, in place of the microwave heterodyne receiver shown in figure 3.2, as the receiver for the backscatter signal after it had first been converted to an electrical signal via a lightwave detector. A typical representation of a modern electronic spectrum analyser is shown in figure 3.3.

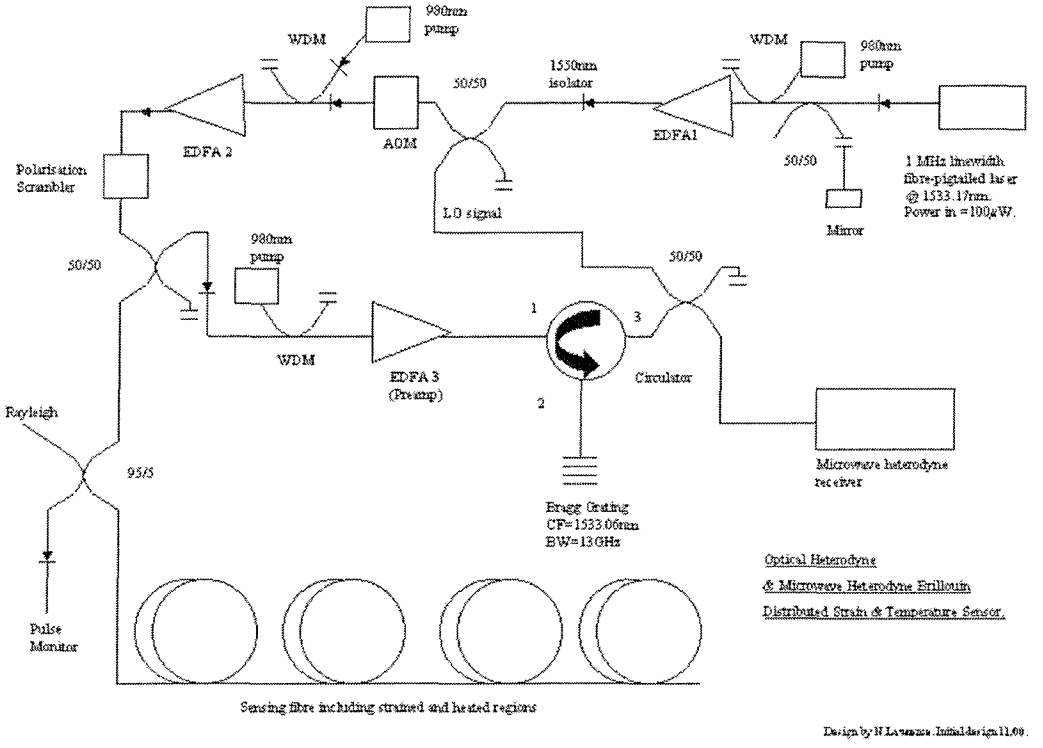

Figure 3.2 Optically Heterodyned and Microwave Heterodyned Sensor Used in This Research.

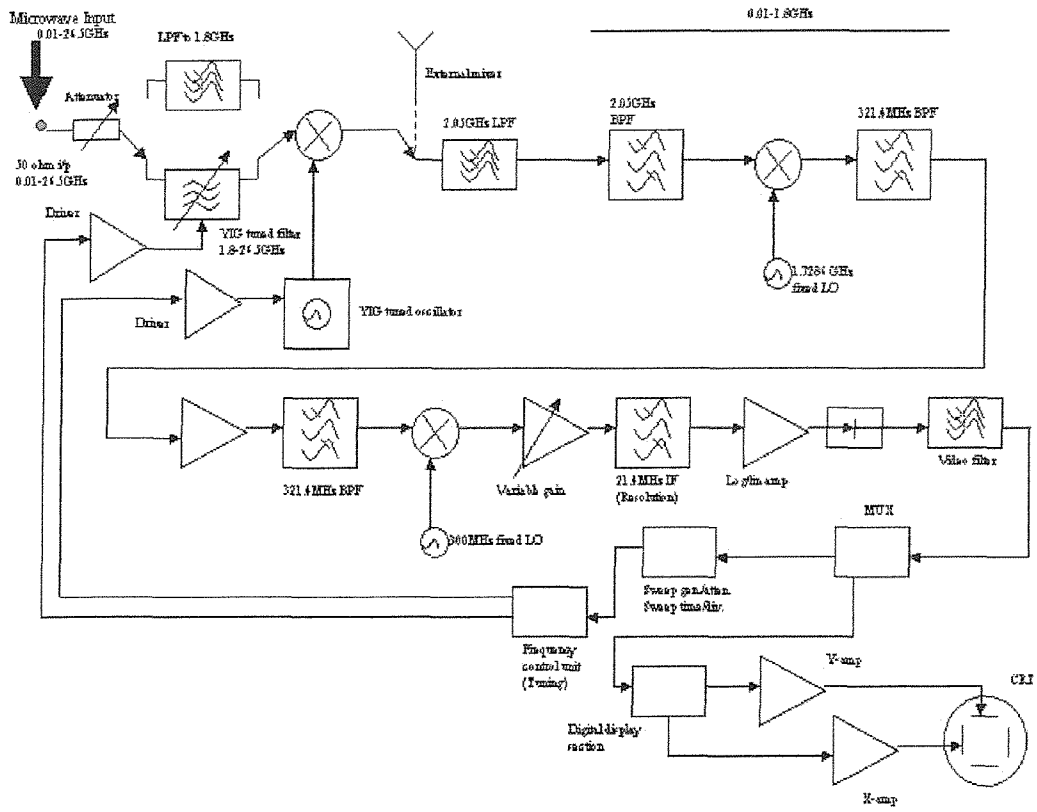

Figure 3.3 A Typical Representation of a Modern Electronic Spectrum Analyser.

A modern electronic spectrum analyser [5] can be easily represented as an elaborate superheterodyne receiver capable of mixing the radio frequency signal to be measured with a local oscillator signal in order to create an intermediate frequency proportional to the incumbent radio frequency signal in every way apart from having a reduced carrier frequency.

In terms of optical fibre sensing, the radio frequency signal is that of the incumbent Brillouin backscatter signal after being optically heterodyned down to a microwave beat frequency of 11GHz plus the AOM modulation frequency imposed on the optical signal when it was pulsed via this component. The local oscillator frequency in this instance is considered to be that used in the final superheterodyne module. The internal structure of the electronic spectrum analyser clearly shows that any incumbent radio frequency is frequency downshifted in a stepped fashion with the resulting intermediate frequency being that resulting from the final superheterodyne module that it has passed through. In this instance the radio frequency is deemed to have reached the final

superheterodyne module and so the resulting intermediate frequency has a frequency of 21.4MHz.

This system incorporating the use of an electronic spectrum analyser, while having produced some very encouraging results as regards temperature and strain resolution along an optical fibre, does possess however the following limitations:

- Firstly, any spectrum analyser, due to its superheterodyne structure allowing for electronic spectral analysis from typically a few 100MHz to a few tens of GHz, has an inherently high noise figure due to its many frequency mixing or superheterodyne circuits. This translates as a reduction in sensitivity which is a problem for any optical scattering analysis where low powers are involved. Typical noise figures quoted for such systems lie within the range of 20 to 35dB.

- Secondly, for most microwave applications a small resolution bandwidth is necessary in order to resolve any received signal in as fine detail as possible. Indeed as new analysers are marketed, one of their selling points is an ever reducing resolution bandwidth needed for discrimination of close proximity signals. Typically resolution bandwidths can be as low as a few kHz rising to 5MHz. However for the analysis of the Brillouin optically scattered spectrum the resolution bandwidth of a conventional electronic spectrum analyser has now proved to be the limitation in terms of spatial resolution with respect to the OTDR nature of Brillouin optical fibre sensing. A 5MHz resolution bandwidth will provide a spatial resolution of 20m.

- From a purely financial point of view, modern electronic spectrum analyser are costly in nature with prices well into the tens of thousands of pounds sterling. It is hence vital that any new design should reduce expense to a minimum.

3.4 Improving on Previous Work

Clearly, in order to improve upon results already obtained by the optical fibre sensor incorporating an electronic spectrum analyser, the limitations of such a sensor, namely noise figure, spatial resolution and price, needed to be addressed. Several ideas were forthcoming:

- The first step taken in this analysis was to look at whether the electronic spectrum analyser could be modified in any way in order to allow for an increase in resolution bandwidth. While 21.4MHz direct outputs were available from the spectrum analyser which could then be adapted manually for either direct passage through an external bandpass filter or direct rectification this would not be useful in the analysis of say a signal measured within a 20MHz bandwidth (5m resolution) as the bandwidth as a factor of the centre frequency is clearly too large.

- Physically opening up the electronic spectrum analyser and changing the intermediate frequency filter or resolution bandwidth filter for one of a wider bandwidth. However, with the fact of the spectrum analyser being a precious commodity within the group, this was deemed as being too risky to follow through on.

- Another way of addressing the spatial resolution impasse that was considered was to open up the spectrum analyser and effectively tap off the intermediate frequency signal from a superheterodyne stage prior to that of 21.4MHz developed from the final superheterodyne stage. This would greatly improve any bandwidth to centre frequency ratio allowing for a measurement to be taken far more closely resembling any signal incumbent on the receiver. This was once again deemed as being too risky.

Hence, another alternative was sought that moved away from using the electronic spectrum analyser in any shape or form.

Armed with the knowledge of the internal structure of an electronic spectrum analyser together with its limitations and the requirements needed to overcome them, three systems were subsequently proposed. The first system was based on a multichannel design. The second was based on the common design of a superheterodyne receiver on which, for all intents and purposes, the modern electronic spectrum analyser is based. Finally the third system involved a complete copy build of the existing spectrum analyser. The third system was soon abandoned due to the complexity and time involved. The remaining two designs are shown in figures 3.4 and 3.5 and their various advantages and disadvantages are compared.

3.4.1 Multichannel Electronic Spectrum Analyser

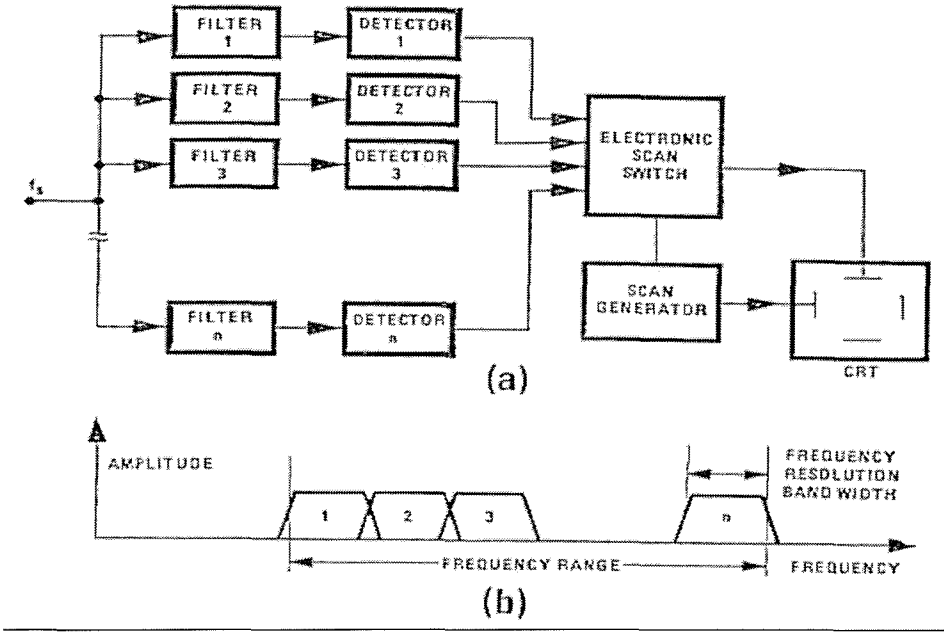

Figure 3.4 Multichannel Spectrum Analyser (a) Schematic Form (b) Passband Filter Arrangement to Define the Frequency Channels (f_S is the Test/Backscatter Signal).

Advantages

- The development of a system to receive the backscatter signal based on a multichannel electronic spectrum analyser would mean no mixing down from 11GHz with the result that this direct microwave detection would generate fast results as no heterodyne scanning across the frequency band of interest would be needed as is the case in any microwave superheterodyne system.

- Less averaging time than that needed by a superheterodyne system is required to detect a backscatter signal since no scanning of the frequency range of interest is required.

Disadvantages

- A 700MHz total filter bandwidth is required at around 11GHz which will be far noisier than the small IF bandwidths used in superheterodyne systems. The bandwidth will also be far from being flat meaning that a complicated calibration method would have to be employed.

- Components are hard to obtain and are expensive.

- Components are far more susceptible to stray effects at this high frequency.

- Brillouin frequency shift measurements are difficult to resolve to an acceptable frequency step.

3.4.2 Superheterodyne Electronic Spectrum Analyser

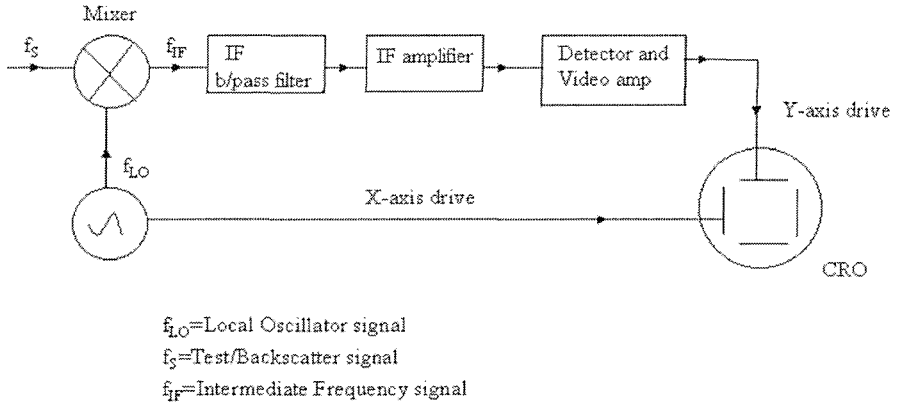

Figure 3.5 Superheterodyne Receiver Schematic.

Advantages

- Increased sensitivity over the direct detection method due to a smaller IF bandwidth.

- Mixing to a low microwave IF means a wider range of microwave connectorised products available.

- Amplifiers at low IF are typically with higher, flatter gain and improved noise figure characteristics.

- Ability to tune over wide range should it be required without changes needed in receiver line-up.

- Spatial resolution of Brillouin backscatter signal can be altered simply by changing the bandpass filter (BPF).

- Based on electronic spectrum analyser frequency conversion techniques so system concept already 'proven' to work. The advantage of this system compared to an electronic spectrum analyser is a greater spatial resolution is possible together with a reduction in noise figure meaning higher sensitivity.

Disadvantages

- Long measurement time required due to scanning over many frequencies.

- There is a greater cascaded noise figure at the front end due to the mixer and BPF when compared to that of the direct detection method (multichannel electronic spectrum analyser). This can be remedied with MESFET mixer technology rather than traditional diode mixer technology hence providing conversion gain and not loss.

Having considered the advantages and disadvantages of these two systems the outcome of this, after surprisingly little deliberation, was to decide upon the superheterodyne-based receiver. The final receiver system set-up is shown in figure 3.6.

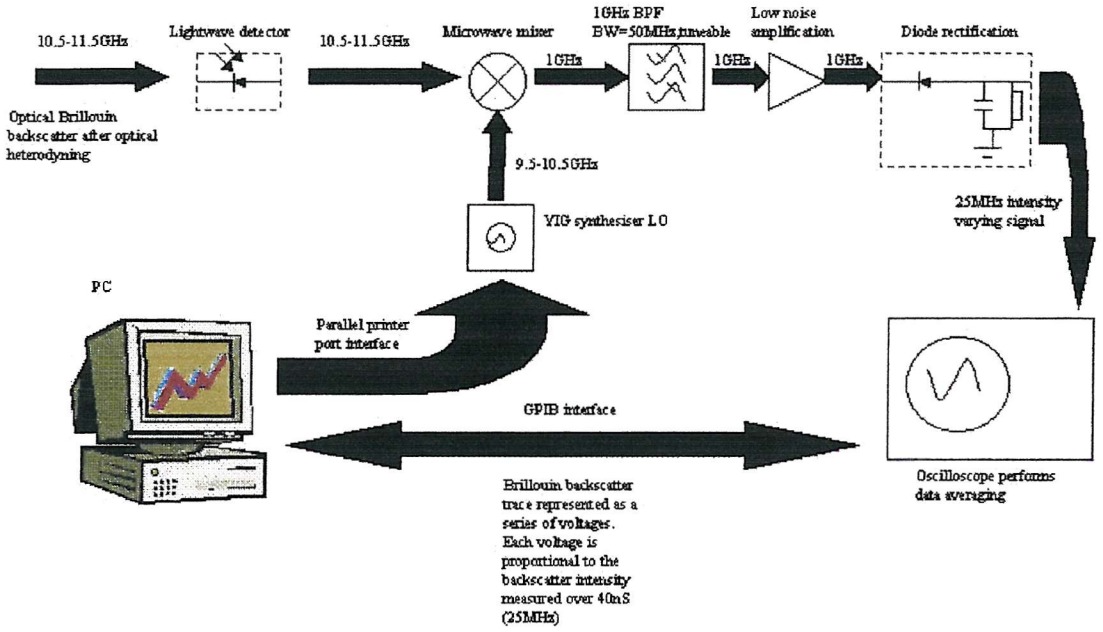

Figure 3.6 Microwave Receiver Based on Superheterodyne Principles.

Hence the sensor developed was based on a dual heterodyne structure. The first heterodyne path involves mixing of the optical backscattered signal with a continuous wave optical signal of wavelength differing by the Brillouin frequency shift (11GHz) and by that due to the modulating frequency of the AOM (110MHz). In this instance this value is 11.110GHz. Then, with this signal still comprising all relevant information with regard to temperature and strain resolution but at the more amenable microwave frequency of 11.110GHz the signal then undergoes frequency downshifting once again through a process of heterodyning but this time down to a lower microwave frequency.

It should be noted that the intermediate frequency of the microwave receiver of 1GHz as shown in figure 3.6 was chosen due to the abundance of microwave components at the frequency with each component demonstrating good values of noise figure, gain flatness, loss and amplification [6,7] compared with those of a higher frequency.

At this juncture a short theory on superheterodyne systems follows.

3.5 An Overview Of Superheterodyning

It is instructive to analyse in some detail the principle operation of a mixer, the component on which superheterodyne theory, to a large extent is based. This component is also the heart of any spectrum analyser. The devices that may be used as mixers include point contact diodes (usually silicon), Schottky barrier diodes, or FETs.

A mixer uses the nonlinearity of a diode to generate an output spectrum consisting of the sum and difference frequencies of two input signals. In a receiver application, a low-level RF signal, in this instance the backscatter signal, and a RF local oscillator (LO) signal are mixed together to produce an intermediate frequency (IF), $f_{IF}=f_{RF}-f_{LO}$, and a much higher frequency, $f_{RF}+f_{LO}$, which is filtered out. This is shown in figure 3.7.

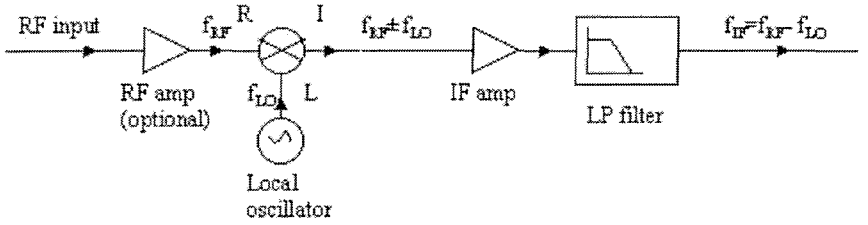

Figure 3.7 Typical Superheterodyne Receiver Chain.

The IF signal usually, due to its low frequency, is able to be amplified with a low-noise amplifier. This is called a heterodyne receiver, and is useful because it has much better sensitivity and noise characteristics than a direct detection scheme. A heterodyne system also has the advantage of being able to tune over a band by simply changing the LO frequency, without the need for a high-gain, wideband RF amplifier.

There are several types of mixer circuits, but the simplest is the single-ended mixer. This is often used as part of more sophisticated mixers.

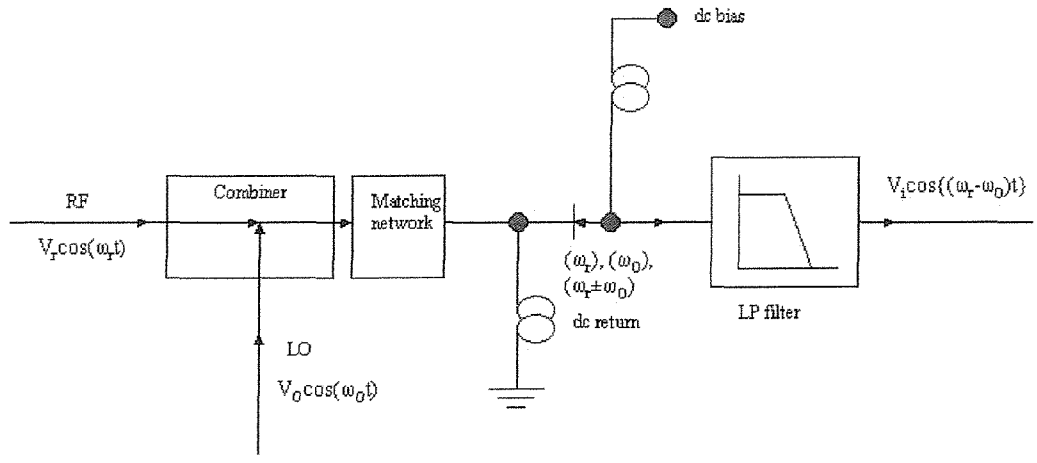

Figure 3.8 Typical Single-Ended Mixer Circuit.

A typical single-ended mixer circuit is shown in figure 3.8, where an RF signal,

$$V_{RF}(t)=V_r\cos(\omega_r t) \qquad \{3.3\}$$

is combined with an LO signal,

$$V_{LO}(t)=V_o\cos(\omega_o t) \qquad \{3.4\}$$

and fed into a diode. The combiner may be a simple T-junction combiner, or a directional coupler. A RF matching circuit may precede the diode, and the diode may be biased through chokes that allow DC to pass while blocking RF. Now from theory [5,8,9], the diode current can be represented as

$$I=(G_d'/2)[V_r\cos(\omega_r t)+ V_o\cos(\omega_o t)]^2$$
$$=(G_d'/2)[V_r^2\cos^2(\omega_r t) + 2\ V_r\ V_o\cos(\omega_r t)\cos(\omega_o t) + V_o^2\cos^2(\omega_o t)]$$
$$=(G_d'/4)[V_r^2 + V_o^2 + V_r^2\cos(2\omega_r t) + V_o^2\cos(2\omega_o t) + 2\ V_r\ V_o\sin\{(\omega_r-\omega_o)t\} + 2\ V_r\ V_o\sin\{(\omega_r+\omega_o)t\}] \quad \{3.5\}$$

where G_d' is the second derivative of the dynamic conductance of the diode which equals the reciprocal of the junction resistance.

The diode current is seen to consist of a constant DC bias term, and RF and and LO signals of frequencies ω_r and ω_o, due to the term which is linear in V.
The DC terms can be ignored, and the $2\omega_r$ and $2\omega_o$ terms will be filtered out. The most important terms are those of frequency $\omega_r \pm\omega_o$.

For a receiver or down-converter, the ω_r-ω_o term will become the IF signal. Note that, for a given local oscillator frequency, there will be two RF frequencies that will mix down to the same IF frequency. If the RF frequency is $\omega_r=\omega_o+\omega_i$, then the output frequencies of the mixer will be $\omega_r \pm\omega_o =2\omega_o+\omega_i$, and ω_i; if the RF frequency is $\omega_r=\omega_o+\omega_i$, then the output frequencies of the mixer will be $\omega_r \pm\omega_o =2\omega_o-\omega_i$, and $-\omega_i$

This latter output is called the image response of the mixer, and is indistinguishable from the direct response. It can be eliminated by RF filtering at the input to the mixer, but this is difficult because the desired RF frequency ($\omega_o+\omega_i$) is relatively close to the spurious image frequency at ($\omega_o-\omega_i$), since generally $\omega_i << \omega_o$. Another way to eliminate the image response is by using an image rejection mixer.

For the case where the RF frequency is $\omega_r=\omega_o+\omega_i$, as is the case for the Brillouin sensor, the output frequency from the mixer is ω_i . This intermediate frequency subsequently passes through a bandpass filter centred on ω_i and with a tuneable bandwidth proportional to that required by the criteria for spatial resolution.

It is noteworthy to realise that mixer power outputs are a directly proportional to their power input since a conversion loss or logarithmic ratio of available RF input power to

IF output power is usually given, to a first approximation, as constant across the operating bandwidth.

Although the backscatter signal is not purely AM in nature as it also undergoes frequency modulation it can be considered to be the intensity of backscatter signal received in a 1GHz IF (see figure 3.6) over successive pulsewidths of, say, 100ns (10MHz or 10m spatial resolution), it can be in some instances regarded as a 1GHz carrier signal being amplitude modulated by a 10MHz 'audio' signal for simplicity. This frequency of 10MHz denotes the most rapid change possible in intensity, hence the maximum audio signal frequency, along the fibre according to the spatial resolution being employed. This leads to the 20MHz bandwidth of a resolution or IF filter at the intermediate frequency of 1GHz being needed in order to rectify this 10MHz signal from a 1GHz signal as shown in figure 3.9.

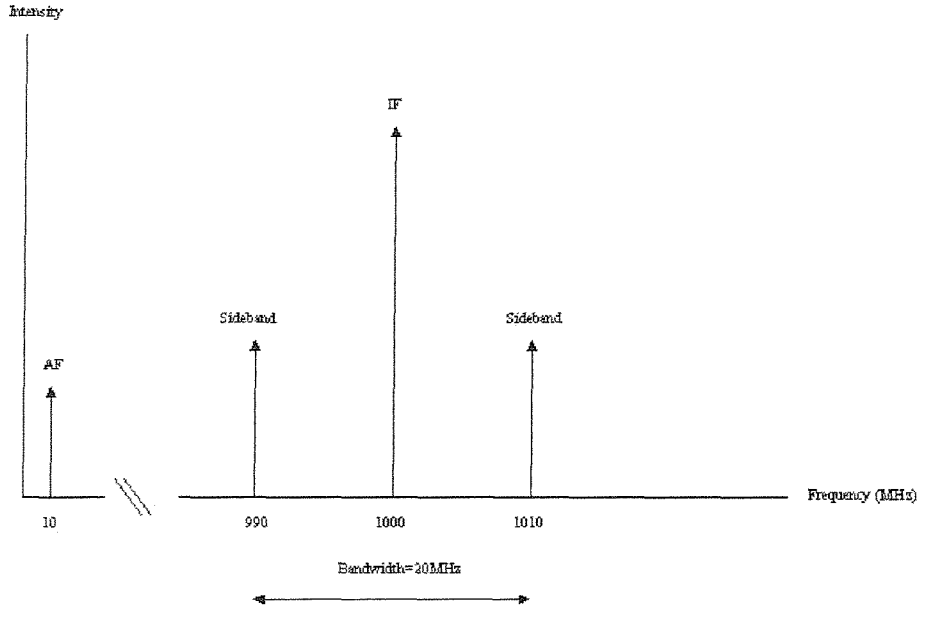

Figure 3.9 Typical DSB-AM Spectral Diagram For a 1GHz IF Signal Being Modulated by a 10MHz AF Signal.

The diode rectifier used in this instance to demodulate the IF signal in order to obtain the 10MHz backscatter intensity-dependent signal operates in accordance with the square-law principle as it is based on diode technology.

A typical square-law region is shown in figure 3.10.

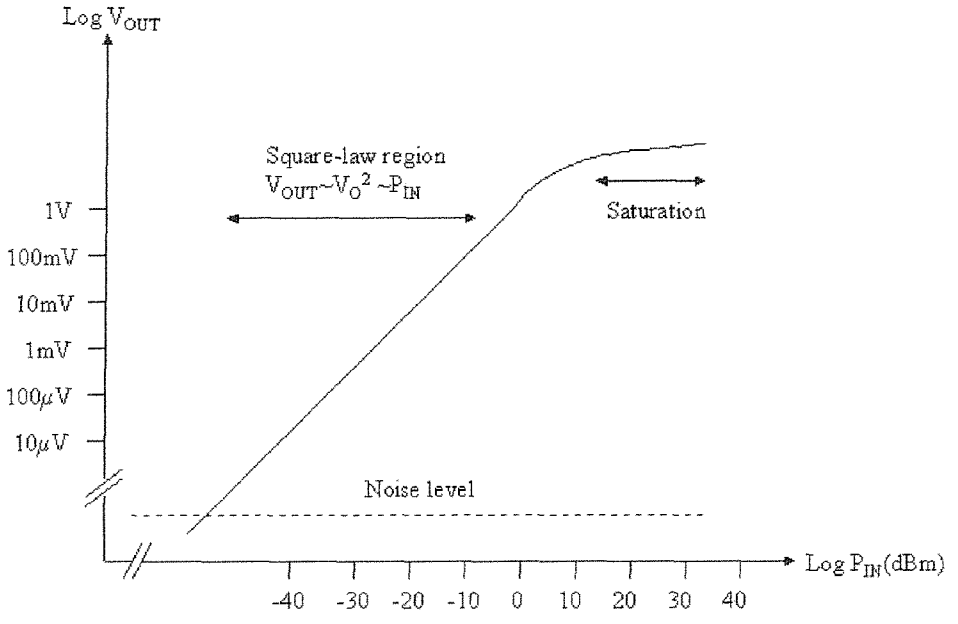

Figure 3.10 Square –Law Region for a Typical Diode Detector.

3.6 Components Making Up The System

3.6.1 Optical System

Previous work performed at the university [10] has developed an optical system which was used in this piece of research. It is instructive in this section to highlight the important characteristics of each optical component of this system. Since the principal aim of this research is to evaluate the new microwave receiver section of the distributed fibre optic sensor and the improvement in spatial resolution resulting from it, the reader is directed towards previous work [4] for a more in-depth appraisal of each optical component.

3.6.1.1 Source

The source chosen for this piece of research was a continuous wave, fibre coupled, Hewlett Packard tunable laser (1474-1567nm) with a linewidth of 300kHz (2.3fm)[4] and a maximum output power of approximately 100μW.

3.6.1.2 EDFA & Pump Lasers

Erbium Doped Fibre Amplifiers (EDFAs) are a useful component within many optical networks. In order to amplify the signal within the sensor for the purposes of improving the signal to noise ratio use is made of this component. Indeed the sensor design in this research comprised three EDFAs. EDFA1 as seen in figure 3.6 acted as an amplifier for both the local oscillator signal and the signal sent to the AOM for pulse generation. EDFA2 was incorporated to boost the pulsed signal strength before launching into the sensing fibre ensuring a high signal strength at the output. Finally EDFA3 was included as a preamplification stage for the backscatter signal before it was finally detected. This third amplifier was constructed so as to effectively nullify the optical loss that had been observed along the optical return path of the sensor.

The principle of the EDFA lies in the fact that a length of Erbium doped optical fibre can be pumped by a laser pump operating at any of the following typical wavelengths, 532nm, 670nm, 807nm, 980nm and 1480nm [11]. Through this pumping, Erbium ions are induced into a higher energy state also known as population inversion.

Then, according to relaxation theory, the electrons that have been pumped to the upper lasing level or $^4I_{11/2}$ energy level with a lifetime of around 3μS [12] undergo relaxation to the $^4I_{13/2}$ metastable energy level with a relatively long lifetime of approximately 10mS [4]. In order for the Erbium ion to fall back to its original pre-pumped state, radiative decay at 1.55μm then occurs to the $^4I_{15/2}$ energy level or ground level. Figure 3.11 demonstrates the principal.

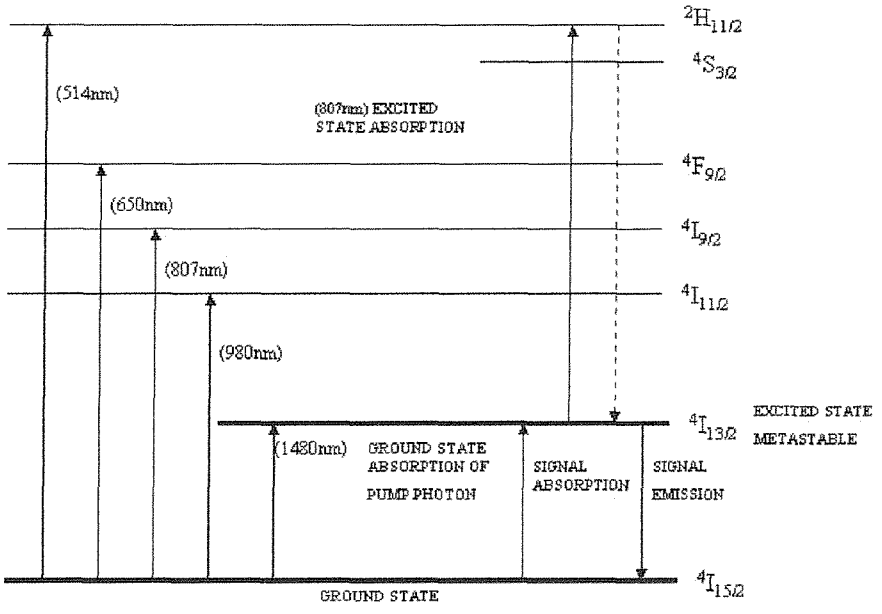

Figure 3.11 Erbium-Doped Fibre Schematic With Pumping Levels.

Applying this theory, EDFA1 was built to give an optical gain of 23dB with EDFA2 having a gain of 32dB and finally EDFA3 possessing a gain of 14dB.

The pump lasers chosen for the amplifiers in the sensor were 980nm fibre-pigtailed laser diode sources with in-fibre maximum output powers of between 75mW and 110mW.

3.6.1.3 AOM

Through the application of a modulating RF signal to it, a bulk-wave acousto-optic Bragg modulator (AOM) is able to generate pulses with typical rise times of 20ns to 150ns [13]. The basic AOM cell consists of an acoustic cell of sufficiently large aperture and obviously a laser source of which the signal is to undergo diffraction, both operating at suitable wavelengths. The acoustic cell itself is made of a column of

anisotropic or isotropic material that possesses desirable acoustic, optical, and acousto-optic properties.

An RF signal is applied to a planar piezoelectric transducer bonded on one finely polished end face of the crystal through which incident light is propagating. An acoustic wave within the crystal is set up through the application of this modulating signal with the result that a moving optical or refractive index grating is induced within it. This effectively turns the AOM into a switch by which incident light is diffracted according to the principle of Bragg diffraction. The relationship governing the diffraction principle in this instance is

$$\sin\theta_i = n\sin\theta_{Bragg}$$
$$= (\lambda_i \nu_{RF})/2v_{acoustic} \qquad \{3.6\}$$

where θ_i is the angle of incidence, θ_{Bragg} is the Bragg angle, λ_i is the incident wavelength in , ν_{RF} is the RF frequency and $v_{acoustic}$ is the acoustic velocity.

The angle through which the incident beam is deflected is typically of the order of 2-3° for 1550nm radiation, 110 MHz modulating RF frequency and an acoustic velocity of 4000m/s. Figure 3.12 demonstrates an AOM structure.

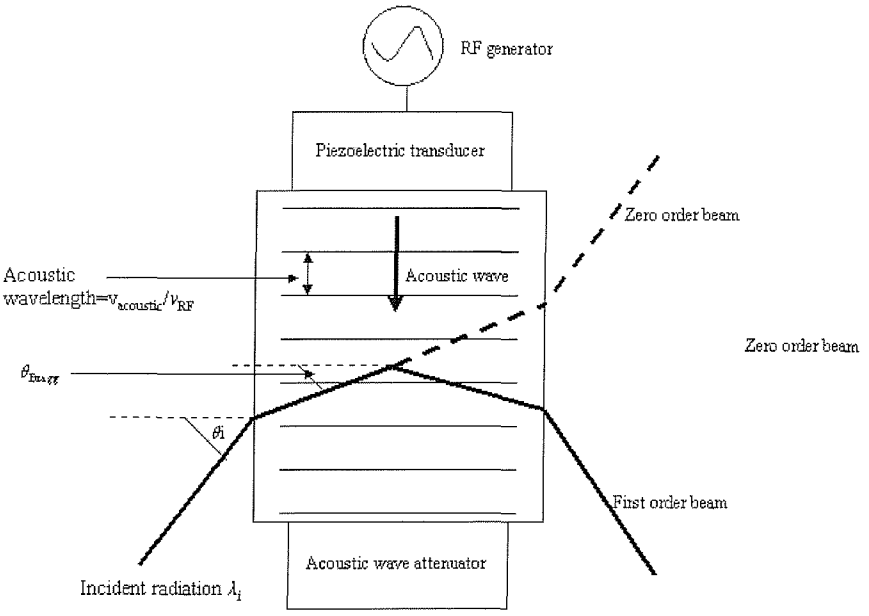

Figure 3.12 Bulk-Wave AO Bragg Modulator (AOM). In This Instance the AOM Is of the Upshift Variety As Is Used In This Research.

Since the grating is moving, the deflected light undergoes either a Doppler upshift or downshift by the applied RF frequency. The upshift and downshift correspond, respectively, to the cases in which the wave vector of the incident light wave is at an angle greater than and smaller than 90° from the wave vector of the acoustic wave.

With no RF signal applied, no diffraction takes place and no light is coupled into the first order beam. This leads to a high extinction ratio being offered by the AOM. With suitably high RF power (around 3W) the diffraction efficiency of the AOM can reach 80% but due to additional loss from the input and output coupling fibres the loss is usually >3dB in pulsed mode. Although the intensity of the diffracted light is proportional to the power of the acoustic wave or the RF driving signal, thermal considerations limit the RF power that can be applied to an AOM as too much heat within the crystal can cause irreparable damage.

The pulse modulator chosen for this piece of research was a 20-25ns rise-time 110MHz upshifting TeO_2 AOM, with an insertion loss of 3dB at 3W applied RF power. The device was fibre coupled for ease of use and stability and had a quoted extinction ratio of >50dB.

3.6.1.4 Polarisation Scrambler

Optical heterodyne theory assumes that the two mixed signals are of the same polarisation. Should the polarization states differ from each other, however, the interference will not be complete and reduces to zero for orthogonal positions. In order to maximize the interference, a polarisation controller could be used on the local oscillator signal if the Brillouin backscatter signal remained at one constant polarization state. However, standard single-mode optical fibre has low birefringence and so the polarisation states of both the input pulse and the backscatter signal would be affected by this. The backscatter signal therefore has a different polarization and therefore a different heterodyne efficiency depending on its point of origin within the fibre. Fibre birefringence changes only slowly with time so the noise on the trace resembles coherent Rayleigh noise and will not be reduced significantly by temporal averaging. This noise is peculiar to heterodyne detection. There is, however, no persistent component of coherent noise in the Brillouin trace due to each scattering center producing a different phase shift at the detector. This is due to the scattering centres not being spatially fixed, as is the case for density fluctuations in Rayleigh scattering. Instead they occur where there is an interaction with a phonon. Each trace will therefore have different phase noise characteristics and averaging over many traces will remove this component of the noise.

A 3-axis polarization scrambler based on a fibre squeezing technique using piezo-electric transducers to induce fibre birefringence along each of 3 axes was used to reduce polarization noise to a minimum. The state of polarization of the input, polarized radiation to the sensing fibre is continuously varied in time such that, over a sufficiently long averaging time, the output radiation interferes as though unpolarised. For more details of the polarisation scrambler design, information can be obtained from [4].

3.6.1.5 Fibre Bragg Grating

The Fibre Bragg Grating used in this research has been included to reduce the amount of Rayleigh signal and ASE feedthrough to the detector while ensuring that all the anti-Stokes passes unaltered. The bandwidth of the grating is given in figures 3.13 & 3.14 and is of the order of 13GHz (0.11nm) and is centred on 1533.06nm. This ensures that the Rayleigh signal is significantly rejected allowing measurements to be made purely using Brillouin backscatter. This is due to the fact that a source wavelength of 1533.17nm was employed in the measurements and since the Rayleigh backscatter is only shifted by 110MHz (8.8e-4nm) in this instance from this wavelength it should not encroach into the Fibre Bragg Grating (FBG) bandwidth. The Brillouin backscatter however will be upshifted by 11.110GHz (0.09nm) as described in 2.1 so causing the backscatter to fall well within the optimum region of the FBG for direct and near 100% transmission through to the detector.

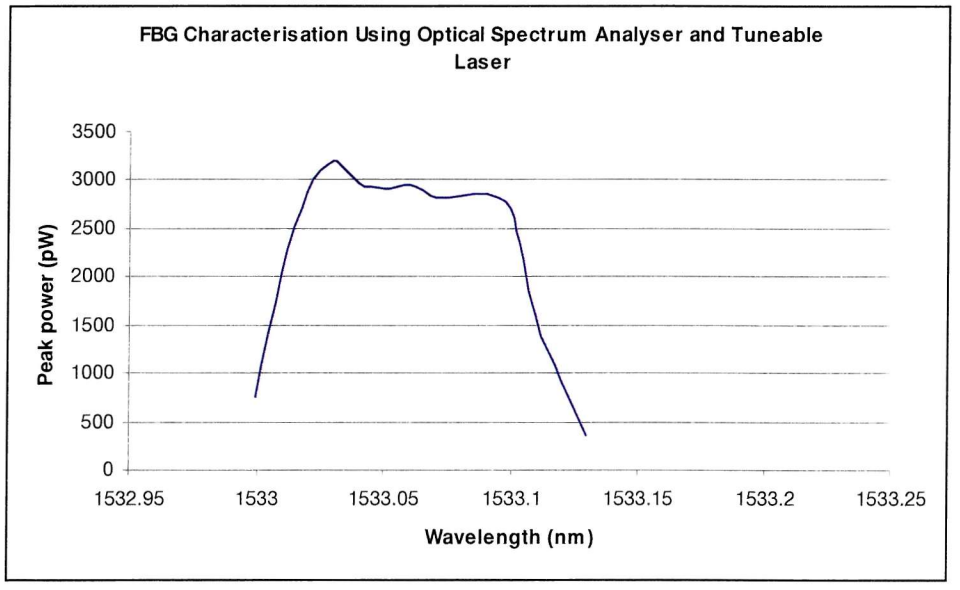

Figure 3.13 Fibre Bragg Characterisation Using Optical Spectrum Analyser.

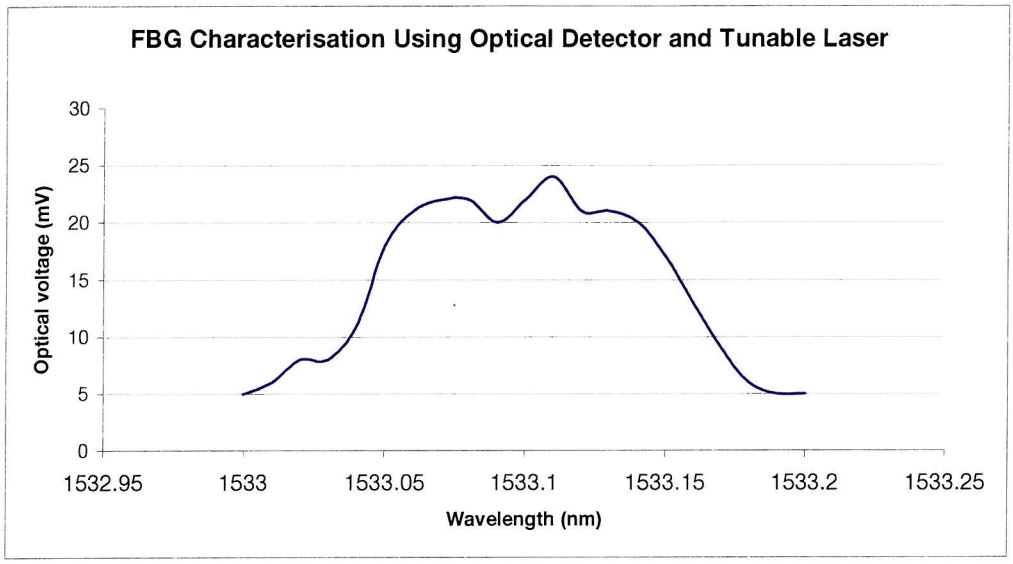

Figure 3.14 Fibre Bragg Characterisation Using Optical Detector.

3.6.1.6 Lightwave Receiver

This component is used within the system to convert photonic energy from the optical section of the sensor into electrical energy for amplification and subsequent detection within the microwave section of the sensor. The detector used in this research was a Hewlett Packard (HP 83440C) 20GHz bandwidth high-speed lightwave converter. It comprised a fibre-connectorised, DC-coupled, hermetically sealed, unamplified InGaAs photodiode, with a responsivity of 0.65A/W at 1550nm and a corresponding gain of 32.5V/W into a 50Ω load [14].

3.6.2 Receiver System & Microwave Components

3.6.2.1 Mixer

The microwave mixer M1-0412 [15] was designated as being suitable for use in the receiver system because it had:

- Correct frequency of operation- this particular mixer, based on diode technology, is designed to accept radio frequency and local oscillator signals anywhere in the range of 4-12GHz while producing an intermediate frequency of DC to 4GHz.

- Low conversion loss of 5.5dB- this is effectively the intermediate frequency signal output strength compared to that of the incumbent radio frequency strength. The ensuing power ratio is quoted as a value in decibels. To note is the fact that the near constant value of loss around the Brillouin backscatter frequency of 11GHz suggests a linear conversion from radio frequency signal intensity to intermediate frequency signal intensity.

- The local oscillator drive level of +10 to +13dBm allows a range of technologies including VCOs, SSPAs and synthesiser units to deliver this power to the mixer.

- The isolation between local and radio frequency ports is excellent at 40dB with the intermediate and local frequency ports being also well isolated at 25dB. This ensured minimum imposition of the local oscillator's characteristics onto the signal being downshifted and subsequently investigated.

- The housing of the mixer is available in many configurations.

3.6.2.2 YIG Synthesiser

After looking into the current market of local oscillator products, it turned out that while SSPAs could be procured at the frequency required they remained extremely cost inefficient as a means of generating a local oscillator signal. It transpired also that VCOs at a frequency of 11GHz are very difficult to obtain.

As a result of this, attention was turned to a synthesised solution, namely that of the YIG synthesiser of which the benefits are outlined below:

- The YIG (Yttrium Indium Gallium) digital synthesiser MLSL-1077H [16], based on permanent magnet technology, provides an extremely cost effective solution to the need for a local oscillator at 11GHz. The unit itself is robustly packaged since it is commonly used in marine transceiver units, this being useful for an optical fibre sensor as it is often taken into demanding environments.

- The phase noise of the unit provides a minimal frequency shift error on any backscatter signal being investigated.

- The power delivered by the unit (min. +10dBm) across its bandwidth (9.5-10.5GHz) is consistent with the mixer technology being incorporated into the receiver system and varies minimally across the frequency range to be investigated as seen in figure 3.15.

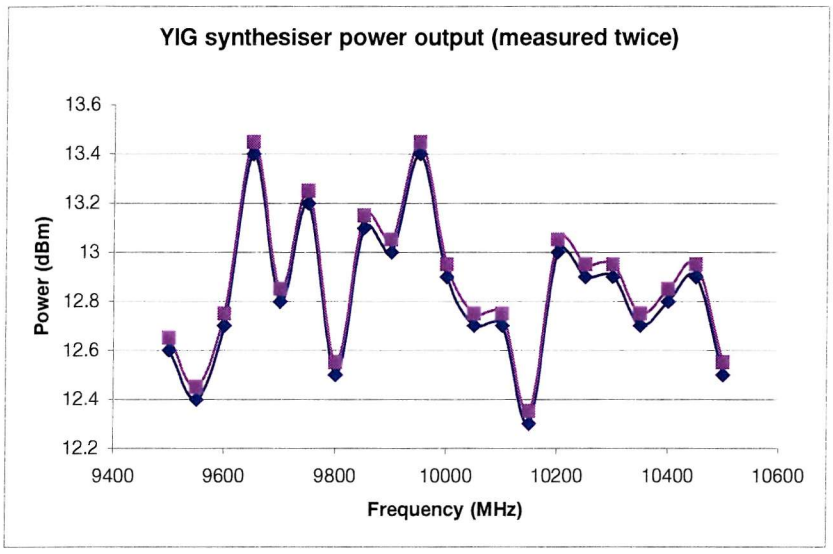

Figure 3.15 YIG Synthesiser Power Output (Blue Line (with Diamonds) is the Manufacturer's Specification, Pink Line (with Squares) is the Measured Output).

- The frequency of the device is also suited for use in the receiver system since, for a 1GHz intermediate frequency signal to be developed, the local oscillator signal should be centered at a frequency 1GHz below that of the radio frequency signal to be downshifted.

- The unit is able to step in intervals of 250kHz hence allowing for in-depth investigation of a particular frequency of interest should the need arise.

- The frequency produced by the YIG synthesiser is entirely faithful to the frequency required from it. This was verified before the YIG synthesiser was used in the sensor and demonstrated observed frequency errors less than 500kHz over a 48 hour period.

- The unit is fully programmable using C as its programming environment. This allows for frequency sequences and data averaging to be employed while using the unit.

- The unit's environmental credentials demonstrate a frequency stability from –35°C to +75°C of ±20kHz. Its power stability across this range is ±2dB. RF-wise the unit is fully operational with the technology considered for the sensor.

3.6.2.3 Bandpass Filter

Having chosen 1GHz as a desirable intermediate frequency of the receiver necessitates a bandpass filter centred on this frequency in order to act as an intermediate or resolution filter. The ideal filter, for an increased spatial resolution of 4m say, would need to be centred on 1GHz with a 50MHz bandwidth to enable all backscatter intensity measurements measured within the corresponding timescale for 4m resolution, namely 40ns, to be collected and subsequently correctly rectified. The reason for the 50MHz bandwidth and not 25MHz is evident in the fact that the 1GHz intensity dependent signal is changing over a timescale of 40ns (25MHz) where the superheterodyne receiver will collect both sidebands. This means that intensity measurements from 975MHz to 1025MHz should be captured and processed by the system. This means that the signal is effectively 3dB stronger than a single sideband system often employed in other types of superheterodyning systems. Another parameter deemed necessary for the filter was that of bandwidth tuneability. The filter purchased for the receiver makes use of a variable capacitor in its filter-tuning network that can be tuned through a screw in the housing to enable the bandwidth of operation to be modified to suit whichever spatial resolution is required. This is important since, as seen above in the case put forward for the tuned-filter receiver, one of the disadvantages of a wide bandwidth in capturing a small signal is the amount of unused bandwidth that effectively becomes a noise generator. Conversely, too small a bandwidth means that fast changes in intensity are effectively not picked up by the receiver resulting in a smooth and inaccurate OTDR trace. This results in poor spatial resolution leading to inaccurate temperature and strain resolution. The bandwidth of the filter purchased is shown in figure 3.16 and can be seen to show 3dB cutoff limits at 973MHz and 1024MHz to a first approximation. This remained the bandwidth for both 4m and 10m spatial resolving.

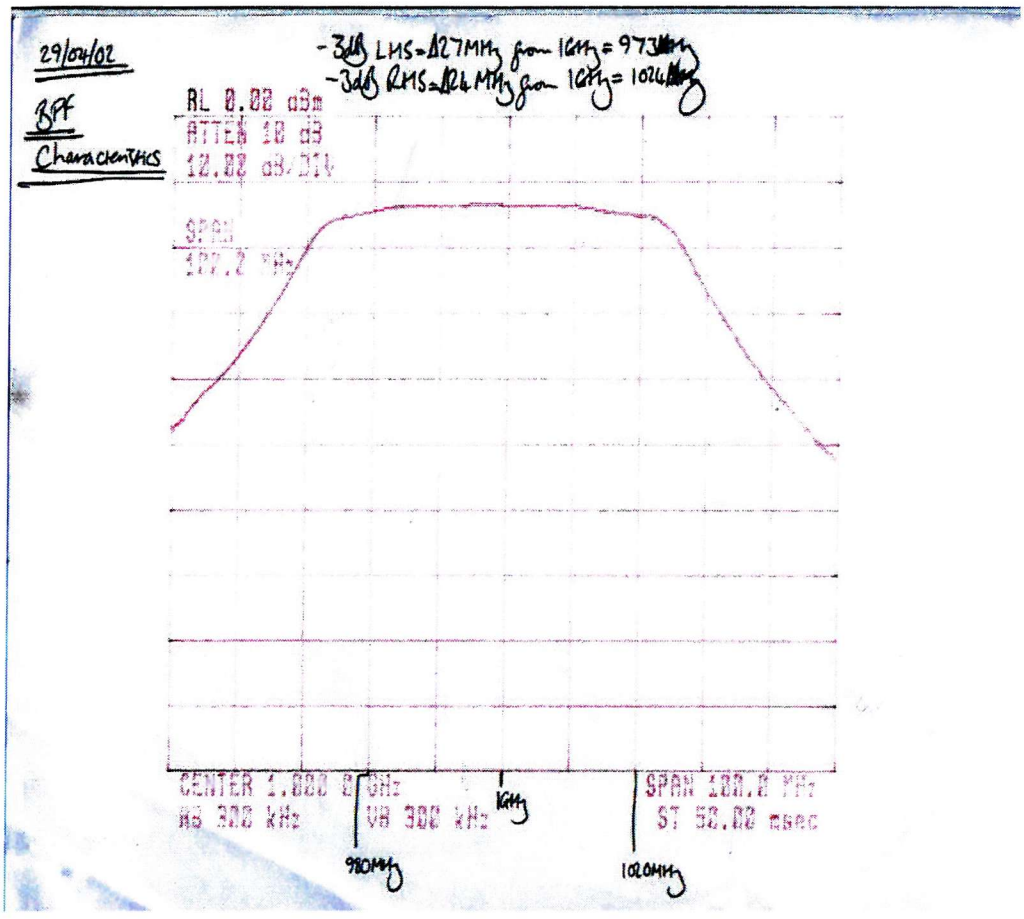

Figure 3.16 Typical Bandwidth of the Microwave Bandpass Filter (Scale used is 10MHz/div on x-axis and 10dB/div on y-axis. X-axis is centred on 1GHz. Loss on y-axis is relative and not absolute). 3dB Roll-Off Corners are Set at 973MHz and 1024MHz.

3.6.2.4 Amplifiers

Amplifiers at 1GHz are more abundant and competitively priced than those at 2 GHz and above. This was one of the driving points in choosing this frequency as the intermediate frequency. It was decided that two amplifiers would be sufficient in supplying the gain necessary to provide a signal strong enough at the rectifier output in order to ensure that a good SNR and hence temperature and strain resolution would be possible. Another advantage of the system being set at 1GHz is that components at this frequency are flatter in terms of gain than systems operating at higher frequencies. Also the fact that the backscatter signal is basically a 1GHz intensity signal being modulated by the refractive index of the fibre determined by the strain and temperature present on

it means that the components from the output of the mixer to the input of the diode rectifier do not need to be calibrated as such since they are all operating at only the intermediate frequency of 1GHz. The gain of the two amplifiers purchased [6] in series was found to be +61dB as shown in figure 3.17. This corresponds well to the quoted literature figures of >28dB each so giving >56dB in series. The theoretical flatness of the amplifier system is in theory close to 0dB since the system is operating at 1GHz within a 50MHz bandwidth (for 4m spatial resolution). The figure of 56dB gain being required was calculated from the theoretical value of 2μW being output from a 0km Brillouin backscattered signal being mixed with a 1.3mW optical local oscillator in the case of a 10m spatial resolution sensor. This optical output would then be converted through the lightwave converter with a known conversion factor of 32.5V/W. In turn, this would give an electrical output of 65μV into the microwave receiver resulting, powerwise, in –10dBm being fed into the diode rectifier. The specification of the diode rectifier would limit any further amplification of the signal since the maximum input power to this device is +17dBm.

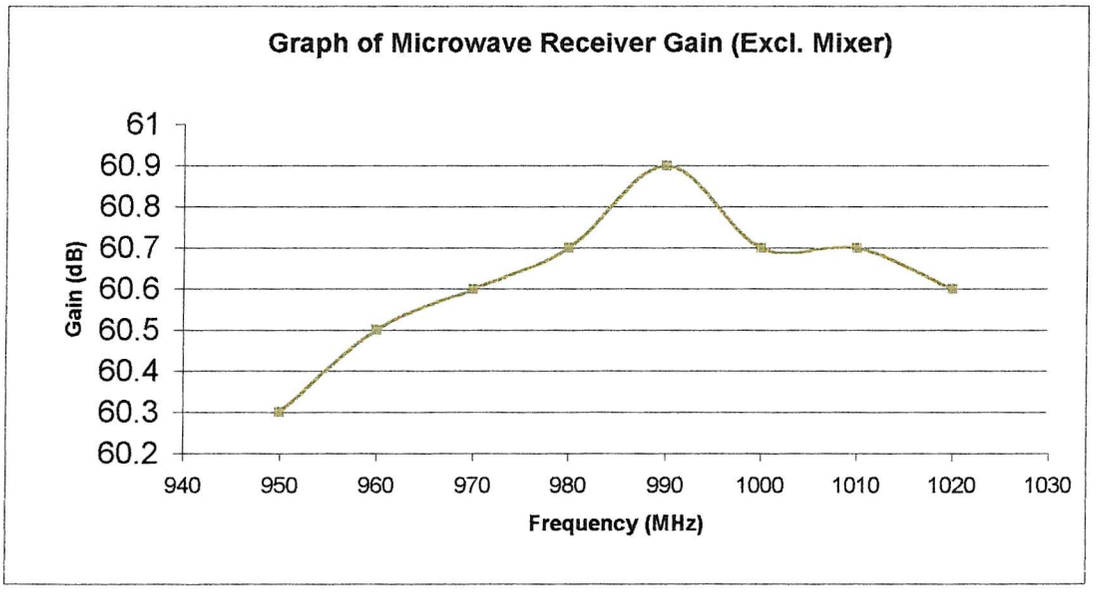

Figure 3.17 Intermediate Frequency Stage Gain of Microwave Receiver Section of Sensor.

3.6.2.5 Diode Rectifier

The diode rectifier is the fundamental connection between the 1GHz intensity varying signal and any OTDR trace that is to be collected. The necessity for a good input/output

VSWR meaning little reflectance of signal incumbent on the module is of primary importance for generating an OTDR trace authentic to the backscatter signal received. With a conversion factor of 1500-2000mV/mW it is evident that any electrical signal voltage passing through it is squared according to the square law employed in diode based-systems. The diode rectifier used in this instance was unbiased with a dc return ensuring that no dc offset on the backscatter signal was observed.

The flatness is quoted as ±0.62dB [7] across a 200MHz bandwidth centred on 1GHz suggesting that performance at the specified intermediate frequency should be almost ideal.

3.6.2.6 Coaxial Cabling Effects On Rise Times

At the diode rectifier output of the Brillouin sensor, 1m of RG174 C coaxial cabling is attached in order that data transmission to the 200MHz oscillscope for averaging can take place. A 50pF capacitor is known to be present on the ouput of the diode rectifier together with a 50 ohm output resistance. The nominal value of capacitance per metre for RG174 C cable is 60pF. This suggests a rise time on the Brillouin sensor output of [50ohms x (50+60)pF] or 5.5ns. This is far smaller than the smallest pulsewidth of 40ns and suggests that no rise time delays should be seen in data collected. As the results in subsequent chapters demonstrate, this was proven to be the case.

3.7 Data Processing Including Code Written Specifically For The Control Of The New Microwave Receiver

In order to control the new receiver, source code was written in the C programming environment using LabWindows after having been sent a basic YIG synthesiser source code template from the manufacturers of this component. This controls the frequency scanning of the YIG synthesiser LO, sampling & averaging of rectified data and subsequent file creation and downloading to a PC.

A brief pseudo code algorithm of the control code that was written is given below (see also figure 3.6).

- Input the lowest frequency to scan, the highest frequency to scan and the frequency step to use while moving from the lowest to the highest frequency.

- Code the lowest frequency into binary code that can be interpreted by the YIG synthesiser. The YIG synthesiser then generates a digitally synthesised frequency at exactly 1GHz below the lowest frequency input.

- The oscilloscope registers any ensuing backscatter and proceeds to average this data in user-defined averaging stages through renewing the backscatter trace in real-time and subsequently taking the average at each point along the trace. The default number of averages is 4096 taking around 50 seconds to complete but the number of averages can be altered if necessary. Multiples of the 4096 averages can then be taken up to any number value required. Once again the data averaging is accomplished by taking the average of the data at each point along the trace, the difference being in this instance that the system is not using real-time data but rather the averaged set for each set of 4096 traces. The code used to perform the required averaging was adapted from an original code written by G.Lees.

- The YIG synthesiser is then written to again in order to shift its frequency up by one step size. Once again the YIG synthesiser is 1GHz below the backscatter frequency to be examined. Hence should 10.9GHz be the backscatter frequency of interest the YIG synthesiser is set to 9.9GHz so as the 1GHz microwave receiver can give the required trace output.

- The process continues until the highest frequency backscatter has been data averaged.

Finally the averaged backscatter data must be scaled according to a set of frequency-power coefficients established both theoretically and practically using a Marconi 8210 network analyser which are shown in figure 3.18. The blue line represents the coefficients according to manufacturer's data with the pink line representing data measured using the network analyser. The pink line data was measured in 5MHz steps as shown in figure 3.19 but is shown in figure 3.18 with increased frequency step sizes.

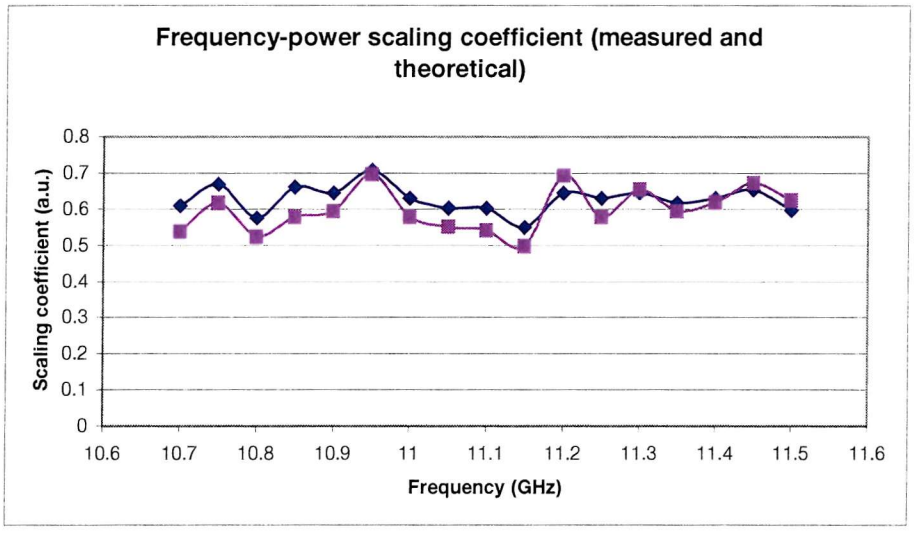

Figure 3.18 Frequency-Power Scaling Coefficients for the Microwave Receiver (Blue Line (with Diamonds) Represents Theoretical Coefficients from Manufacturer's Data, Pink Line (with Squares) Represents Measured Data Found Using a Network Analyser).

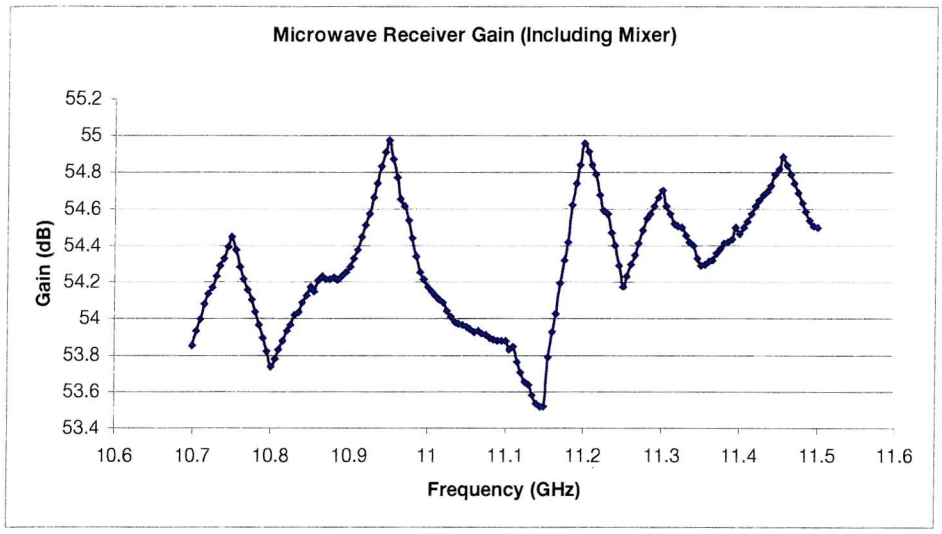

Figure 3.19 Microwave Receiver Gain Including Mixer.

3.8 How The Sensor Operates

Attention is now turned to demonstrating the principle behind the operation of the new sensor. An example is given here incorporating the sensor being employed to gather backscatter information over a 30km length of standard telecommunications fibre.

The optically heterodyned and microwave heterodyned sensor is shown in figures 3.2 and 3.6.

3.8.1 Sensing Pulse Generation

Figure 3.2 shows how a continuous wave seed signal, generated by the tuneable laser, is amplified through EDFA1 after which the signal is effectively split 50/50. With 50% of the amplified signal having been hived off for use an optical local oscillator signal the remaining 50% is fed through to acousto-optic modulator whereby a first order shifted optical output is obtained in a pulsed format, the pulsewidth and period being set by the electrical trigger controlling the AOM's operation. Due to the optical shifting taking place within the AOM the pulse signal output is effectively upshifted or downshifted by

the modulation frequency of the AOM according to whether an upshift or downshift variant of this component is used. In this instance an upshift AOM is used.

With the AOM effectively generating pulses through acousto-optic chopping or blocking of the signal rather than forming pulses through integration of the energy in the continuous wave into a single pulse, the pulse output is less intense than the intensity of the continuous wave entering it. This is due to losses encountered during the optical shifting from zeroth to first order output. This is remedied by another amplification stage after which polaristaion noises that can be encountered within the pulsed optical signal are reduced through a polarisation scrambler. The signal is then split 50/50 once again before finally passing through a 95/5 coupler and into the sensing fibre.

The Rayleigh backscatter signal, essential for the purposes of normalisation of anti-Stokes backscatter intensity, is generated from pulsed broadband ASE from EDFA1 within the optical transmission path. For this generation to occur, the broadband mirror at the coupler directly connected to the tuneable laser is employed while no tuneable laser signal is used. This ensures a broadband source, needed so as coherent Rayleigh noise (CRN) is not present on the signal, is obtained for the Rayleigh backscatter signal. The source signal then follows the same optical transmission path through the AOM as discussed for the anti-Stokes source signal.

3.8.2 Receiver System Operation

As can be seen in figure 3.2, the Rayleigh backscatter signal is readily obtained through the 5% port of the coupler directly connected to the sensing fibre. Due to the fact that this signal is not optically heterodyned, the application of an optical detector rather than a microwave receiver is needed.

The anti-Stokes backscatter on the other hand, after passing through the 95% arm of the coupler just mentioned, passes through the 50/50 coupler and on to a preamplifier used to effectively boost the signal power before optical heterodyning with the local oscillator signal previously discussed. The resultant beat frequency is a signal of 11GHz (the frequency shift seen in the Brillouin backscatter process) +110MHz (the

AOM modulation frequency). The local oscillator is also used to boost this 11.1GHz signal strength according to {3.2} before passing through the lightwave detector in which optical energy is converted to an electrical signal. This electrical signal, still at 11.1GHz, is then incumbent on the microwave mixer where, through YIG synthesiser local oscillator interaction, it is down converted to an intermediate frequency of 1GHz.

The signal is then filtered at this frequency using a bandpass filter with a 3dB bandwidth determined by the spatial resolution required. In this instance, a 4m spatial resolution signal would need a bandwidth of 50MHz with a 10m spatial resolution requiring a 20MHz bandwidth. However, in this thesis, the bandwidth was left unchanged at 51MHz (-3dB). With the signal then passing through a low noise amplification stage it is finally rectified into an intensity changing signal of duration determined by the pulsewidth of the optically transmitted pulse.

In order to explain how the anti-Stokes receiver system works, suppose a 30km length of sensing fibre has three regions of interest. The first 10km (Region 1) is subjected to neither any strain nor temperature. The second 10km (Region 2) is subjected to a temperature of X Kelvin above ambient but no strain. The third 10km region (Region 3) is subjected to a strain of Y microstrain but is kept at ambient temperature. Due to the nature of Brillouin backscatter three discrete Brillouin linewidth peaks [17] are inherent on the fibre with their respective frequency shifts from the original launch pulse governed by the effects of strain and temperature exerted on each section.

A broadband Rayleigh backscatter signal, in order to normalise out splice/bend losses, is obtained as already described. Following this, a narrowband anti-Stokes signal is then established in order to obtain the Brillouin backscatter signal to be measured.

Having chosen an IF of 1GHz, the YIG synthesiser LO is required to scan through a range of frequencies in user-defined frequency steps 1GHz below the Brillouin backscatter frequency range. Hence, the range has been chosen to run from 9.5-10.5GHz to cover a backscatter range of 10.5-11.5GHz. The source code written in C in 3.7 controls the frequency scanning of the YIG synthesiser LO, sampling & averaging of rectified data and subsequent file creation and downloading to a PC.

Figure 3.20 shows three graphs representing backscatter traces for backscatter frequencies of 11GHz, 11.2GHz and 11.4GHz that could be collected by the sensor.

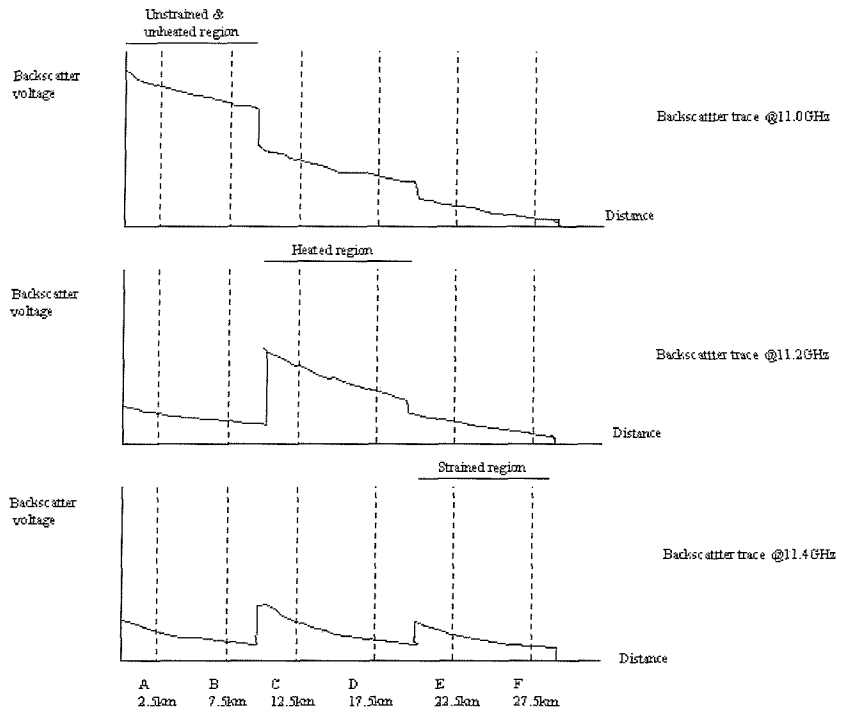

Figure 3.20 Three Backscatter Traces Each Received at Different Interrogative Frequencies.

As can be seen from the traces above the backscatter intensity is different for different backscatter frequencies due to the effects of strain and temperature. The measured backscatter intensities at A,B,C,D,E,F along the fibre at 5km intervals can be used to give the 3 Brillouin spectral linewidths as shown in figure 3.21 even though the example is much simplified. This can be understood by noticing that, at 11.0GHz, backscatter intensities A and B appear to be relatively greater than those at C, D, E and F due to an apparent step in backscatter intensity. A similar argument stands for backscatter intensities C, D at 11.2GHz and E, F at 11.4GHz. Obviously, the resolution of the backscatter spectral envelope improves with more backscatter frequencies being sampled and greater averaging being employed.

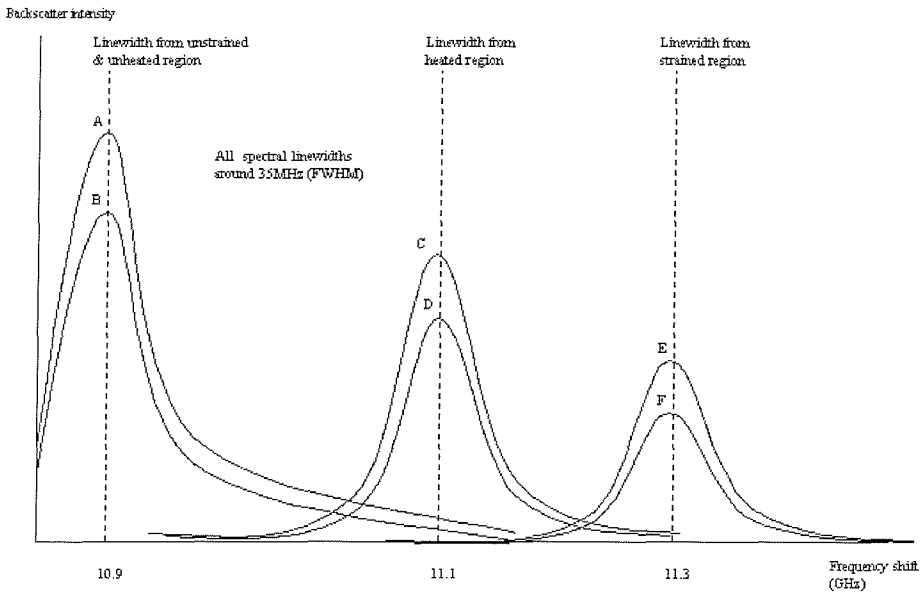

Figure 3.21 Three Corresponding Linewidths for the Three Backscatter Traces Each Received at Different Interrogative Frequencies Shown in Figure 3.20.

Through the use of the Landau-Placzek Ratio (LPR), a means of normalising an anti-Stokes backscatter intensity signal by means of a Rayleigh backscatter signal, together with the three discrete Brillouin linewidth peaks above and equations {3.8} given below, the applied temperature and strain to the second and third regions of the sensing fibre with reference to region 1, the control region, can be ascertained.

Now,

$$\Delta\nu_b = C_{\nu b\varepsilon}\Delta\varepsilon + C_{\nu bT}\Delta T$$

$$\Delta P_b = C_{Pb\varepsilon}\Delta\varepsilon + C_{PbT}\Delta T \qquad \{3.7\}$$

where

$\Delta\nu_b$ =change in Brillouin frequency shift due to applied heat and strain

ΔP_b =change in Brillouin backscatter intensity due to applied heat and strain

$\Delta\varepsilon$=applied strain (in microstrain)

ΔT=applied temperature

The applied strain and temperature at a point on a fibre are then given as,

$$\Delta\varepsilon\ (\mu\varepsilon) = (|C_{\nu b\varepsilon}C_{PbT} - C_{Pb\varepsilon}C_{\nu bT}|)^{-1}[(C_{PbT}\Delta\nu_b)+(-C_{\nu bT}\Delta P_b)]$$

$$\Delta T\ (K) = (|C_{\nu b\varepsilon}C_{PbT} - C_{Pb\varepsilon}C_{\nu bT}|)^{-1}[(-C_{Pb\varepsilon}\Delta\nu_b)+(C_{\nu b\varepsilon}\Delta P_b)] \qquad \{3.8\}$$

where the known coefficients from previous research are,

$C_{\nu b\varepsilon}$ =coefficient for change of Brillouin frequency shift with strain=0.048MHz/$\mu\varepsilon$ [18]

$C_{\nu bT}$ =coefficient for change of Brillouin frequency shift with temperature=1.1MHz/K [18]

$C_{Pb\varepsilon}$ =coefficient for change of Brillouin backscatter intensity with strain= -0.000903%/$\mu\varepsilon$ [19]

C_{PbT} =coefficient for change of Brillouin backscatter intensity with temperature=0.32%/K [2]

RMS errors in the Brillouin frequency shift, through transposition of the sampled & averaged data, and Brillouin backscatter intensity, through use of normalisation by the Rayleigh backscatter signal, can also be yielded as per figures 3.22 and 3.23 respectively. The errors can be calculated at A,B,C,D,E,F using a standard RMS error calculation method [20] which gives RMS errors of frequency and intensity at these 6 points. These errors can then be used in {3.9} to give the resolution error in temperature and strain.

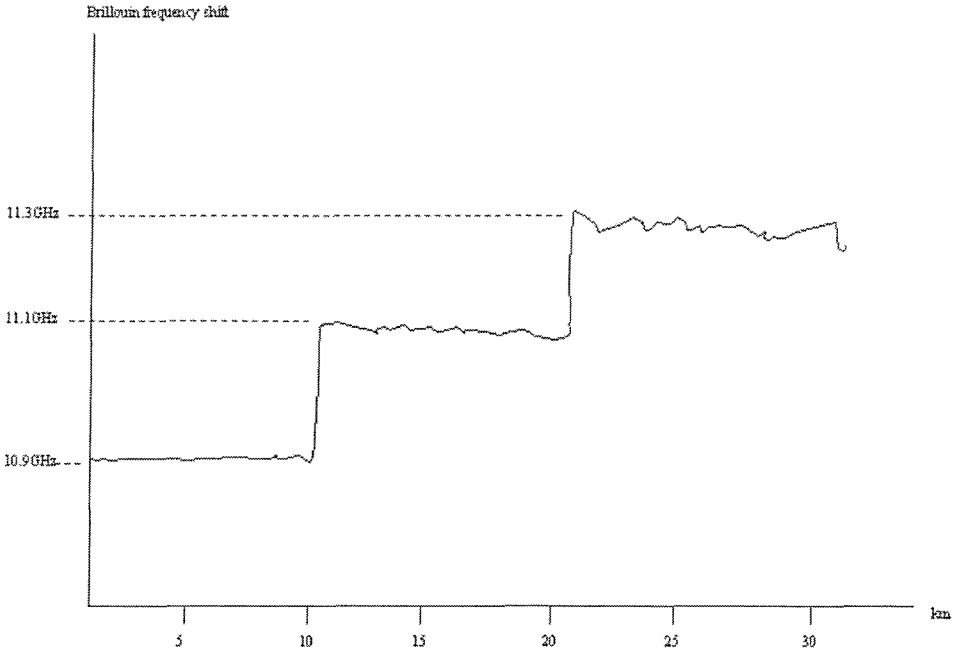

Figure 3.22 Three Anti-Stokes Frequency Shifts According to the Backscatter Traces in Figure 3.20. RMS Error can be Taken for Each of These Three Frequency Shifts so as to Give a Corresponding Error in Temperature and Strain Along the Fibre (When Used in Conjunction with the RMS Errors Found in Backscatter Intensity or LPR in Figure 3.23).

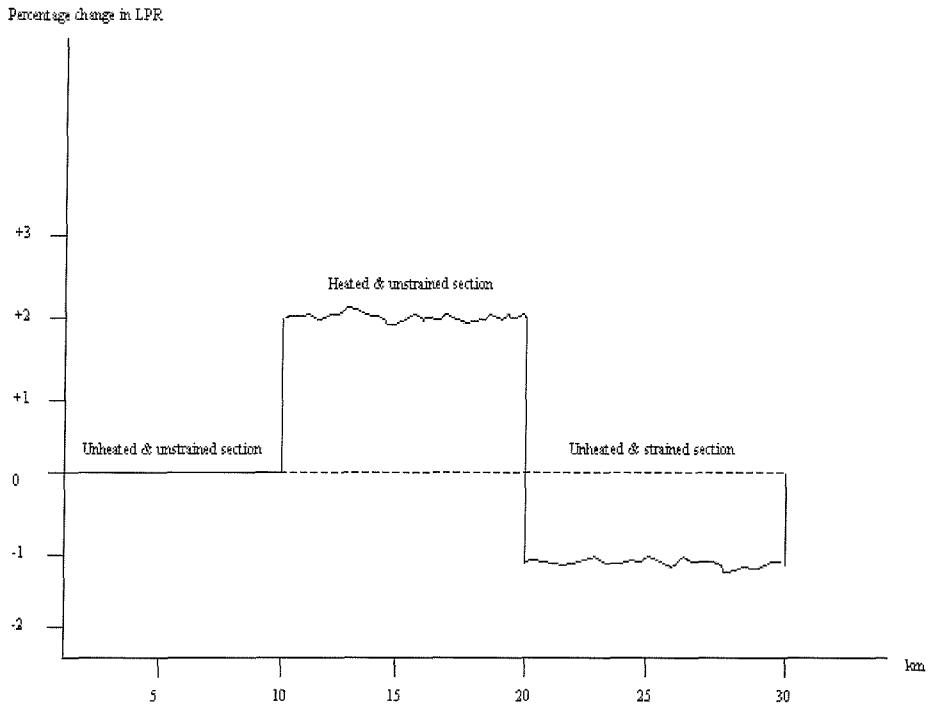

Figure 3.23 Three Normalised Anti-Stokes Intensity Changes (LPR) According to the Backscatter Traces in Figure 3.20. RMS Error can be Taken for Each of These Three LPR Scetions so as to Give a Corresponding Error in Temperature and Strain Along the Fibre (When Used in Conjunction with the RMS Errors Found in Brillouin Frequency Shifts in Figure 3.22).

Through use of the same set of coefficients just mentioned and the equations below the corresponding errors in temperature and strain resolution can be given.

$$| \delta\Delta\varepsilon\ (\mu\varepsilon)| = (|C_{vb\varepsilon}C_{PbT} - C_{Pb\varepsilon}C_{vbT}|)^{-1}\ [(|C_{PbT}|\delta\Delta\nu_b) + (|C_{vbT}|\ \delta\Delta P_b)]$$

$$| \delta\Delta T\ (K)| = (|C_{vb\varepsilon}C_{PbT} - C_{Pb\varepsilon}C_{vbT}|)^{-1}\ [(|C_{Pb\varepsilon}|\delta\Delta\nu_b) + (|C_{vb\varepsilon}|\ \delta\Delta P_b)] \qquad \{3.9\}$$

where δ denotes the measured RMS error on the variable in question.

The overall result of this is to give the temperature and strain values of the fibre together with their associated resolution with reference to an unstrained and unheated control fibre region. The final variable, spatial resolution along the fibre, is governed by the launched pulsewidth and the receiver IF resolution bandwidth.

Although greatly simplified from reality, this example demonstrates how it is possible to effectively translate backscatter traces into useful information regarding the temperature and strain at a region along an optical fibre. Moreover the backscatter traces can then be further employed to generate three dimensional graphs allowing the evolution of external forces such as temperature and strain to be observed as a function of distance along the fibre.

3.9 Conclusions

This chapter has given an insight into the challenges to overcome in order to progress beyond the use of conventional electronic systems such as the electronic spectrum analyser in an optical heterodyning fibre sensor. These challenges have inadvertently forced many sensor designs to be considered with regard to their suitability in an optical fibre sensor with increased spatial resolution. With the advantages and disadvantages discussed, this has lead to the finalising of a successor to the electronic spectrum analyser-based system being found. The new receiver for the optical fibre sensor is based on superheterodyne technology and has the advantage of being interchangeable to allow for a wide range of spatial resolutions to be employed simply through the tuning of the bandwidth filter. The theory behind superheterodyning, mixing and rectification has been demonstrated in this chapter. Components have been examined for their suitability and where deemed necessary have been purchased for the receiver.

The main components, those that are new or of importance, of the system have been included in the chapter and all information obtained on them is either given here or as a reference.

Finally, a simplified example of how the sensor operates has been demonstrated.
The following chapter will take the theory underpinning these components and use it to establish values used to engineer the optical fibre sensing system researched here.

3.10 References

[1] G.P.Lees, P.C.Wait, M.J.Cole and T.P.Newson, 'Advances in Optical Fiber Distributed Temperature Sensing Using the Landau-Placzek Ratio', *IEEE Photonics Technology Letters*, Vol.10, No.1, pp 126-128, (January 1998)

[2] P.C.Wait and T.P.Newson, 'Landau-Placzek ratio applied to Distributed Fibre Sensing', *Optics Communications*, Vol.122, No.4-6, pp141-146, (1996)

[3] J.M.Senior, 'Optical Fiber Communications: Principles and Practice. Second Edition', *Prentice Hall International Series In Optoelectronics*, ISBN 0-13-635426-2, (1992)

[4] S.M.Maughan, 'Distributed Fibre Sensing Using Microwave Heterodyne Detection of Spontaneous Brillouin Backscatter', Doctor of Philosophy Thesis, Department of Electronics and Computer Science, *University of Southampton*, (September 2001)

[5] D.M.Pozar, 'Microwave Engineering: First Edition', *Addison-Wesley*, ISBN 0-201-50418-9, (1990).

[6] 'ZHL-0812MLN Series Broadband Amplifier (SMA)' data sheet, *Mini-Circuits Europe*, www.mini-circuits.com/dg02-142.pdf

[7] 'DZ417 Zero Bias Schottky Detector' data sheet, *Omniyig Inc.*, www.omniyig.com

[8] J.Dunlop and D.G. Smith, 'Telecommunications Engineering: Third Edition', *Chapman & Hall*, ISBN 0-412-56270-7, (1994)

[9] G.Gonzalez, 'Microwave Transistor Amplifiers: Analysis & Design: Second Edition', *Prentice Hall*, ISBN 0-13-254335-4, (1997)

[10] S.M.Maughan, H.H.Kee and T.P.Newson, 'Simultaneous Distributed Fibre Temperature and Strain Sensor Using Microwave Coherent Detection of Spontaneous Brillouin Backscatter', IOP, *Measurement Science and Technology*, 12, pp. 834-842, (February 2001)

[11] E.Desurvire, 'Erbium-Doped Fiber Amplifiers: Principles and Applications', ISBN 0-471-58977-2.

[12] S.G.Grubb, W.F.Humer, R.S.Cannon, T.H.Windhorn, S.W.Vendetta, K.L.Sweeney, P.A.Leilabady, W.L.Barnes, K.P.Jedrzejewski and J.E.Townsend, '+21 dBm Erbium power amplifier pumped by a diode-pumped Nd:YAG laser', *IEEE Photonics Technology Letters*, Vol.4, No.6, pp.553-555, (1992)

[13] D.Maydan, 'Acoustooptical Pulse Modulators', *IEEE Journal of Quantum Electronics*, Vol. QE-6, No.1, pp.15-24 (January 1970)

[14] Agilent 83440B/C/D High-Speed Lightwave Converters' data sheet, *Agilent Inc.*, www.agilent.com/cm/rdmfg.converters/83440c/index.shtml

[15] 'M1-0412 Series Microwave Mixer' data sheet, *Marki Microwave Inc.*, www.markimicrowave.com/m1-0412.htm

[16] 'MLSL-0911 Series YIG Synthesiser' data sheet, *Micro Lambda Inc.*, www.microlambdawireless.com/mlslqam.htm

[17] K.Shimizu, T.Horiguchi, Y.Koyamada, T.Kurashima, 'Coherent Self-Heterodyne Brillouin OTDR for Measurement of Brillouin Frequency Shift Distribution in Optical Fibers', *Journal of Lightwave Technology*, Vol.12, No.5, pp 730-736, (1994)

[18] T.R.Parker, M.Farhadiroushan, V.A.Handerek and A.J.Rogers, 'A Fully Distributed Simultaneous Strain and Temperature Sensor using Spontaneous Brillouin Backscatter', *IEEE Photonics Technology Letters*, Vol.9, No.7, pp.979-981, (1997)

[19] K.De Souza, P.C.Wait and T.P.Newson, 'Characterisation of Strain Dependence of the Landau-Placzek ratio for distributed sensing', *Electronics Letters*, Vol.33, No.7, pp 615-616, (1997)

[20] University of Leicester, Department of Physics and Astronomy, 'Experiments in the First Year Undergraduate Laboratory', *University of Leicester*, (1992-1993)

Chapter 4 Theoretical Analysis Of The Distributed Optical Fibre Sensor

4.1 Theoretical Analysis And Modelling

The following chapter highlights areas of theoretical computer modelling such as those of noise and SNR that have been considered in the design process. The purpose of this modelling has been twofold; firstly to obtain an idea based on theory of values expected within or from the system and secondly to estimate values required for further engineering of the optical fibre sensor in order to facilitate optimisation.

The first area to be examined through the use of modelling is the action of backscatter itself. This includes a look at the power expected through Rayleigh backscatter and subsequently Brillouin backscatter for a particular pulse power and width launched down the sensing fibre. This leads on to limits that are encountered should too much power be launched down the fibre or should the pulse be too narrow.

The second area of the system to be investigated via modelling is noise since this tends to limit the system performance the most. Types of noise modelled in the system are also examined here. The noise analysed is then used to model the SNR that can be expected in the system leading to figures being generated for the final percentage error on any backscatter trace obtained. This percentage error, due to noise on the signal, is then plotted as a function of distance in order to enable an overview of the system performance to be expected.

Finally, from the literature provided for the microwave receiver components, the percentage intensity error and frequency shift error on the backscatter signal are estimated.

4.1.1 Rayleigh And Brillouin Backscatter

The following equations {4.1} and {4.2} are used to model the intensity of Rayleigh and Brillouin backscatter signals as a function of coefficients previously defined in {2.2}.

Rayleigh Backscattered Power=$0.5\{P_{in}W_o\gamma_R\upsilon_gSexp(-\upsilon_g\gamma_Rt)\}$ [1] {4.1}

Anti-Stokes or Stokes Backscattered Power= $(0.5/60)\{P_{in}W_o\gamma_R\upsilon_gSexp(-\upsilon_g\gamma_Rt)\}$ [2] {4.2}

The launching of a 140mW 100ns pulse, giving a spatial resolution of 10m, generates 110nW of optical Rayleigh power directly at the front end of a single mode sensing fibre where S=0.0016, $\upsilon g=2x10^8ms^{-1}$, $\gamma R=4.5x10^{-5}$. Since either the Stokes or anti-Stokes backscatter is given as 1/60 of this value, the value to be expected at the front end of the fibre is 1.8nW of optical power. As a function of distance this optical power falls exponentially as shown in figure 4.1.

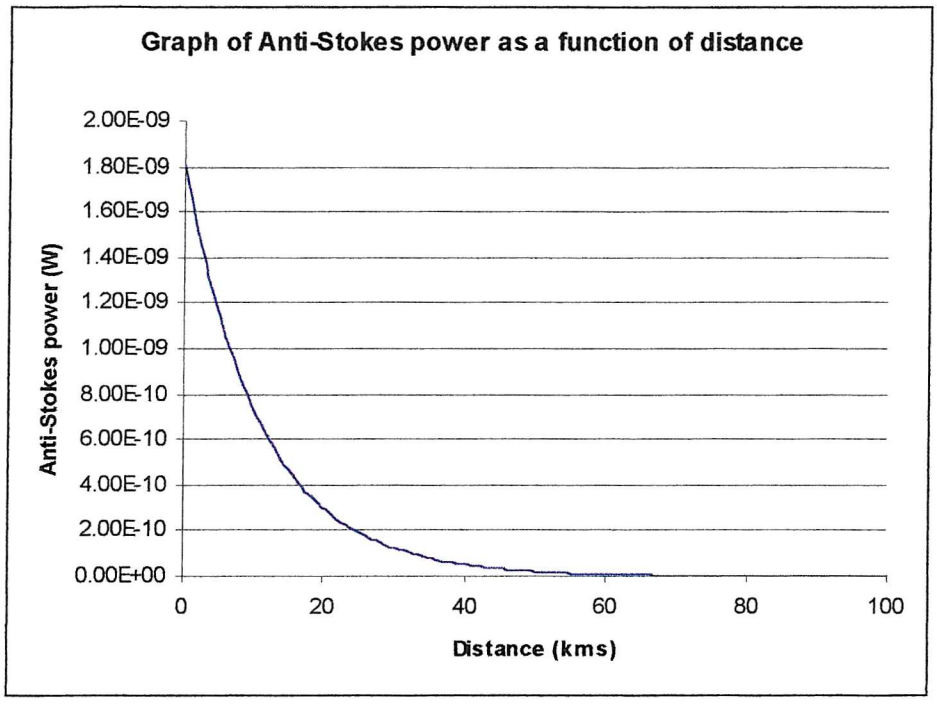

Figure 4.1 Anti-Stokes Power vs Sensing Distance.

For a 140mW 40ns pulse, giving a spatial resolution of 4m, the expected Rayleigh and anti-Stokes backscatter power merely fall as 40ns/100ns to give Rayleigh backscatter as 44nW of optical power with the corresponding anti-Stokes backscatter equalling 0.7nW directly at the front end of the sensing fibre.

Considering a reduction in launch power leads to the following. For a 110mW 100ns pulse, the Rayleigh backscatter is given as 86nW at the front end of the sensing fibre with the corresponding anti-Stokes power given as 1.43nW of optical power.

With these values seeming as small as they are, there is a temptation to increase the power launched in order to augment the backscatter power received so improving both the optical and electrical SNR of the optical fibre sensor to give greater temperature and strain resolution along a greater distance of sensing fibre. However, it is unfortunately not possible to greatly increase the power launched due to the following phenomena becoming prevalent at higher launch powers.

- Stimulated Raman Scattering (SRS)

When the input pump pulse power to a sensing fibre approaches a certain threshold, stimulated Raman amplification will occur and the pump power is effectively transferred to a frequency shifted Stokes signal 13THz away from the pump wavelength. [3] defines this threshold power as the input pulse power at which the output Stokes power equals the residual pump power at the fibre output. This can be expressed by

$$P_O^{th}=(16A_{eff})/(L_{eff}\, g_R) \qquad [2] \qquad \{4.3\}$$

where the effective area for conventional silica telecommunications fibre is $60\mu m^2$ [4], g_R is the Raman-gain coefficient ($1x10^{-13}m/W$) and the effective length is given by

$$L_{eff}=\alpha_P^{-1}[1-\exp(-\alpha_P L)] \qquad [2] \qquad \{4.4\}$$

where α_P is the absorption of the pump pulse ($5x10^{-5}m^{-1}$ for silica fibre) in the sensing fibre and L is the sensing fibre length.

With the frequency separation of the Stokes and pump wavelengths being of the order of 13THz, another effect becomes dominant and modifies the effective length for short pump pulses (<30ns). This effect arises from the dispersive nature of optical fibre and causes the pump and Stokes pulses to separate after a certain distance down the sensing fibre and hence to cease to interact. This distance, known as the walk-off length, is given by

$$L_W=W/[D(\lambda_S-\lambda_P)] \qquad [2] \qquad \{4.5\}$$

where W is the pulse width, D is the fibre dispersion coefficient (17ps/km/nm for standard silica telecommunications optical fibre) and λ_S-λ_P is the wavelength separation between the pump and Stokes signals.

- Stimulated Brillouin Scattering (SBS)

With an incident signal of high intensity and narrow linewidth, a much stronger backscattered signal due to the reinforcement of the acoustic waves by the process of electrostriction between the pump beam and the thermally generated acoustic waves occurs and is known as stimulated Brillouin scattering. A similar equation for the threshold level at which this occurs to that for stimulated Raman scattering is given as

$$P_O^{th}=(21A_{eff})/(L_{eff}\, g_B) \qquad [2] \qquad \{4.6\}$$

where all coefficients are the same as those of the Raman case except that g_R is replaced by the Brillouin gain-coefficient g_B ($=6\times10^{-11}$m/W) [2]. As long interaction lengths and high power densities can often occur in a fibre core any pump light can generate both Brillouin and Raman Stokes shifted light. Above the threshold powers given in {4.6} and {4.3}, these shifted light wavelengths are observed to build up exponentially. This can lead to almost all of the pump power being converted to these Stokes shifted wavelengths hence reducing any sensing range. {4.3} and {4.6} effectively set upper limits on optical peak pulsed power which can be launched down a sensing fibre.

Modelling enables threshold values to be generated for these phenomena which should not be exceeded should the optical fibre sensor be used to give meaningful temperature and strain resolution along a sensing fibre.

For a 100ns pulse and 20km sensing length,

L_W=58.8km

SRS=836mW

SBS=2.5W

(with L_{eff}=12.6km)

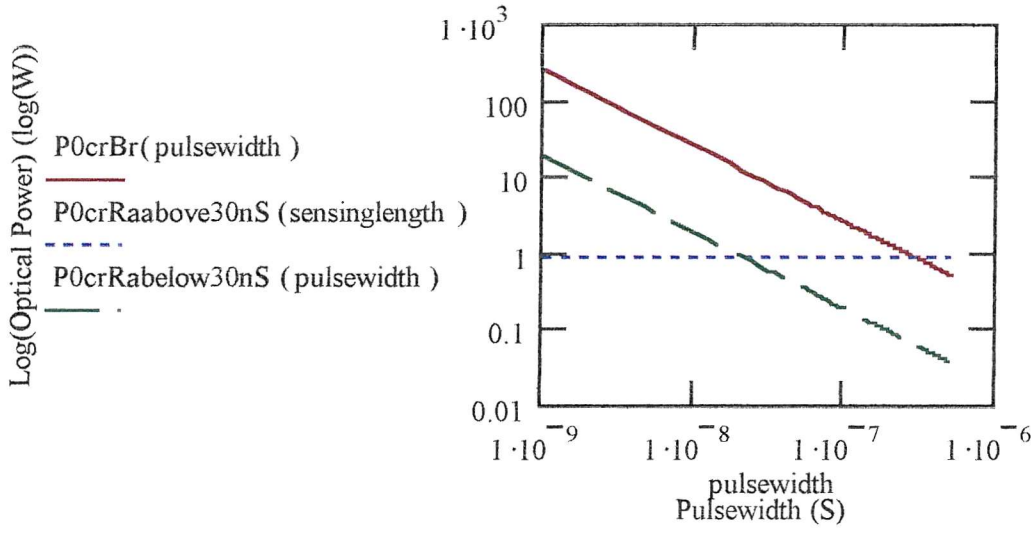

Figure 4.2 Threshold Limits for Distributed Fibre Optic Sensing as a Function of Launched Optical Pulsewidth. Red Line (P0crBr) is Threshold Limit for Stimulated Brillouin Scattering, Blue Line (P0crRaabove30ns) is Threshold Limit for Stimulated Raman Scattering Using a Launched Pulse of > 30ns Duration (Taken at 20km Sensing Since the Threshold Limit Decreases with Increasing Sensing Length), Green Line (P0crRabelow30ns) is Threshold Limit for Stimulated Raman Scattering Using a Launched Pulse of < 30ns Duration.

For a 40ns pulse and 20km sensing length,

L_W=23.5km

SRS=836mW

SBS=6.2W

(with L_{eff}=12.6km)

It would appear from {4.3} and {4.6} that the SBS threshold will always be lower for any given length of fibre and pump wavelength so contradicting what is observed in figure 4.2.

Equations {4.3} and {4.6} work for the case of a cw pump, however optical pulses require calculations of threshold power to be made according to whether the scattering is Brillouin or Raman in nature. Due to the backward-propagating nature of stimulated Brillouin scattering, an interaction length replaces L in {4.4} over which the pump and Stokes wave overlap (which is the fibre length for the cw pump case) and will be half of the fibre length occupied by the pump pulse or the fibre length itself, whichever is shorter. The effect of this is to greatly increase the SBS threshold for short pulses.

Raman scattering however is a forward-propagating phenomenon and a pulsed pump input will suffer from 'walk-off' whereby the Raman and pump pulses are no longer coincident after a certain distance as given by {4.5}. The interaction length in this instance will be either the walk-off length or the fibre length, whichever is smaller. This causes the Raman threshold to rise for very short pulses but to tend to a steady state value for longer pulses.

This phenomenon demonstrates how the effective length given in {4.4} is different for SBS and SRS under pulsed conditions. This leads to the SRS threshold being the first threshold encountered as seen in figure 4.2 and in the accompanying calculations. This threshold is above those calculated in previous research [5] to which the research conducted here is to adhere.

4.1.2 Noise Analysis

Noise analysis is inherently complex within the realm of optical fibre sensing due to the small optical powers that are present within any optical fibre sensor. Effectively, these small powers are not much greater than the noise power inherent within any detection system meaning a low SNR at the detector output. However good estimates for calculating the value of noise have been generated and these can be used to give a useful approximation to the combined noise that can be expected on any backscatter trace that is to be quantified.

4.1.2.1 Types Of Noise

The following gives an insight in to the types of noise that were analysed in this research for the purposes of obtaining an insight into the final performance of the sensor.

4.1.2.1.1 Local Oscillator Shot Noise

The detection of light by a photodiode is a discrete process since the creation of an electron-hole pair results from the absorption of a photon, and the signal emerging from the detector is dictated by the statistics of photon arrivals. However random fluctuations of charge carriers during photodetection can impose a noise on the output photocurrent which does not obey this statistical nature. This is shot noise and is due to the random movement of charge carriers across a p-n junction within a semiconducting material.

The shot noise current on the photocurrent I_P is given by,

$$\langle i_S^2 \rangle = 2eBI_P \qquad \{4.7\}$$

where e is electronic charge
B is receiver bandwidth

The output photocurrent from {2.21} I_P given as,

$$I_P = \eta P_0 e/hf$$

Hence assuming the photocurrent generated by the local oscillator signal to be the major contribution to the photocurrent this gives the mean shot noise generated by the local oscillator signal to be

$$\langle i_{SL}^2 \rangle = 2e^2 \eta P_L B/hf \qquad \{4.8\}$$

where P_L is the incident local oscillator power in Watts

4.1.2.1.2 Relative Intensity Noise

Fluctuations in the amplitude or intensity of the output from semiconductor injection lasers leads to optical intensity noise. These fluctuations may be caused by temperature variations, or alternatively, they result from the spontaneous emission contained in the laser output. The random intensity fluctuations create a noise source referred to as relative intensity noise (RIN), which may be defined in terms of the mean square power fluctuation $\langle \delta P_e^2 \rangle$ and the mean optical power squared ($\langle P_e \rangle^2$) which is emitted from the following

$$RIN = \langle \delta P_e^2 \rangle / \langle P_e \rangle^2 \qquad \{4.9\}$$

{4.9} allows the RIN to be measured in dB/Hz where the power fluctuation is written as

$$\langle \delta P_e^2 \rangle(t) = \int S_{RIN}(f)\, df \qquad \{4.10\}$$

between the frequency limits of 0 and ∞. $S_{RIN}(f)$ is related to the power spectral density of the relative intensity noise $S_{RIN}(\omega)$ by

$$S_{RIN}(f) = 2\pi\, S_{RIN}(\omega) \qquad \{4.11\}$$

where $\omega = 2\pi f$.

Hence from {4.9}, the RIN as a relative power fluctuation over a bandwidth B of 1Hz is

$$RIN = [S_{RIN}(f).B(1Hz)] / \langle P_e \rangle^2 \qquad \{4.12\}$$

Typically the RIN for a single-mode semiconductor laser lies in the range -130 to -160dB/Hz. However it should be noted that the relative intensity noise decreases as the injection current level I increases following the relation [6]

$$RIN \propto (I/I_{th})^{-3} \qquad \{4.13\}$$

where I_{th} is the laser threshold current.

From {2.21} the relationship between incident optical power and output photocurrent is known. Applying this relationship in this instance gives

$$\delta I_P(t) = \delta P_O(t).\eta e/(hf) \qquad \{4.14\}$$

where $\delta P_O(t)$ is the fluctuation in incident optical power due to the RIN and $\delta I_P(t)$ is the resulting fluctuation in output photocurrent which is superimposed on the output photocurrent. This exhibits a mean square value given as

$$\langle i^2 \rangle(t) = \langle \delta I_P^2 \rangle(t) = [\langle \delta P_O^2 \rangle(t).\eta^2 e^2]/(hf)^2 \qquad \{4.15\}$$

Considering the fluctuation in the incident optical power at the detector to result from the RIN in the laser emission leads to a final mean square noise current in the output of the detector due to RIN being described as

$$\langle i_{RIN}^2 \rangle = [(RIN).B.\langle P_e \rangle^2.\eta^2 e^2]/(hf)^2 \qquad \{4.16\}$$

The RIN is assumed to mostly eminate from the optical local oscillator due to the high intensity of laser light from it.

4.1.2.1.3 Dark Current Noise

When there is no optical power incident on the photodetector a small reverse leakage current still flows from the device terminals. This dark current contributes to the total system noise and gives random fluctuations about the average particle flow of the photocurrent. It therefore manifests itself as shot noise [7] [8] on the photocurrent. Thus the mean square dark current noise is given by

$$\langle i_d^2 \rangle = 2eBI_d \qquad \{4.17\}$$

where e is the charge on an electron and I_d is the dark current. It may be reduced by careful design and fabrication of the detector.

4.1.2.1.4 Thermal Noise

This is the spontaneous fluctuation due to thermal interaction between the free electrons and the vibrating ions within a conducting medium, and it is especially prevalent in resistors at room temperature.

The thermal noise current it in a resistor R may be expressed by its mean square value[4] and is given by

$$\langle i_t^2 \rangle = 4kTB/R \qquad \{4.18\}$$

where k is Boltzmann's constant, T is the absolute temperature and B is the post-detection (electrical) bandwidth of the system (assuming the resistor is in the optical receiver).

4.1.2.1.5 Polarisation Noise

Single mode fibres exhibit an additional problem over multimode devices, namely polarization noise. In general, the state of polarization of the backscattered light differs from that of the laser pulse coupled into the fibre at the input end and is dependent on the distance of the backcscattering fibre element from the input fibre end. This results in an amplitude fluctuation in the backscattered light kown as polarisation noise. A polarization scrambler [9], for the purposes of this research, has been obtained and added to the system. The analysis and evaluation of results obtained, while acknowledging that the polarization scrambler has been efficient in reducing polarization noise, does not take into consideration any effects, be they beneficial or detrimental, by this component. For a fuller analysis of polarization noise the reader is directed toward prior research [10].

4.1.2.1.6 Noise Figure Of Microwave Receiver

Any component added to an already existant receiver will inherently add noise and in some instances will worsen the SNR that can be expected at the output. A compromise can be seen to exist since amplification of a signal is often required but the addition of an amplifier to the system will add additional noise to it. A noise figure can be specified for any system whereby,

$$\text{Noise figure F (dB)} = SNR_{input}/SNR_{output} \quad \{4.19\}$$

Extending this principle to a cascaded network of microwave components leads to the following equation describing the total noise figure of a microwave network

$$F_{cascaded}=F_1+[(F_2-1)/G_1]+[(F_3-1)/G_1G_2]+.... \quad \{4.20\}$$

where the components that comprise a system are labelled in a numerically increasing order from system input to output and F is the noise figure of each component and G is the gain of each component.

4.1.2.1.7 Phase Noise

Any sinusoidal signal, unless ideal in nature, will suffer from amplitude noise and phase noise. This is commonly noted as

$$s(t)=(A+a(t))\sin(\omega t+\phi(t)) \quad \{4.21\}$$

where s(t) represents a sinusoidal signal, A is the ideal amplitude of the sinusoid, a(t) is a time-varying amplitude noise on the signal, ωt is the ideal phase of the sinusoid and $\phi(t)$ is a time-varying phase noise on the signal. Whereas the amplitude noise is affects only the amplitude of the sinusoid, the phase noise only affects the 'zero crossings' of the sinusoid. This is observed as a jitter in the time, hence frequency, domain of the signal.

Figure 4.3 demonstrates the principle.

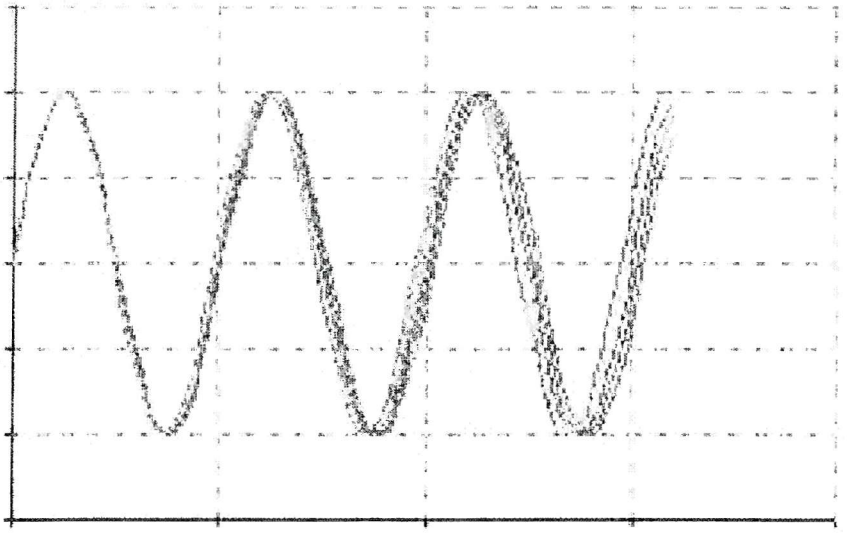

Figure 4.3 Phase Noise Manifesting Itself on a Sinusoid

The local oscillator signal within the microwave section of the Brillouin sensor is generated by an Yttrium Iron Garnet (YIG) digital frequency synthesizer which is accompanied with literature giving values of phase noise at various frequencies away from the generated and required centre frequency. The values are –53dBc/Hz @ 100Hz, -60dBc/Hz@1kHz, -87dBc/Hz@10kHz, -110dBc/Hz@100kHz and –133dBc/Hz @ 1MHz where dBc is a decibel ratio measurement of noise power relative to the required output signal power.

Through a process of integration of this quoted spectral purity of the YIG signal, the result of the frequency variation as a function of phase noise is obtained. The value is calculated as $\pm 1.34 kHz_{pk\text{-}pk}$ and suggests that, as anticipated, the YIG synthesizer produces an extremely pure signal.

4.2 Models Generated To Calculate Sensor SNR (Including Preamplification Of 14dB)

Using the information on signal and noise given above, models were constructed to give information with regard to SNR at any point along the optical fibre sensor. Care was taken to ensure that optical powers and electrical powers were treated accordingly.

An example of this being that 0dBm optically is given as equalling –16dBm electrically.

For the noise terms described above the corresponding models showed the following results:

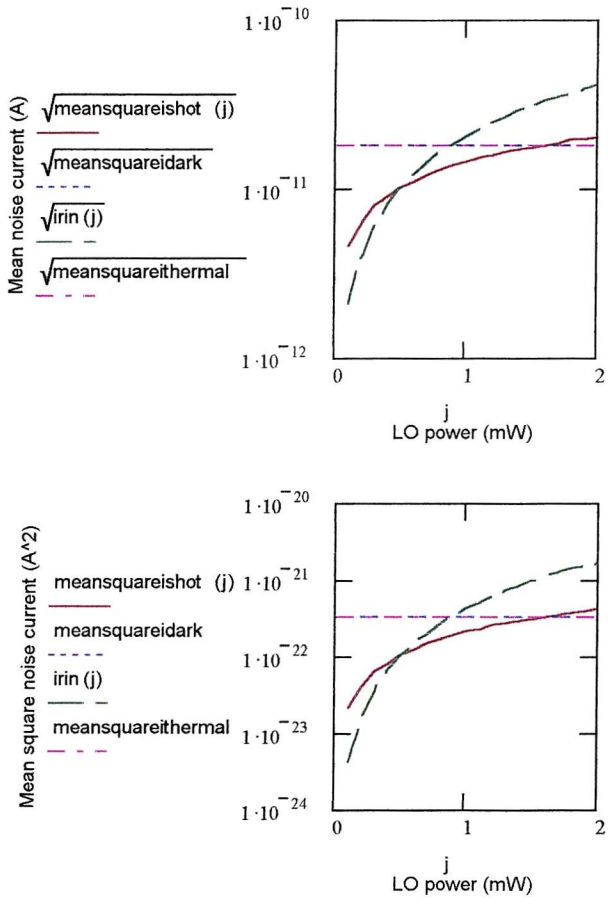

Figure 4.4 Mean Optical Noise Current as a Function of Local Oscillator Power (Top), Mean Squared Optical Noise Current as a Function of Local Oscillator Power (Bottom).

Figure 4.4 demonstrates the pure optical noises that are predominant at the lightwave detector within the sensor; these noises being RIN noise (introduced by P.C.Wait through meetings with a local optical technology company), local oscillator shot noise

and dark current noise (equivalent to thermal noise). They are given here as a total noise in a 1Hz BW equalling -161dBm for a 1.3mW local oscillator signal strength.

The information forthcoming from the models bearing the most significance suggested that:

- For a 110mW 100ns pulse, the noise expressed as a percentage error on the signal would be 0.05% for 65536 averages at the front end of the fibre, suggesting a ±0.17°C temperature resolution and ±55με strain resolution, both these results being comparable to previous research [10]. For 20km sensing the results would be 0.13%(±0.43°C & ±140με) and for 40km sensing the results would be 0.24% (±0.8°C & ±260με). The voltage output from the diode rectifier would be 28.5mV at the front end of the fibre.

- For a 140mW 100ns pulse, the noise expressed as a percentage error on the signal would be 0.04% for 65536 averages at the front end of the fibre, suggesting a ±0.13°C temperature resolution and ±40με strain resolution, both these results being comparable to previous research [10]. For 20km sensing the results would be 0.1% (±0.35°C & ±110με) and for 40km sensing the results would be 0.2% (±0.7°C & ±230με). The voltage output from the diode rectifier would be 36.3mV at the front end of the fibre.

- For a 140mW 40ns pulse, the noise expressed as a percentage error on the signal would be 0.1% for 65536 averages at the front end of the fibre, suggesting a ±0.35°C temperature resolution and 110±με strain resolution, both these results being comparable to previous research [10]. For 20km sensing the results would be 0.18%(±0.6°C & ±190με) and for 40km sensing the results would be 0.5% (±1.7°C & ±600με). The voltage output from the diode rectifier would be 14.5mV at the front end of the fibre.

Figure 4.5 gives these modelled results in table form.

Pulse power (mW)	Pulsewidth (ns)	Averages	Sensing distance (km)	Diode Rectifier Output Voltage (mV)	Noise (% of signal power)	Derived temp. resolution (±K)	Derived strain resolution (±με)
110	100	65536	0	28.5	0.05	0.17	55
		65536	20		0.13	0.43	140
		65536	40		0.24	0.8	260
140	100	65536	0	36.3	0.04	0.13	40
		65536	20		0.1	0.35	110
		65536	40		0.2	0.7	230
140	40	65536	0	14.5	0.1	0.35	110
		65536	20		0.18	0.6	190
		65536	40		0.5	1.7	600

Figure 4.5 Modelled Diode Rectifier Output Voltage Together with Noise as a Percentage of Signal Intensity and Derived Strain and Temperature Resolutions for Various Pulse Forms Using an SNR-Based Modelling Technique.

All these values are based on coefficients found in previous work [11], [12], [13] and have been calculated using a SNR approach whereby all components of the sensor contribute noise leading to a final SNR at the sensor output.

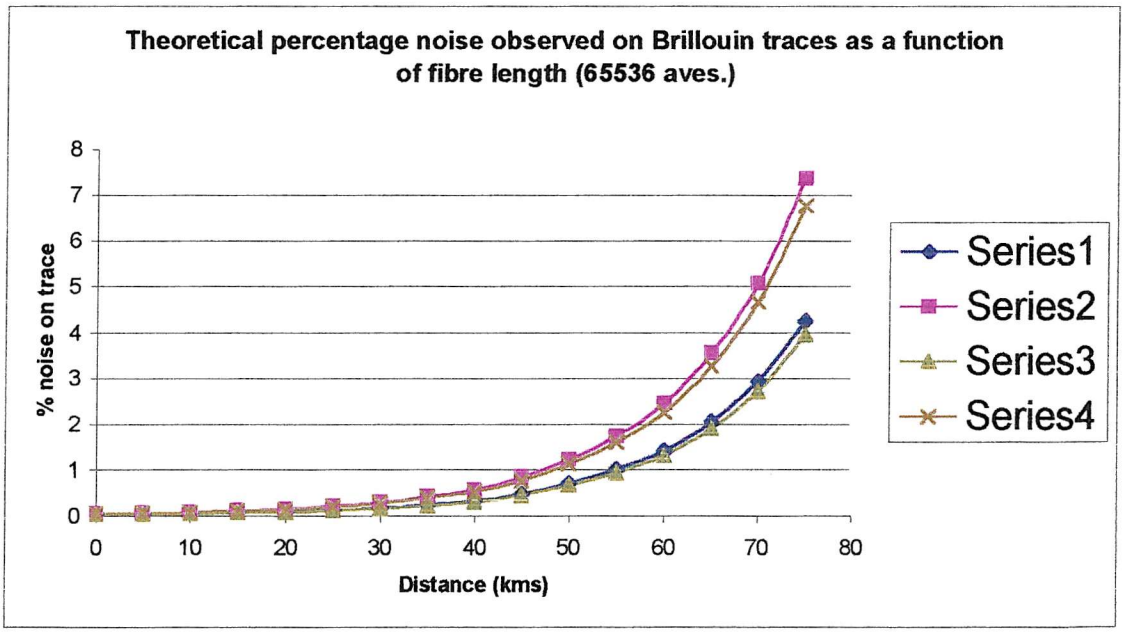

Figure 4.6 Theoretical Percentage Noise on Anti-Stokes Backscatter Traces as a Function of Fibre Length (65536 Averages).

Figure 4.6 shows four theoretical traces. Series 1 shows the 100ns 140mW results as described above. Series 2 shows the 40ns 140mW results as described above. Series 3 show the results of a noise analysis on a 100ns 140mW launched pulse signal employing an approach using data from figure 4.4 where noise is given as a function of local oscillator power. Finally series 4 demonstrates the results of this local oscillator-based noise analysis for a 40ns 140mW pulse.

Good agreement between both analysis methods can be seen. From this graph it can be seen that for the noise to be no greater than 0.3% as required for ±1°C temperature resolution the maximum sensing distance should not exceed should 25km for 4m spatial resolution. In the case of strain resolution of ±100με, the noise should be no greater than 0.1% which would mean not exceeding 0km sensing for 4m spatial resolution.

It is not feasible to obtain the strain resolution unless additional averages are employed. This is not wanted as 65536 averages are already being considered. With this in mind it would seem reasonable to aim at a 20km sensor while concentrating on the temperature resolution as the principal resolution to be measured. This sensing distance should allow for reasonable conclusions to be drawn from any analysis performed in this region of the fibre.

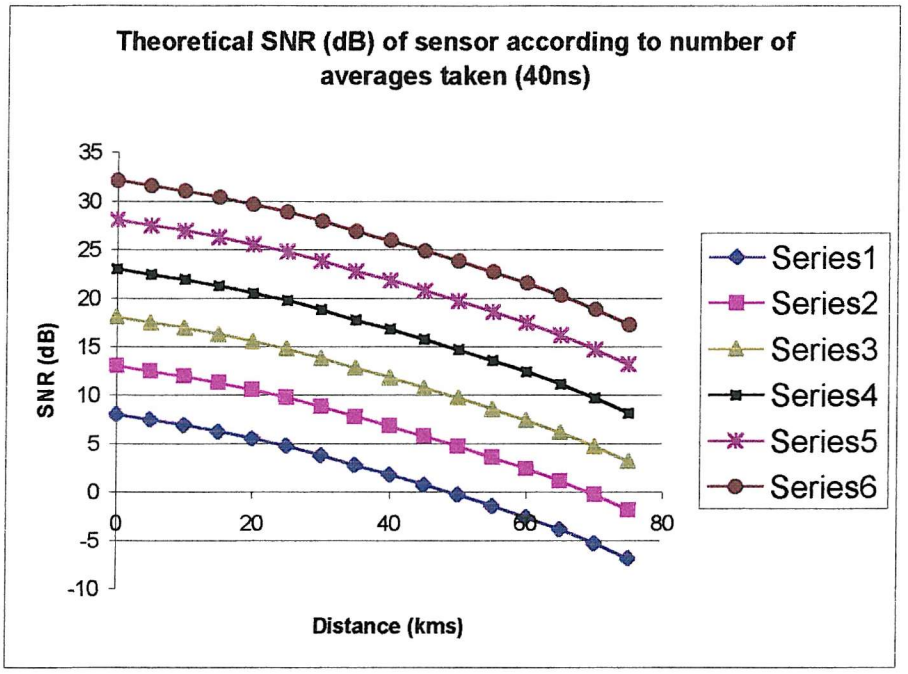

Figure 4.7 Theoretical SNR (dB) of Sensor According to Number of Averages vs Distance (40ns Pulsewidth or 4m Spatial Resolution).

Figure 4.7 shows how the number of averages influences, at least theoretically, the SNR at the sensor output. Series 1 is with 1 average, series 2 with 10, series 3 with 100, series 4 with 1000, series 5 with 10 000 and finally series 6 is with 100 000 averages. An equation for frequency shift error has previously been suggested by Shimizu et al. [14]:

$$\delta\nu_B=\Delta\nu_B/[(\sqrt{2})(SNR)^{0.25}] \qquad \{4.22\}$$

where

$\Delta\nu_B$=35MHz (Brillouin linewidth)
SNR=30dB (at front end of fibre for approximately 65536 averages)

This gives the frequency error as 4.4MHz (±4°C) which seems far larger than the equivalent intensity error of ±0.35°C for a 140mW 40ns pulse at the front end of the fibre. The largeness of the frequency shift error produced by this formula has been commented on in previous work [10]. Figure 4.8 demonstrates the frequency shift error according to Shimizu et al. as a function of distance. The blue line represents a

linewidth of 35MHz with the pink line representing a linewidth of 90MHz, the actual linewidth observed in the research conducted for this thesis.

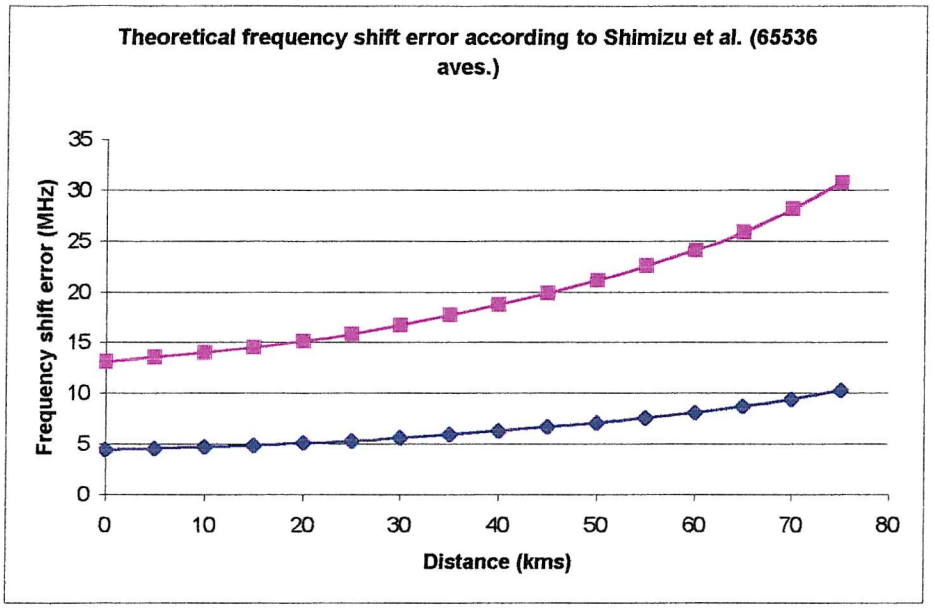

Figure 4.8 Theoretical Frequency Shift Error vs Distance According to Shimizu et al. for 65536 Averages. (Blue Line (with Diamonds) Represents 35MHz Linewidth, Pink Line (with Squares) Represents 90MHz Linewidth).

4.3 Frequency Shift And Power Errors According To Literature Supplied With Microwave Components

As a variant method to the calculation of errors generated on any signal analysed by the sensor described above, the following error analysis was generated from the literature supplied with the microwave components. This is useful in that it provides a second solution to the frequency shift error as calculated using the method given by Shimizu et al [14].

4.3.1 Intensity Error

Power calibration of the microwave receiver requires calibrating the microwave mixer, YIG synthesiser and lightwave detector frequency responses only since the IF section of the receiver only ever receives a 1GHz intensity-varying IF signal. Hence any error on the intensity is proportional to the noise sources described above and to the frequency resolution of the frequency responses of the three components named above to be used in calibrating the system. As regards the calibration of these components,

figure 4.9(b) shows a theoretical power-frequency scaling coefficient graph (blue line) generated from literature supplied with each microwave component together with a measured power-frequency scaling graph (pink line) generated through the use of a Marconi 8210 network analyser test set. Figure 4.9(a) is an identical measurement to the pink measured line in figure 4.9(b) except that measurements are made in 5MHz steps across the same frequency range of 10.7-11.5GHz. A low power signal of -60dBm was input to the microwave mixer over the frequency range of figure 4.8 and the measured power output at each measured frequency was scaled as shown. It can be seen that there is good agreement between the theoretical and measured values. During the measurements the lightwave detector was not able to used due to the frequency range of signal supplied by the Marconi 8210 test set. However, as no frequency-power scaling issues have been mentioned in research prior to this, it seems reasonable to scale only the components that have been classed as new to the system. Previous work has not needed scaling in this way since the receiver has been one generic piece of equipment, namely the electronic spectrum analyser.

The values from this figure have been input to the sensor control code and are used as scaling coefficients on final averaged data sets at each frequency.

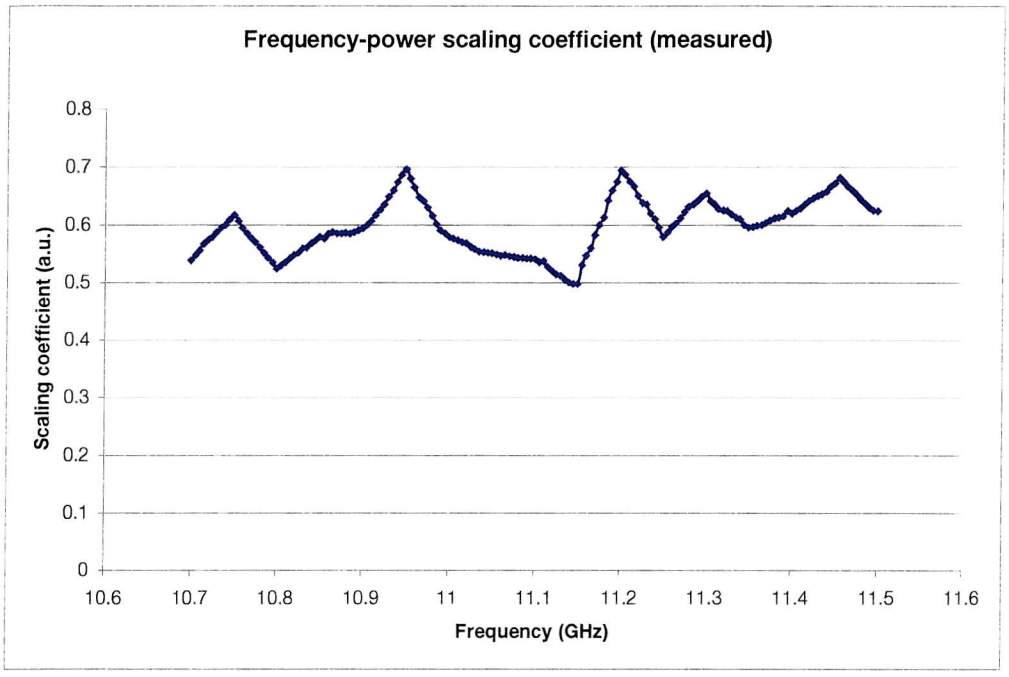

Figure 4.9(a) Frequency-Power Scaling Coefficient With Data Taken at 5MHz Steps Across the Frequency Range of 10.7-11.5GHz.

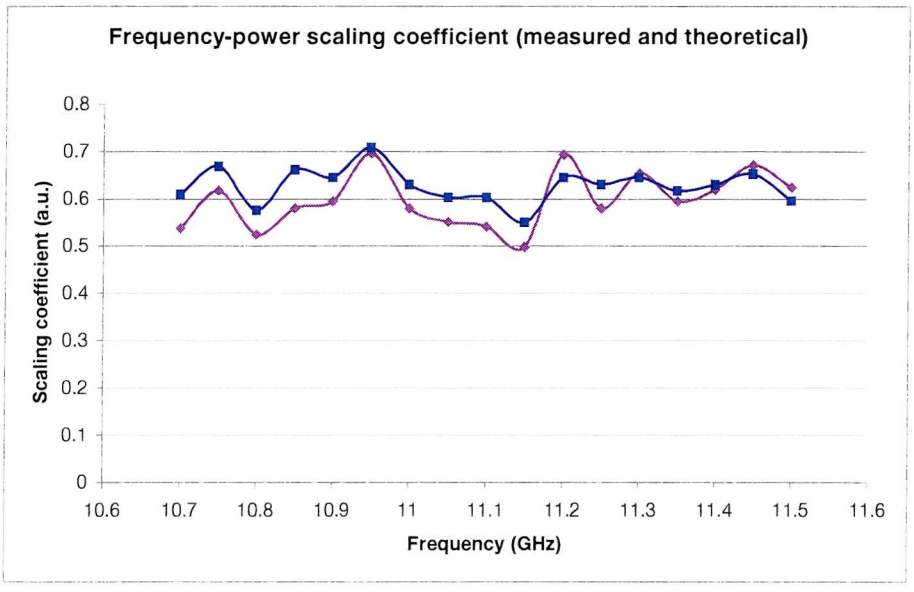

Figure 4.9(b) Frequency-Power Scaling Coefficient Comparison Between Manufacturer's Data and Measured Data (Blue Line (with Squares) is Theoretical From Manufacturer's Data, Pink Line (with Diamonds) is Measured).

4.3.2 Frequency Shift Error

From literature supplied with each microwave component the following frequency shift error has been found.

- Phase noise of the YIG synthesiser translates itself as a frequency shift error on the received signal. The phase noises with reference to the desired centre frequency and as a function of frequency distance away from this desired frequency are given in 4.1.2.1.7. This error is ±1.34kHz [15].

- The reference oscillator used to control the frequency of the YIG synthesiser has a coefficient of ageing describing the variation in output frequency with time due to crystal degradation. This error is ±55Hz for 10MHz output from the reference oscillator as quoted by the literature accompanying this component which translates to a YIG synthesiser ageing frequency shift error of {55Hz x (10.5GHz[worst case]/10MHz)} equalling ±57.75kHz over 1 year.

- Minimum detectable change in Brillouin frequency shift. Error=±398kHz (optical system) [16].

- The YIG synthesiser has a minimum step size introducing a step size error of ±250kHz as quoted by its accompanying literature.

These four figures added together demonstrate an error of just ±707.09kHz. This suggests a substantial difference to the value generated through the use of the equation by Shimizu et al [14].

4.4 Conclusions

Throughout this chapter, the emphasis has been on reducing any analysis down to core modules that can be easily used for generating values necessary in the evaluation of the sensor performance. These core modules have included signal powers together with associated noise errors that have lead to SNRs being calculated for the sensor. Several variants of noise analysis have been shown which suggest that for fibre lengths below

25km there is a good likelihood of obtaining data allowing for a constructive evaluation of the sensor. Beyond this length, it seems that noise on the signal increases to a value whereby the resolution specified for the sensor exceeds limits set. As regards frequency shift error, two models have been shown, one being literature based with the other being calculated according to Shimizu et al. [14]. Research prior to this has brought the latter into question as regards its accuracy while the former demonstrates results similar to those generated by the same prior research [10].

Values have been generated showing the output voltage anticipated from the sensor output and expected noise on the signal together with the resulting temperature and strain resolution. These values have been generated as an aid to sensor development and do not in any case represent the expected final resolution.

Improvements to the noise analysis could have been made by including Self-Phase Modulation effects together with Brillouin, Rayleigh and Local Oscillator Self-Beat and Cross-Beat Terms. ASE beat terms could also have been included. These were not employed due to the author wishing to keep noise analysis as simplified as possible while enabling a satisfactory sensor to be constructed.

4.5 References

[1] S.D.Personick, 'Photon-probe- An optical-fiber time domain reflectometer', *Bell System Technical Journal*, Vol.56, No.3, pp.355-366, (1977)

[2] G.P.Agrawal, 'Nonlinear Fiber Optics. Second Edition', *Academic Press*, ISBN 0-12-045142-5, 1995

[3] R.G. Smith, 'Optical power handling capacity of low loss optical fbers as determined by stimulated Raman and Brillouin scattering', *Applied Optics*, Vol.11, No.11, pp. 2489-2494, (1972)

[4] D.Marcuse, 'Theory of Dielectric Optical Waveguides: Second Edition', *Academic Press*, ISBN 0-124-70951-6, (1991)

[5] S.M.Maughan, H.H.Kee and T.P.Newson, 'Simultaneous Distributed Fibre Temperature and Strain Sensor Using Microwave Coherent Detection of Spontaneous Brillouin Backscatter', IOP, *Measurement Science and Technology*, 12, pp. 834-842, (February 2001)

[6] J.M.Senior, 'Optical Fiber Communications: Principles and Practice. Second Edition', *Prentice Hall International Series In Optoelectronics*, ISBN 0-13-635426-2, (1992)

[7] M.Schwarz, 'Information Transmission, Modulation and Noise', (4^{th} edition), *McGraw-Hill*, (1990)

[8] F.R.Conner, 'Noise', (2^{nd} edition), *Edward Arnold*, (1982).

[9] M.Tateda and T.Huriguchi, 'Advances in optical time-domain reflectometry', *Journal of Lightwave Technology*, 7(8), pp. 1217-1224, (1989)

[10] S.M. Maughan, "Distributed Fibre Sensing Using Microwave Heterodyne Detection of Spontaneous Brillouin Backscatter", Doctor of Philosophy Thesis, Department of Electronics and Computer Science, *University of Southampton*, (September 2001)

[11] T.R.Parker, M.Farhadiroushan, V.A.Handerek and A.J.Rogers, 'A Fully Distributed Simultaneous Strain and Temperature Sensor using Spontaneous Brillouin Backscatter', *IEEE Photonics Technology Letters*, Vol.9, No.7, pp.979-981, (1997)

[12] K.De Souza, P.C.Wait and T.P.Newson, 'Characterisation of Strain Dependence of the Landau-Placzek ratio for distributed sensing', *Electronics Letters*, Vol.33, No.7, pp 615-616, (1997)

[13] P.C.Wait and T.P.Newson, 'Landau-Placzek ratio applied to Distributed Fibre Sensing', *Optics Communications*, Vol.122, No.4-6, pp141-146, (1996)

[14] K.Shimizu, T.Horiguchi, Y.Koyamada, T.Kurashima, 'Coherent Self-Heterodyne Brillouin OTDR for Measurement of Brillouin Frequency Shift Distribution in Optical Fibers', *Journal of Lightwave Technology*, Vol.12, No.5, pp 730-736, (1994)

[15] Aeroflex Comstron, 'Application Note#1: Phase Noise Theory and Measurement', *www.aeroflex.com/comstron/*, (Revised 14.03.95)

[16] T.Horiguchi, T.Kurashima, Y.Koyamada, 'Measurement of temperature and strain distribution by Brillouin frequency shift in silica optical fibers', NTT Telecommunication Field Systems R&D Center, Tokai, Ibaraki-Ken, 319-11, Japan, *Proc. O/E Fibers*, Boston, (Sept. 1992)

Chapter 5 Temperature & Strain Sensing

5.1 Measurements Before System Is Operational

In order to extend the theoretical work already carried out it was necessary to continue with practical measurements before finally taking some experimental results. The results taken were merely meant to point to areas where the sensor was performing according to the models as well as areas where it was not.

5.1.1 Optical Power Measurements

Figure 5.1 below shows power measurements taken throughout the system during its construction. These measurements were included in any models that were generated in order to give the values quoted in the chapter 4.

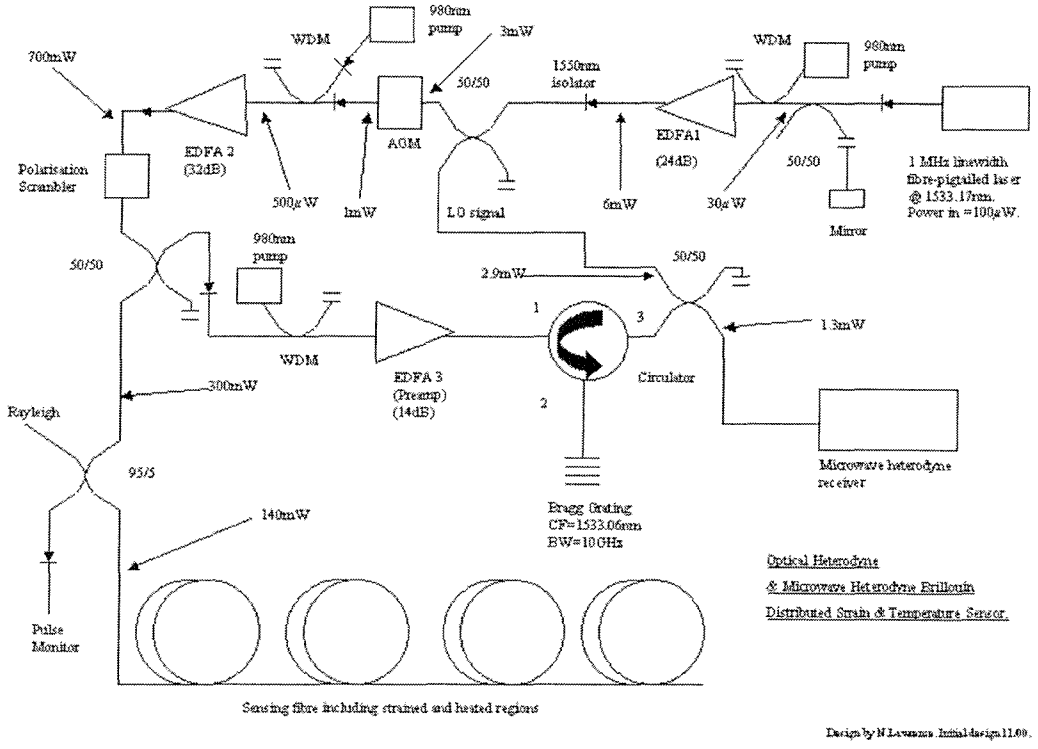

Figure 5.1 Optical Power Measurements Made Along Sensor During Construction.

From measurements made using a narrowband Rayleigh signal from the front end of the fibre to the input of the optical heterodyne coupler around 11.8dB of loss is registered along this optical return path. With this loss only 1.13mV output from the diode rectifier of the microwave section of the sensor is suggested by the models for a 110mW 100ns pulse when considering the anti-Stokes signal . This was confirmed by no signal being present on the oscilloscope when using 1533.17nm and looking over a frequency range of 10.7 to 11.5GHz. Previous work had incorporated a preamplifier for preamplification of the anti-Stokes backscattered signal. A preamplifier was developed and included in this piece of research as shown in figure 5.1.

5.1.2 Fibre Bragg Grating Characterisation

The fibre Bragg grating was characterised through the use of an optical spectrum analyser allowing for its transmission/reflectance window to be viewed. This was achieved by recording the power received over a range of wavelengths by the optical spectrum analyser after having passed from a known swept source, in this instance the tuneable laser, via the fibre Bragg grating itself.

The procedure was repeated by replacing the optical spectrum analyser with a 3MHz bandwidth optical detector. The results were then compared. Figure 3.13 shows a 3dB-cutoff window of around 0.11nm (13GHz) with a centre frequency at 1533.06nm corresponding well with what had been previously described [1]. Figure 3.14 shows a 3dB-cutoff window of 0.13nm (16GHz) with a centre frequency at 1533.09nm. This is slightly out of line with previous measurements. However, with the centre wavelength given previously at 1533.06nm it did seem reasonable to use this value as both sets of measurements taken suggested that the loss of any backscatter signal at this wavelength through the fibre Bragg grating would be minimal.

5.1.3 Preamplifier Consideration

With the reasons for preamplifier inclusion given in 5.1.1, a new 980/1550nm WDM was purchased to be used in its construction. The main aim with the preamplifier in this instance was to effectively nullify the loss seen along the optical return path of the sensor. As a result the cutback method of optical amplifier optimisation was employed

but only to give a gain approximately equal to the loss mentioned above. This was achieved with a gain factor of 14dB being the final value obtained for the preamplifier with a pump drive current level of 110mA.

In order to further improve any evaluation of the sensor the 38km of sensing fibre originally placed with the sensor had been reduced to 24km before the preamplifier was included. This is due to the noise anticipated on any backscatter signal beyond the range of 25km not being conducive to a favourable evaluation of the sensor as discussed in 4.2. Now together with the preamplifier in the sensor, evaluation of the entire system looked viable.

5.1.4 Microwave Receiver

Figure 3.15 shows a pink line that was generated using the Marconi 8210 Network Analyser test set. This line demonstrates the fluctuation in output power of the YIG synthesiser with frequency. The blue line represents measurements supplied by the manufacturing company. There is good correlation between the two sets of measurements suggesting that the YIG synthesiser is operating effectively.

The intermediate frequency stage gain of the microwave receiver was measured using the signal from a Marconi signal generator, which was set at –60dBm, being fed into the two microwave amplifiers within the microwave receiver. The output was then fed into an electronic spectrum analyser and the signal power was recorded, the difference between input and output signal being the effective gain of the two amplifiers. This was repeated across a frequency range around the intermediate frequency of 1GHz. Figure 3.17 shows the resulting graph of gain.

Finally the gain of the entire microwave section of the sensor excluding the diode rectifier was measured.

From figure 3.19 there does appear to be good correlation with the observed YIG synthesiser power output in figure 3.15 remembering the 1GHz offset between the two

figures. Anomalies in the correlation can be down to gain variation of the mixer characteristic itself. By using the coefficients derived from this information a far more accurate interpretation of any strain or heat on fibre can be made.

Figure 5.2 demonstrates the diode rectifer output voltage of the sensor as a function of preamplifer drive current after a period of 30 minutes. The upper trace is for a 100ns pulsewidth while the lower is that of a 40ns pulsewidth. In both instances, 100μW input power from the tunable laser was used. It was not necessary, as was not the case in previous work, to exceed the safe preamplifier pump drive current threshold value of 180mA as sufficient gain was produced with 110mA of drive current. It is noteworthy to see that both traces exhibit a linear nature to their evolution with drive current. This is suggestive of optical power within the sensor bearing a linear relationship with to diode output voltage. This, as will be discussed, helped form the way in which data from experimentation was analysed to give promising results.

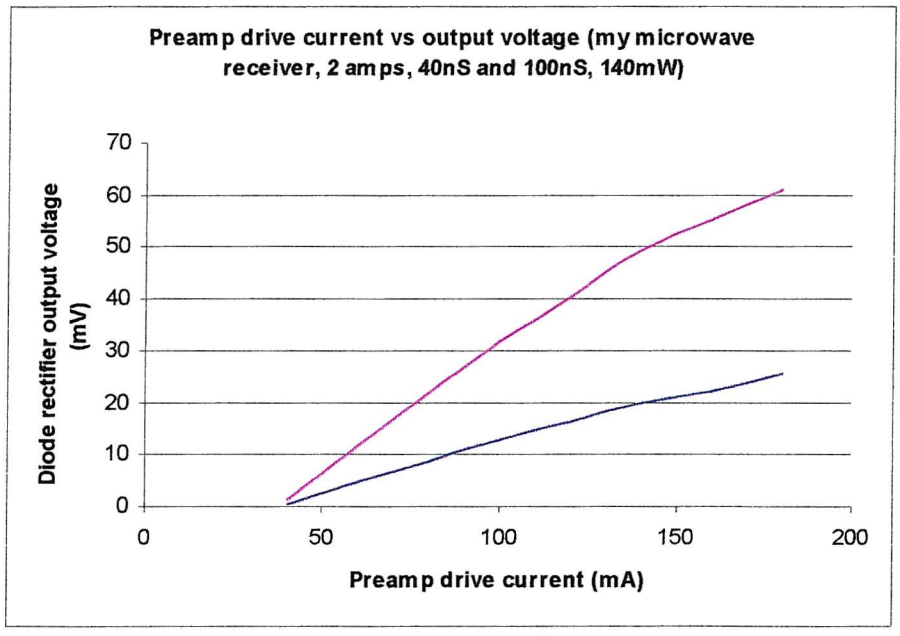

Figure 5.2 Diode Rectifier Output vs Preamplifier Drive Current.

Figure 3.16 shows a typical bandwidth of the microwave bandpass filter centred at 1GHz for inclusion in the microwave section of the receiver. The 3dB bandwidth shown here is around 51MHz and is tuneable through a variable capacitor incorporated within the design although during this thesis the bandwidth remained unchanged.

5.1.5 Rayleigh Considerations

The broadband Rayleigh trace generated at 1553.06nm for use in normalisation of anti-Stokes power measurements so as to enable intensity change at the heated and strains portions to be interpreted was collected for a 10m spatial resolution (100ns). Figure 5.3 and 5.4 show the Rayleigh trace with 4096 averages. This was obtained through the 5% tap of the 95/5 coupler before the sensing fibre as shown in figure 5.1. The peak power of the trace was found to agree with the modelled value of 49mV. This corresponds to an optical Rayleigh backscatter signal of 109nW. The SNR on the trace is around 25dB for 4096 averages. The logarithmic drop in signal power was observed as being 0.47dB/km along the fibre.

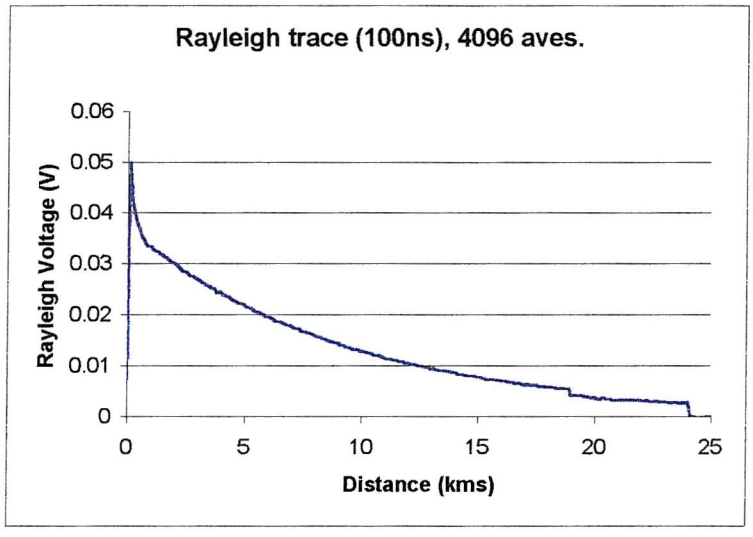

Figure 5.3 Rayleigh Trace Using a 100ns Pulsewidth.

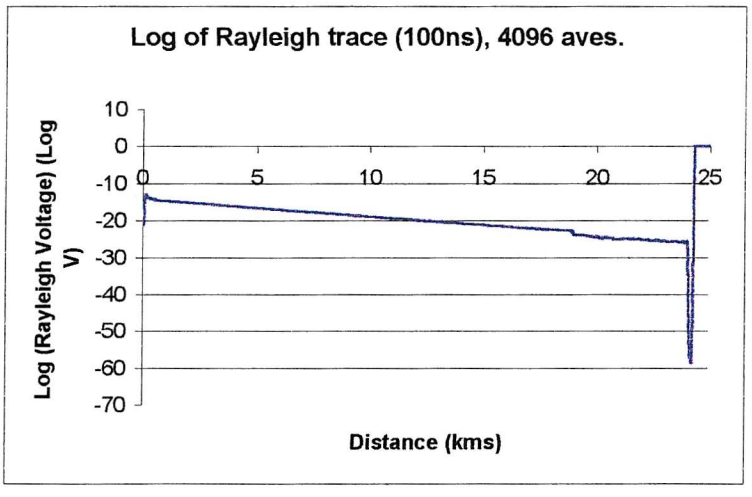

Figure 5.4 Logarithmic Trace of Rayleigh Trace Using a 100ns Pulsewidth.

An optical detector bandwidth-pulsewidth relationship, exploited in research prior to this, was made use of whereby

Optical detector bandwidth(Hz) x Pulsewidth (seconds) ≥ 0.3 {5.1}

This suggested that, using the optical detector whose characteristics are given in table 5.5, no Rayleigh trace generated with a pulsewidth less than 100ns could be correctly resolved for the purposes of accurate anti-Stokes normalisation.

TA10 Optical Detector (InGaAs)
Feedback Resistance: 100MΩ
Sensitivity: 10mV/nA into 50Ω
Detection Bandwidth: dc-3MHz
Aperture Diameter 0.3mm
GAP: 300
NSD: 15fA/√Hz
Corner Frequency: 110kHz

Table 5.5 Characteristics of Optical Detector Used in Obtaining 10m Spatially Resolved Rayleigh Trace.

Figure 5.6 shows the Rayleigh trace obtained using the optical detector characterised above with a 100ns pulsewidth at the region of fibre to be examined.

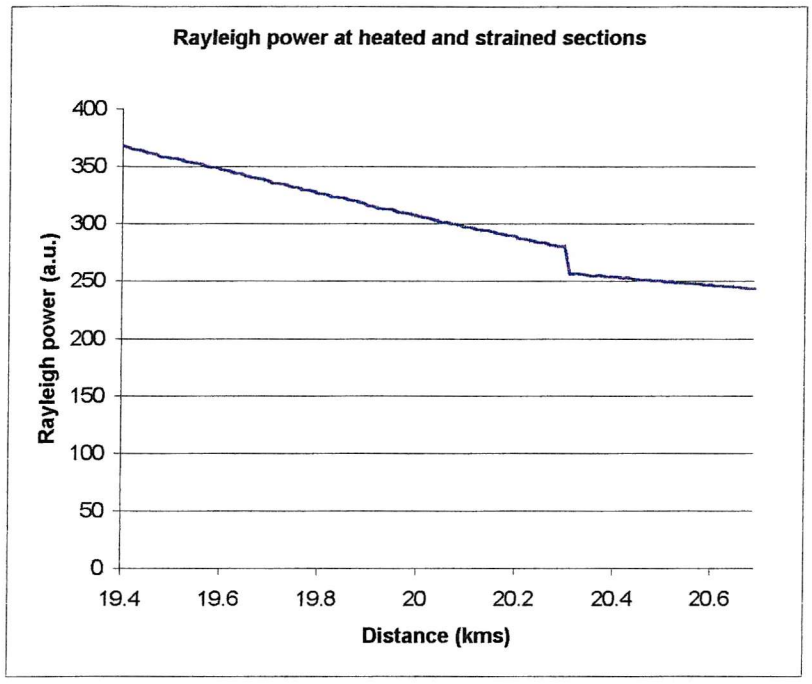

Figure 5.6 Rayleigh Trace Used for Normalisation of Anti-Stokes Power (100nS pulsewidth).

With the relationship in {5.1} limiting the generation of Rayleigh backscatter traces using pulsewidths less than 100ns this meant that another approach had to be investigated in order to generate a 40ns Rayleigh backscatter trace for normalisation of the 4m (40ns) anti-Stokes backscatter trace.

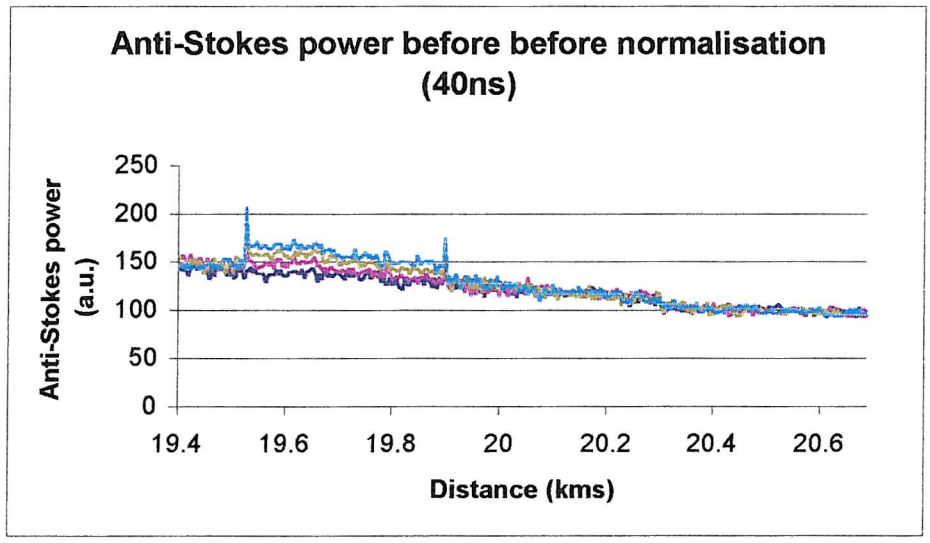

Figure 5.7 Anti-Stokes Power Before Normalisation (40ns).

Taking the anti-Stokes intensity measurements shown in figure 5.7 which were generated through the use of a computer program developed in previous research, the heated and strained sections of this graph were effectively removed leaving only the unheated and unstrained sections of fibre in the region being examined. These unheated and unstrained sections were then used in a curve fitting algorithm in order to generate the missing sections between them caused by the removal of the heated and strained sections. The generated curve was then regarded as an effective 4m (40ns) Rayleigh curve for the normalisation of the 4m (40ns) anti-Stokes backscatter trace and is shown in figure 5.8.

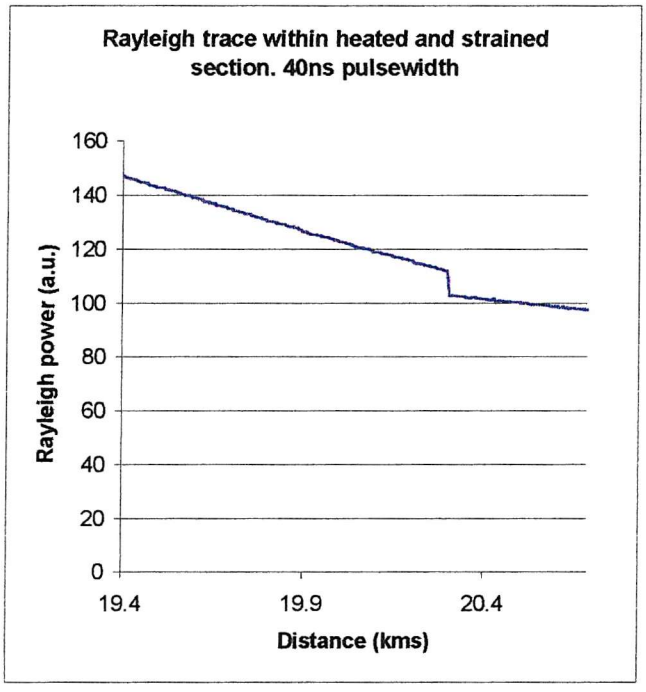

Figure 5.8 Rayleigh Trace Used for Normalisation of Anti-Stokes Power (40ns pulsewidth).

As will be seen further on in this chapter, this process appears valid for the generation of a Rayleigh curve used in anti-Stokes trace normalising although a lot of data processing was involved to get the curve as shown.

5.1.6 Noise Considerations

Although not comprehensive by any means, the following demonstrates how noise can be estimated in order to gain an insight into the performance of the sensor. This then allows for subsequent experimentation with the sensor should the results from these noise floor measurements prove positive.

The electronic spectrum analyser was used as the receiver in this analysis as the hybrid microwave receiver that I have constructed does not easily lend itself to measurement of noise and noise floors.

5.1.6.1 Electronic Spectrum Analyser

The noise floor of the electronic spectrum analyser is quoted [2] as possessing the following noise floors:

> ≤ -110dBm within the span of 6-12GHz for a 1kHz resolution bandwidth (RBW) and 30Hz video bandwidth (VBW).

For a 5MHz RBW this value scales to ≤-73dBm.

This was confirmed with the ESA noise floor measured at –75dBm for a 5MHz RBW.

This was achieved through 40μV being measured as the noise floor using a linear voltage scale and no input signal with the input port terminated with a 50Ω load. This was conducted over a span of 10.6 to 11.4 GHz in 50MHz steps.

The value of –75dBm was verified by –82dBm being observed for a 1MHz RBW and a –92dBm noise floor being seen for a 100kHz RBW.

5.1.6.2 Lightwave Detector

The lightwave detector was connected to the input of the electronic spectrum analyser using the same span of 10.6-11.4GHz in 50MHz steps and with a 5MHz RBW in order to see the Brillouin anti-Stokes signal should it be present. With the sensing system operating the noise floor remained at –75dBm and no Brillouin signal was seen. This concurs with previous modelling carried out which suggested that the lightwave detector, with an NEP of 18pW/√Hz, has a noise power of –105dBm (electrically) into a 5MHz RBW. The total noise power modelled suggested (see above) –161dBm for a

1Hz RBW or –94dBm for a 5MHz RBW, both these values not being viewable with the electronic spectrum analyser noise floor at –75dBm.

As regards viewing the Brillouin signal, it should be noted that only (5/35MHz) of its linewidth can be viewed using this direct detection method due to the RBW being $1/7^{th}$ the width of the Brillouin linewidth. This effectively reduces the Brillouin signal strength to $1/7^{th}$ of its actual power assuming a uniform rectangular linewidth and less than $1/7^{th}$ for any other linewidth shape.

5.1.6.3 Microwave Receiver

Finally the new microwave receiver was placed in between the lightwave detector and the electronic spectrum analyser. With previous settings of RBW=5MHz and a span of 10.6-11.4GHz in 50MHz steps once again being observed the noise floor remained constant at –75dBm with the entire sensor system operating. This suggests that the noise power of the electronic spectrum analyser, namely –75dBm in a 5MHz RBW, is greater than the total noise power of the new sensor. Once again the Brillouin anti-Stokes signal was not observed.

5.1.6.4 Comparison With Modelled Theory

The signal that had been launched down 38km of sensing fibre for these noise floor measurements was 110mW in strength and 100ns in duration. No preamplification had been used during these measurements. From modelled theory, the predicted Rayleigh optical backscatter at the front end of the sensing fibre was of the order of 86nW suggesting a Brillouin anti-Stokes backscatter power of 1.4nW translating to an electrical power of –85.8dBm output from the lightwave detector. The noise power output of the lightwave detector has been modelled as being -94dBm into a 5MHz RBW suggesting an electrical SNR of +8.2dB at the microwave receiver. However due to the noise floor of the electronic spectrum analyser being above both these values at -75dBm this was not confirmed. Omitting this fact for one moment, the voltage output from the diode rectifier would only be of the order of 1mV and so not of much use for data collection. More importantly the noise figure of the new microwave sensor would

cause the SNR at the diode rectifier output to turn negative to the order of –3.5dB electrically.

With this in mind and the fact described in 4.2 that for any intelligible evaluation of the new sensor the fibre sensing length needed to be below 25km the system was changed in order to incorporate a preamplifier (see 5.1.3) of gain merely sufficient to overcome loss along the optical path with the sensing length being reduced to below 25km.

5.1.6.5 Analysis Of Sensor With Preamplification Of 14dB

As highlighted in 5.1.6.4 the preamplification factor of 14dB was merely intended to nullify the loss observed through the optical path. This would then, according to modelled theory, allow the Brillouin anti-Stokes signal to be observed. With the preamplifier in place the sensor was operated as per 5.1.6.3 but with the electronic spectrum analyser replaced with a 200MHz digital oscilloscope. Once again the predicted Rayleigh and Brillouin backscatter powers were respectively 86nW and 1.4nW at the front end of the sensing fibre. With the optical preamplification of 14dB this gave a SNR at the microwave receiver of +22.2dB with an electrical output power from the lightwave detector of –71dBm. Moreover the SNR at the diode rectifier would be of the order of +10.5dB with a rectified voltage output of around 28mV.

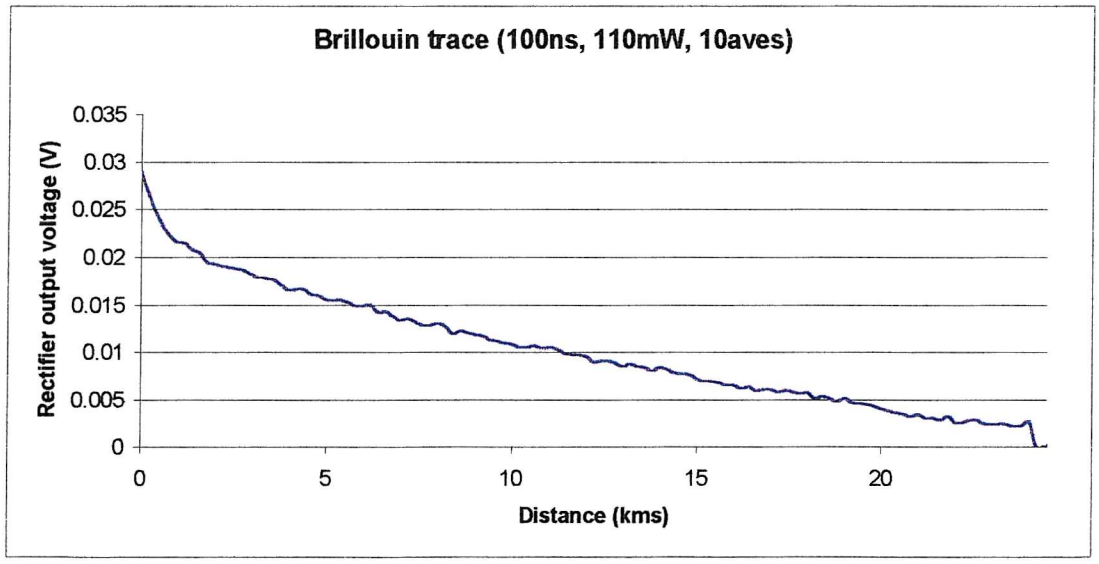

Figure 5.9 Diode Rectifier Output Voltage for a 25km Sensing Length.

Figure 5.9 shows the resulting trace obtained from the sensor for a 110mW, 100ns pulse and 10 averages. As can be seen there is good correlation between the predicted diode rectifier output voltage and the result obtained, both being of the order of 28mV. As regards the SNR on the trace, figure 5.9 demonstrates a front end value of 15dB for just 10 averages. This reduces to 10dB before averaging once again suggesting very good correlation with modelled theory.

5.2 Simultaneous Temperature And Strain Sensing Over 20km

As previously stated in 5.1.5 Rayleigh traces were generated using two different methods due to optical bandwidth restrictions for the purposes of normalising the anti-Stokes data. The time for collecting the anti-Stokes data was of the order of 25 hours as the frequency range of Brillouin spectra covered was 500MHz in 5MHz steps with 65536 averages being taken at each frequency. The reason for such a wide frequency range was to assure that no data would be missed for the evaluation of the new sensor.

With the sensor constructed as appropriate to the requirements of evaluation a distance of 20km sensing was decided upon as a good point to place the fibres to be strained and heated. This was based on previous analysis showing that noise as a percentage of signal power was conducive to a good evaluation of the sensor for distances less than 25km. The following work in this chapter demonstrates the capability of the sensor in terms of its temperature and strain resolution over the sensing length chosen.

The sensing fibre, in order to make the 20km length desired, was constructed using the telecommunication standard single mode fibre lengths shown in figure 5.10.

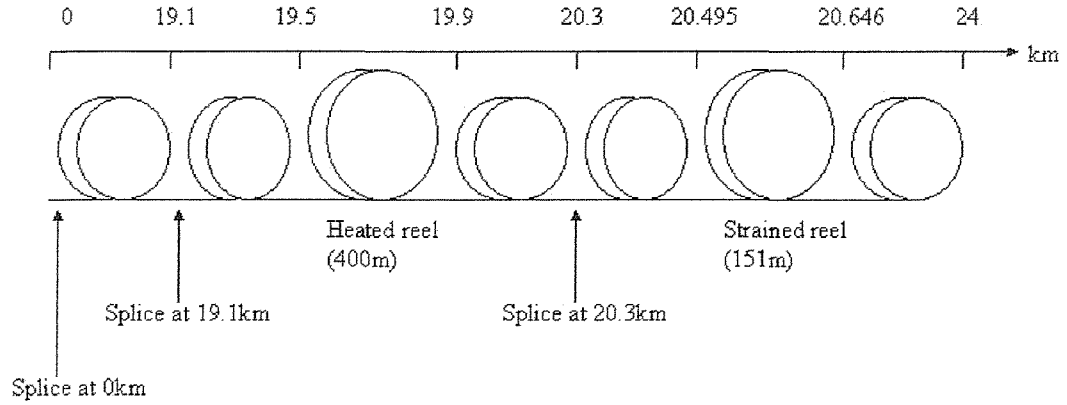

Figure 5.10 Fibre Sensing Layout.

Splices in the sensing fibre were kept to a minimum and the heated and strained regions were surrounded on both sides by similar fibre with no immediate splicing in their vicinity. This ensured accurate measurement of any change in fibre property in the heated and strained regions without the need to include splice effects.
Both temperature and strain measurements were conducted simultaneously over the distances designated in figure 5.10.

Two sets of data were taken, one for a 100ns pulsewidth of 140mW peak power and another of 40ns pulsewidth of the same peak power. The pulses launched are shown in 5.11 and 5.12.

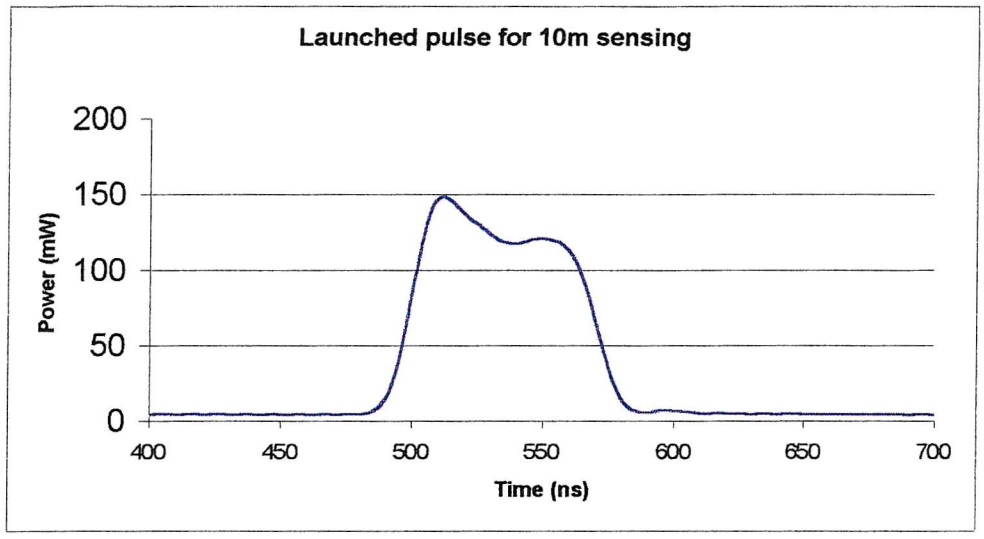

Figure 5.11 100ns Pulse Launched Down the Sensing Fibre.

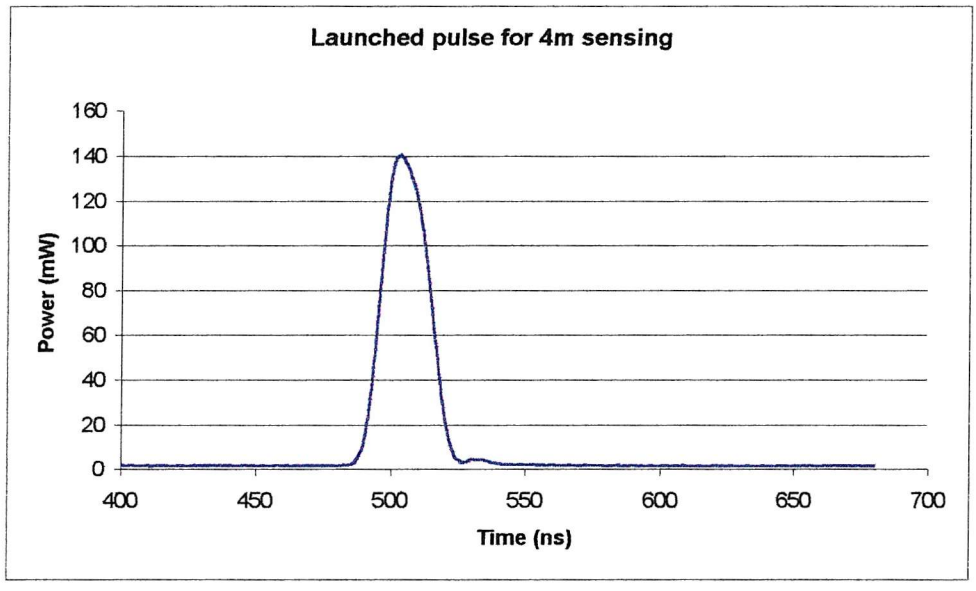

Figure 5.12 40ns Pulse Launched Down the Sensing Fibre.

Both of these data with spatial resolutions of 10m and 4m respectively were not obtainable using the electronic spectrum analyser used in research prior to this. 65536 averages were taken during data collection with the 200MHz oscilloscope being used to zoom in on the regions of interest, namely those of the strained fibre and the heated fibre.

After both spectra sets at 10m and at 4m spatial resolution had been obtained, the frequency shift and power of the Brillouin backscatter was determined at each spatially resolved point along the fibre within the region where strain and heat were being applied.

resolved point along the fibre within the region where strain and heat were being applied.

Using a curve fitting algorithm developed in previous research, a Lorentzian curve was fitted to each spectrum along the fibre at intervals determined by the pulsewidth. This was appropriate since the Brillouin linewidth shape has previously been demonstrated to be of Lorentzian form. By fitting the Lorentzian function, the area or total power under this curve is proportional to the peak power multiplied by its linewidth at that point. The Levenberg-Marquardt nonlinear least squares algorithm was used to determine this area [3] [4]. The advantage of the Levenberg-Marquardt algorithm is that the correct area will be determined even if some of the function lies outside the frequency of the scan, provided there is sufficient data for a good fit. This algorithm can also provide frequency shift information to a higher resolution than the frequency step used in the scan.

5.3 Simultaneous Temperature And Straining Results Obtained From The New Sensor Over 20km

Measurements were taken for 20km sensing length as shown in figure 5.10 according to the following.

The ambient environment was consistently measured as 22°C using a digital thermometer and was stable through the use of an air-conditioning unit and circulating fan. With this in mind oven temperatures were set at the following values: Ambient (22°C), 42°C, 62°C and 82°C. The following strain measurements were recorded simultaneously with those in the heated region: No strain (0με), 19.5cm extension (1290με), 24.4cm extension (1615με), 29.3cm extension (1935με).
65536 averages were used in data collection which involved collecting data over 11000-11500MHz in 5MHz steps. With the sensing fibre set with a particular temperature and strain the time taken for such a run was typically 25 hours.

Figures 5.6 and 5.13 show respectively the Rayleigh trace used for normalisation of the anti-Stokes backscatter powers and the anti-Stokes backscatter powers obtained at the temperatures and strains measured.

Figures 5.14 and 5.15 show respectively the Brillouin frequency shift and percentage change in backscatter intensity for the 10m (100ns) spatial resolution sensor. The sharp spikes in figures 5.13 and 5.15 are attributed to discontinuities in the temperature at the heated section edges.

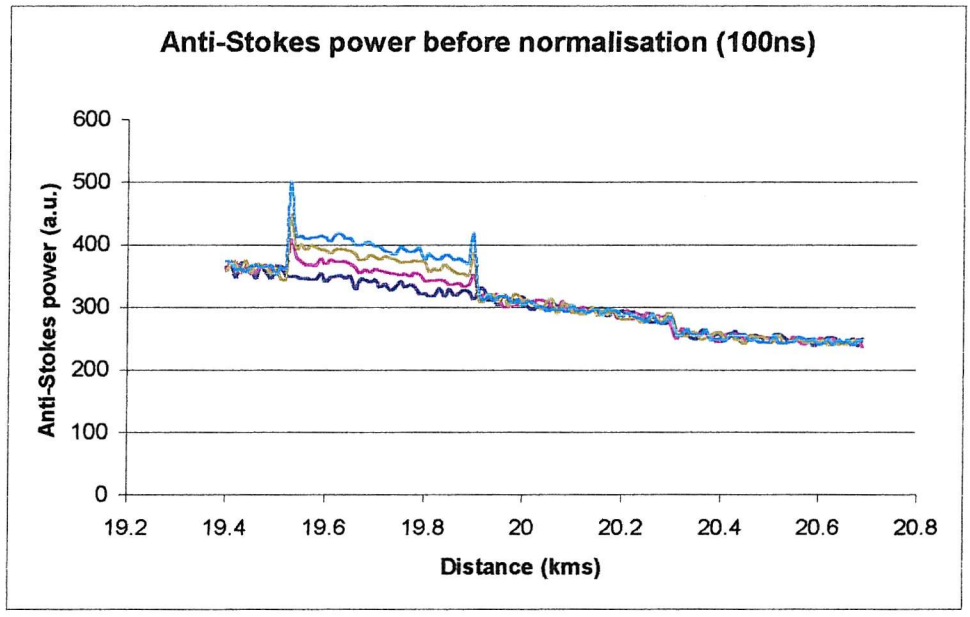

Figure 5.13 Anti-Stokes Power Before Normalisation (100ns).

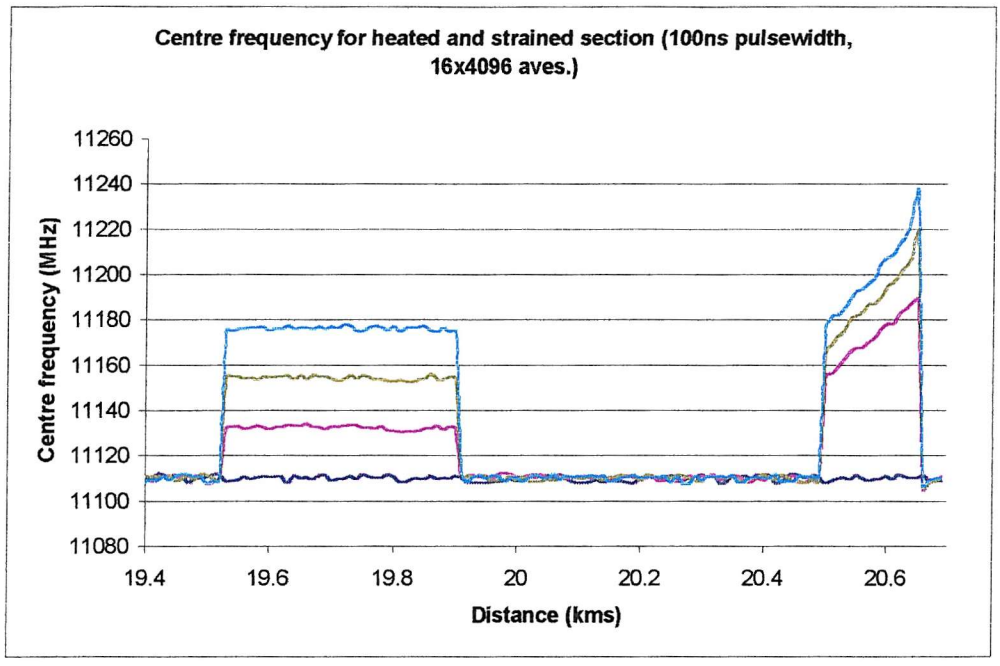

Figure 5.14 Frequency Shift of Anti-Stokes Centre Frequency With Various Temperatures and Strains (100ns pulsewidth).

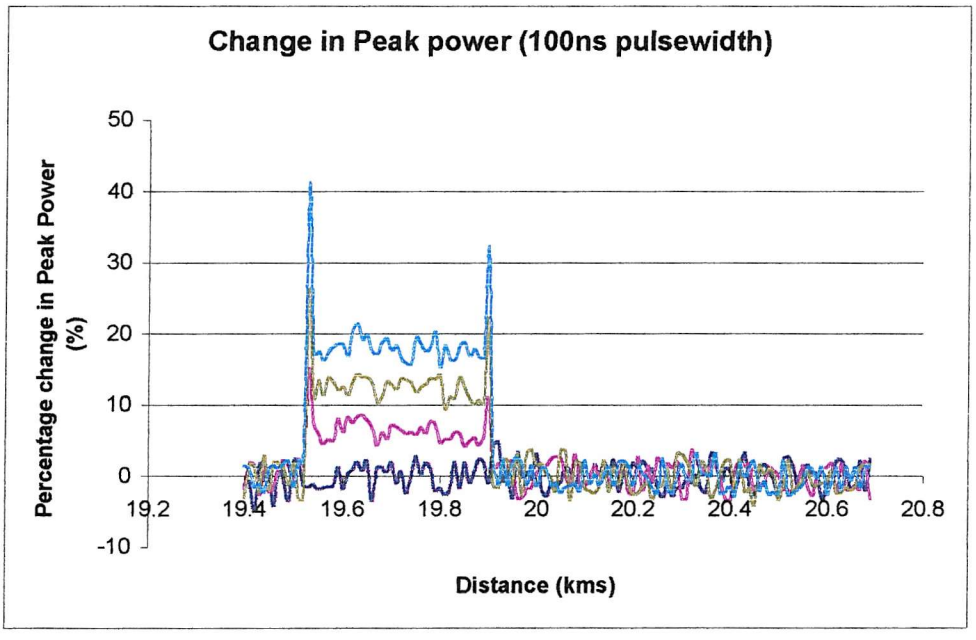

Figure 5.15 Change in Anti-Stokes Power With Various Temperatures and Strains (100ns pulsewidth).

5.3.2 4m Spatial Resolution

Figures 5.8 and 5.7 show respectively the Rayleigh trace used for normalisation of the anti-Stokes backscatter powers and the anti-Stokes backscatter powers obtained at the temperatures and strains measured.

Figures 5.16 and 5.17 show respectively the Brillouin frequency shift and percentage change in backscatter intensity for the 4m (40ns) spatial resolution sensor. The sharp spikes in figures 5.7 and 5.17 are attributed to discontinuities in the temperature at the heated section edges.

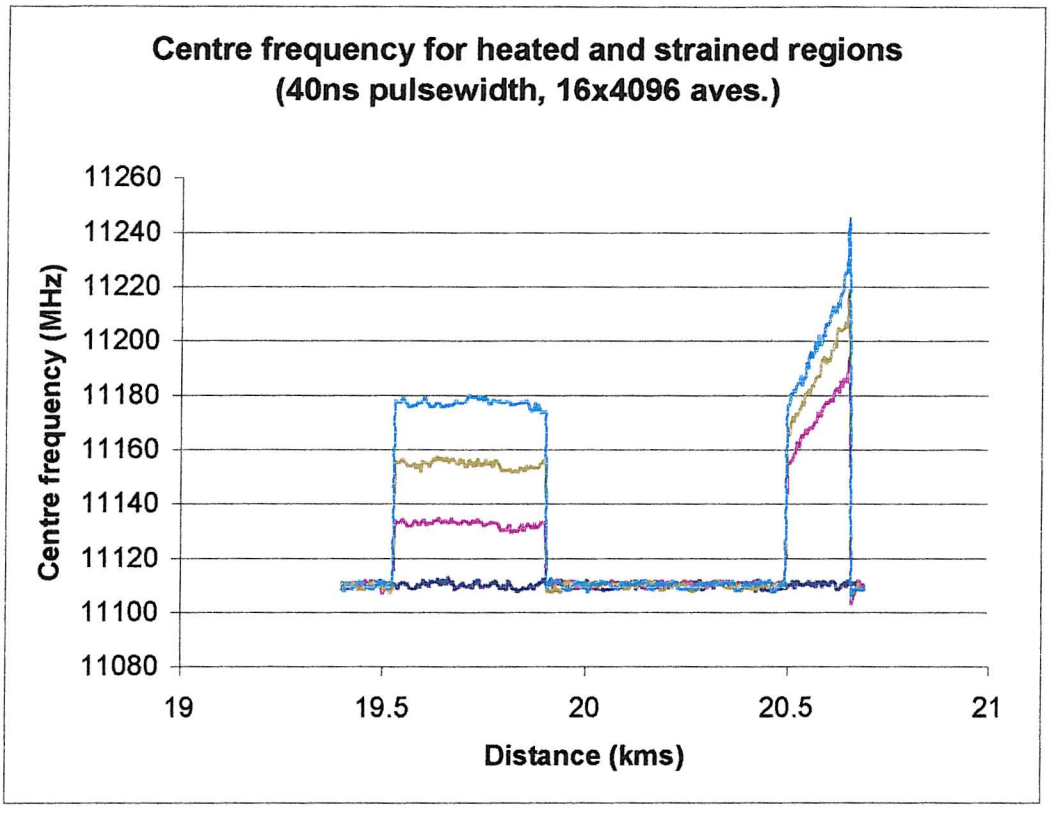

Figure 5.16 Frequency Shift of Anti-Stokes Centre Frequency With Various Temperatures and Strains (40ns pulsewidth).

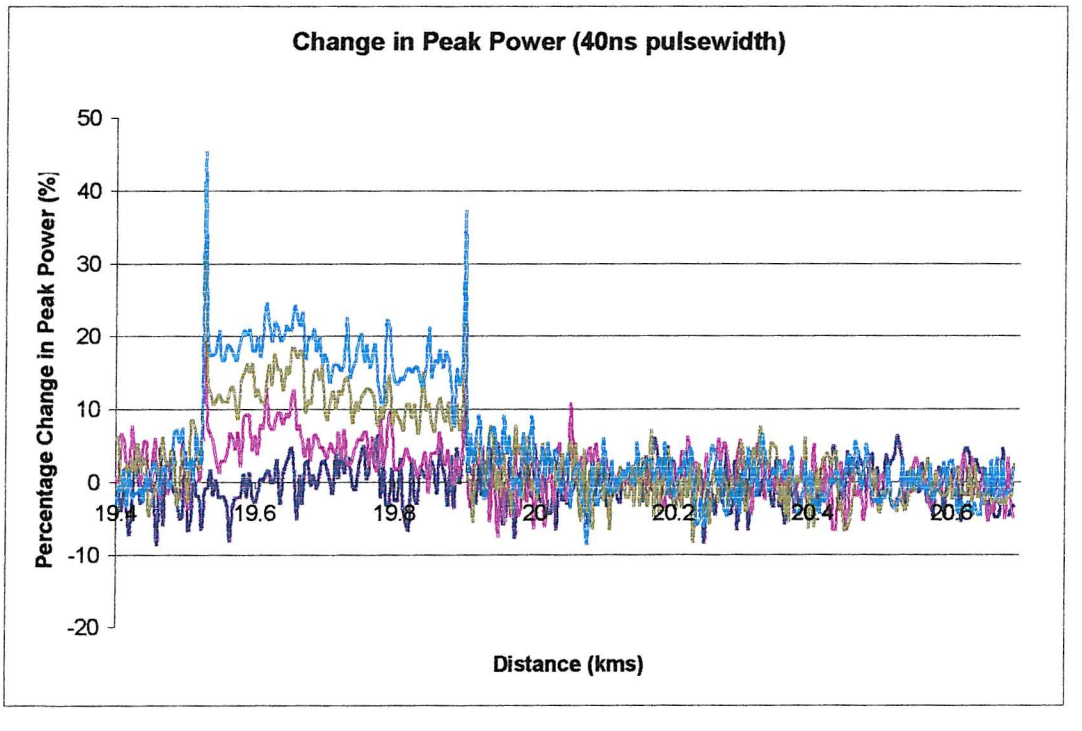

Figure 5.17 Change in Anti-Stokes Power With Various Temperatures and Strains (40ns pulsewidth).

5.4 Temperature Calibration

The heated portion of the sensing fibre consisted of placing 400m of standard telecommunications fibre into a temperature-controlled oven. With the fibre inside being insulated from the ambient environment the oven, during each heated run, was allowed to temperature stabilise over 3-4hours in order to ensure that the fibre was not subject to any hotspots. Temperature stability at the required temperature was conducted through a stirring fan within the oven effectively circulating the air to ensure one temperature inside the oven.

The ambient environment was consistently measured as 22°C using a digital thermometer and was stable through the use of an air-conditioning unit and circulating fan. With this in mind oven temperatures were set at the following values: Ambient (22°C), 42°C, 62°C and 82°C.

Using 65536 averages, results were obtained allowing for the following temperature calibration graphs to be generated.

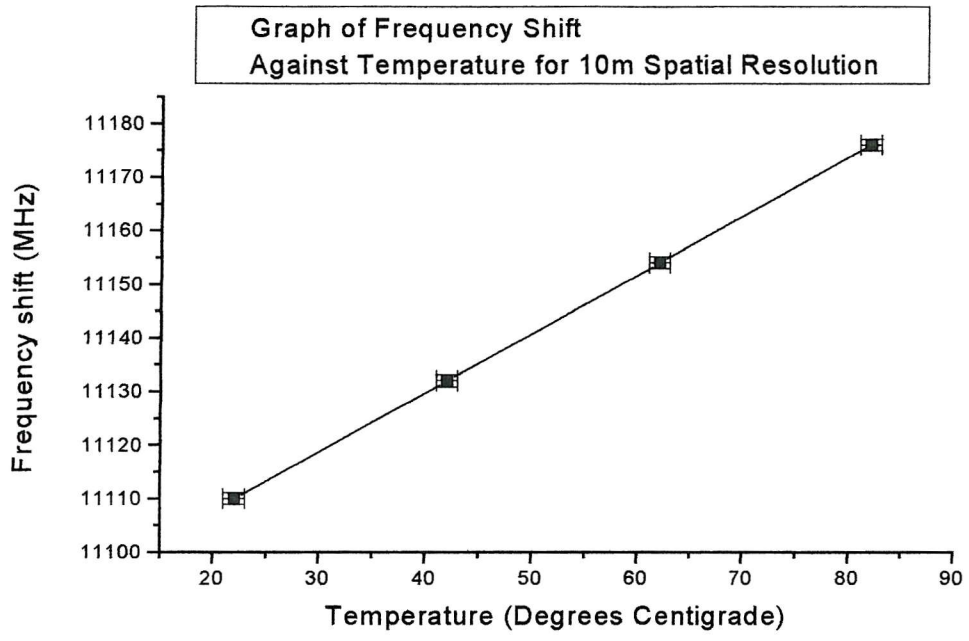

Figure 5.18 Anti-Stokes Centre Frequency Shift vs Temperature (100ns).

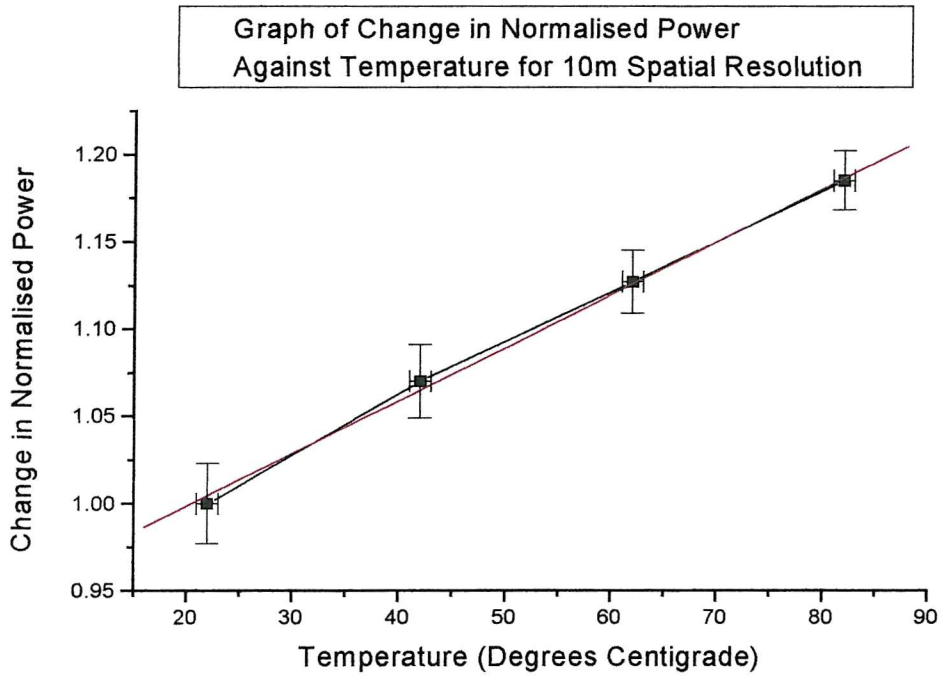

Figure 5.19 Change in Anti-Stokes Normalised Power vs Temperature (100ns)

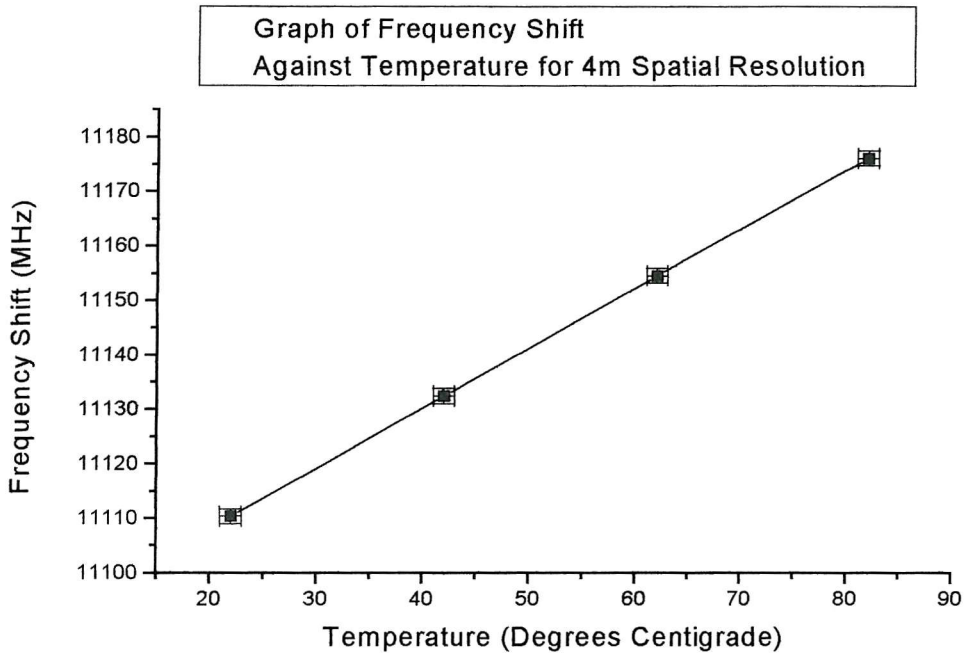

Figure 5.20 Anti-Stokes Centre Frequency Shift vs Temperature (40ns).

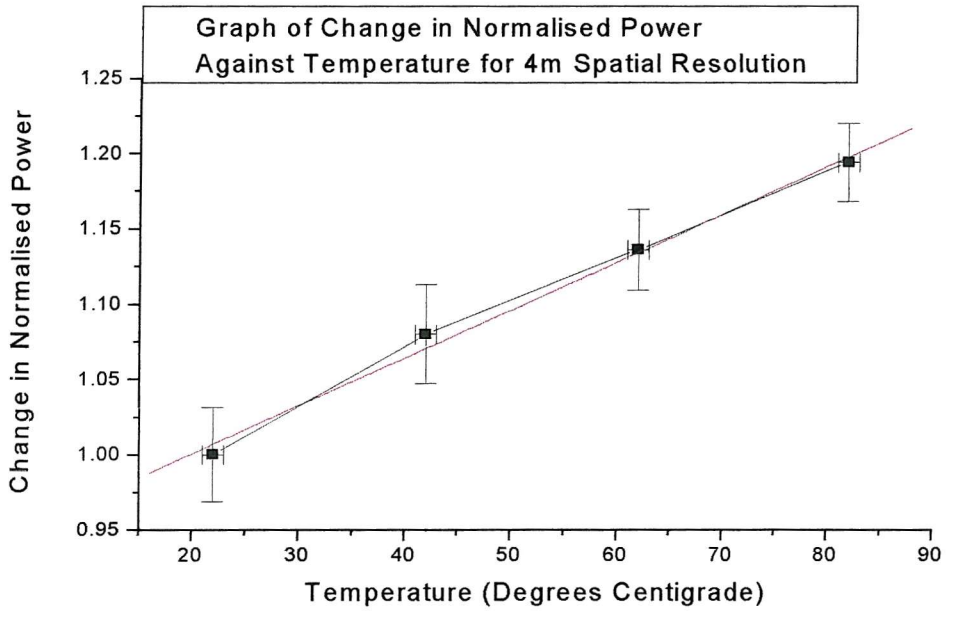

Figure 5.21 Change in Anti-Stokes Normalised Power vs Temperature (40ns).

5.5 Strain Calibration

The strained portion of the sensing fibre consisted of placing 151m of standard telecommunications fibre onto a rig as demonstrated in figure 5.22. Although 11 pairs of pulleys were available only 10 were used in this instance.

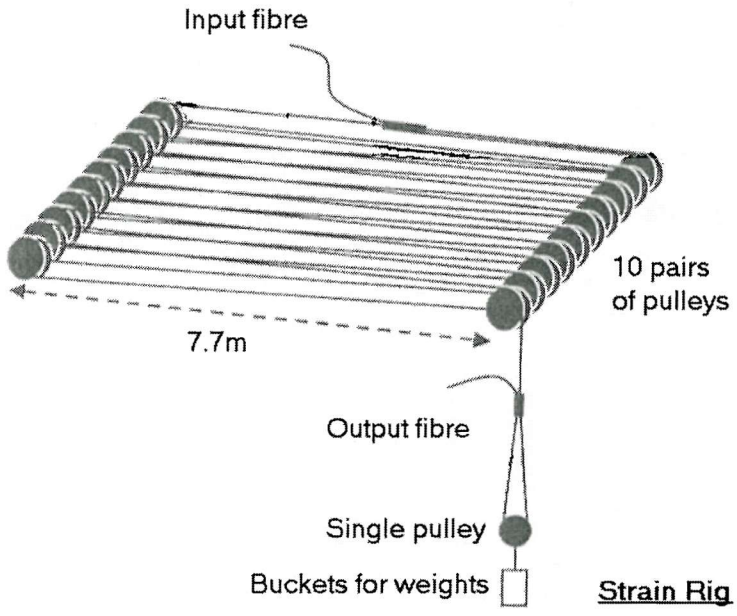

Figure 5.22 Strain Rig Layout for Strain Measurements.

With the fibre in place, weights were placed in the bucket causing it to descend. From a known control position of the bucket the extension of the fibre was measured and recorded in order to calculate the strain on the fibre on the rig. This strained fibre was also allowed to stabilise over the same period of time granted to the heated fibre and measurements taken of the strained region were then carried out simultaneously with those of the heated region.

The following strain measurements were recorded simultaneously with those in the heated region using 65536 averages:

No strain (0με), 19.5cm extension (1290με), 24.4cm extension (1615με), 29.3cm extension (1935με).

This allowed the following strain calibration graphs to be generated. It should be noted that figures 5.14 and 5.16 show the differential nature of the strain across the strain rig in figure 5.22. The frequency shifts of the strained section in these figures correspond well to previous results [5] also showing this phenomenon to occur. In this instance the anti-Stokes frequency shift within the strained section has been found by determining the average value of frequency shift within this section. This value has then been used to generate figures 5.23 and 5.25.

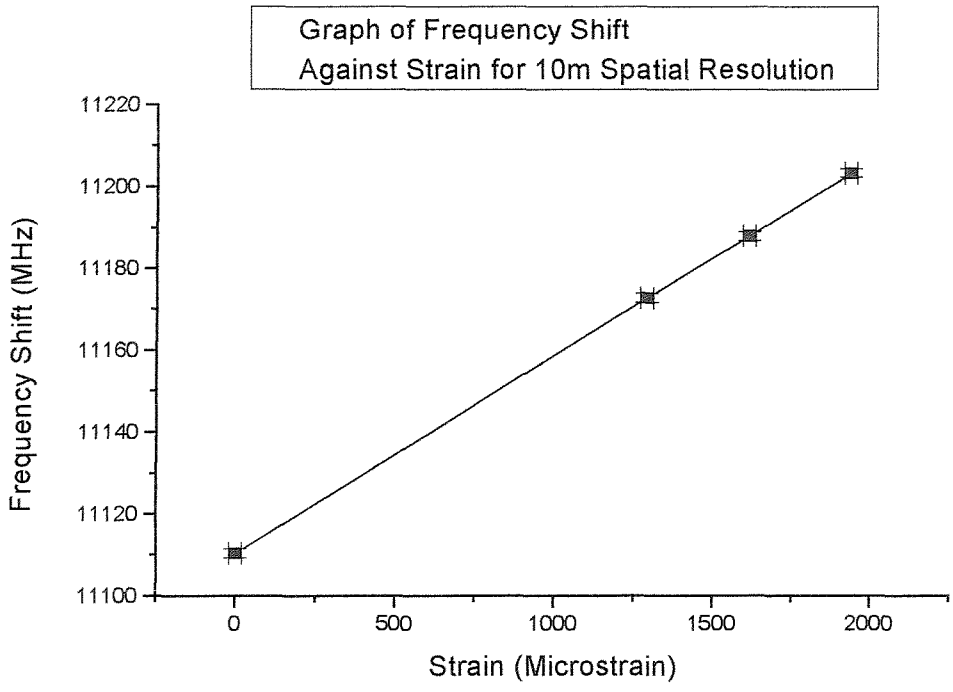

Figure 5.23 Anti-Stokes Centre Frequency Shift vs Strain (100ns).

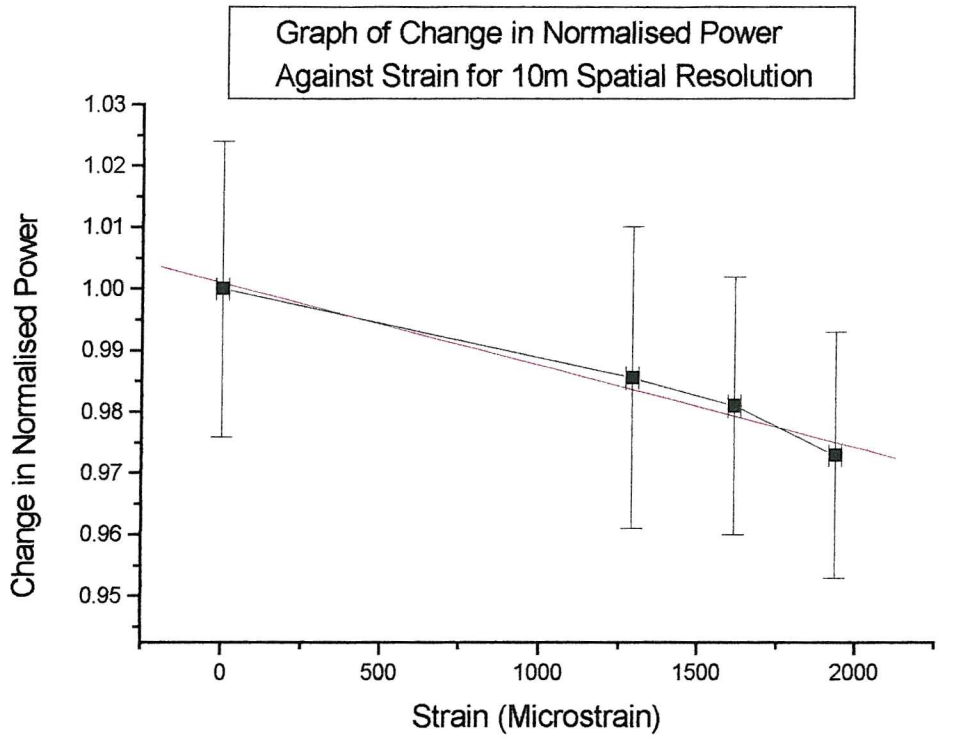

Figure 5.24 Change in Anti-Stokes Normalised Power vs Strain (100ns).

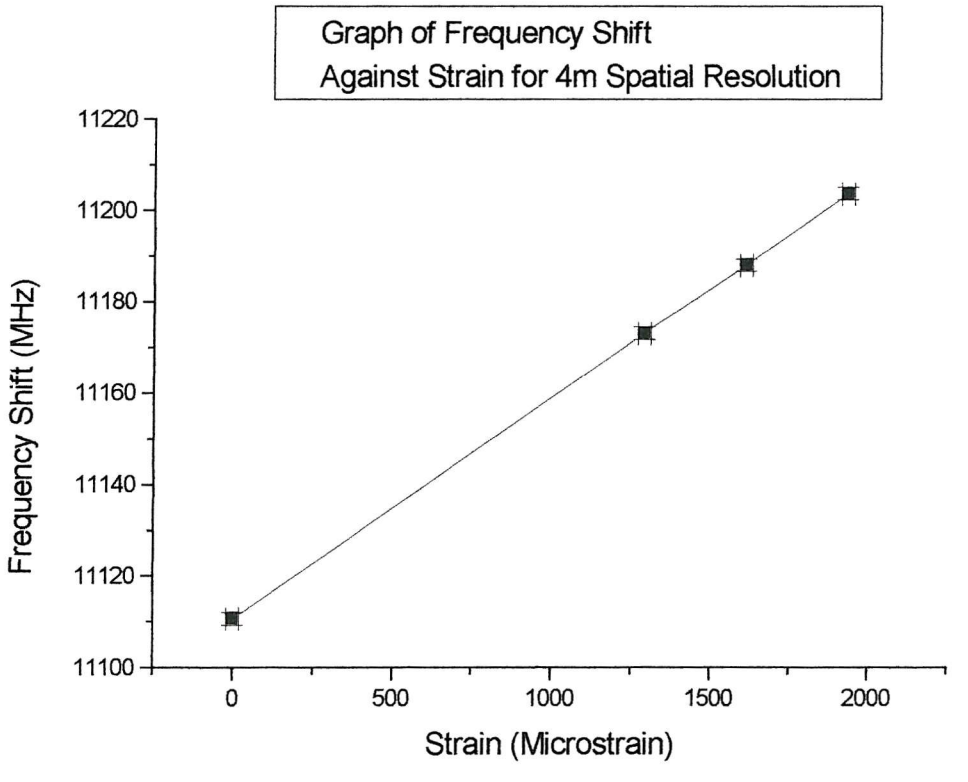

Figure 5.25 Anti-Stokes Centre Frequency Shift vs Strain (40ns).

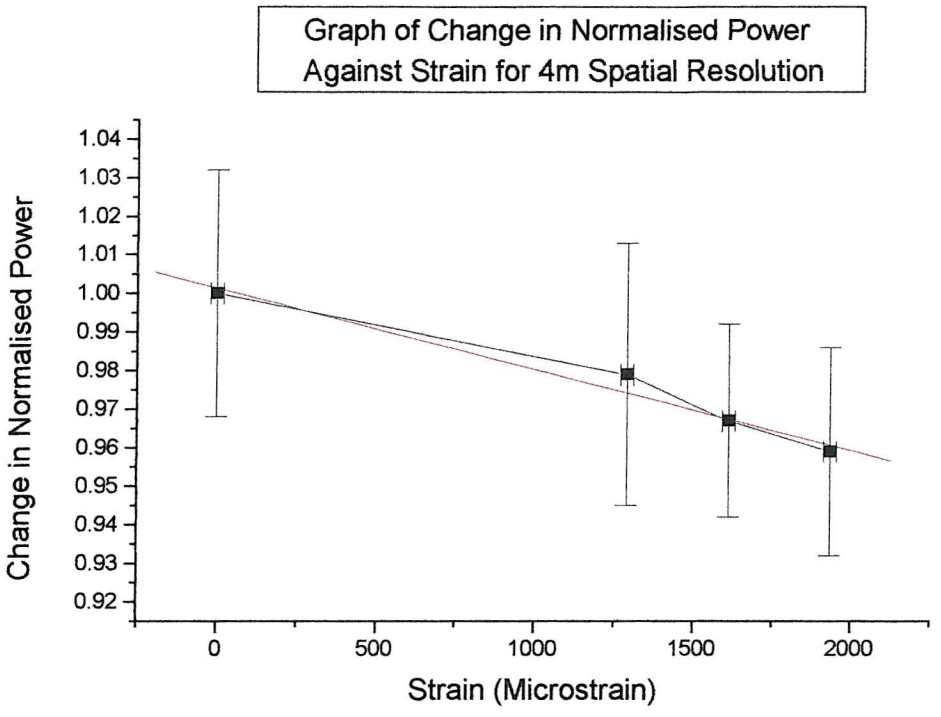

Figure 5.26 Change in Anti-Stokes Normalised Power vs Strain (40ns).

5.6 Coefficients Of Frequency Shift & Intensity Change With Temperature And Strain

The data used to construct figures 5.18, 5.19, 5.20, 5.21, 5.23, 5.24, 5.25 and 5.26 was also evaluated to give RMS errors for each specified temperature and strain point. The RMS errors are included on the figures and pertain to human measurement error in the x-axis together with the associated sensor error in the y-axis. These RMS errors have been used, according to {3.9}, to obtain the information that the 10m spatial resolution sensor has a temperature resolution of <7.3K together with a strain resolution of <190με while the 4m spatial resolution sensor has a temperature resolution of <9.5K together with a strain resolution of <240με. In both instances the overwhelming error in temperature and strain resolution is caused by the error in intensity readings which constitutes a value of 90% of the total resolution error for the 10m spatial resolution sensor and 98% of the total resolution error for the 4m spatial resolution sensor.

Linear regression was also employed in order to generate a line of best fit for these figures and the results together with their associated errors are given below.

5.6.1 10m Spatial Resolution

$C_{vb\varepsilon}$=coefficient for change of Brillouin frequency shift with strain=(0.048±1.4E-4)MHz/με

C_{vbT} =coefficient for change of Brillouin frequency shift with temperature=(1.1±0.1)MHz/K

$C_{Pb\varepsilon}$ =coefficient for change of Brillouin backscatter intensity with strain= (-1.3E-3±2E-4)%/με

C_{PbT} =coefficient for change of Brillouin backscatter intensity with temperature=(0.30±1E-2)%/K

{5.2}

5.6.2 4m Spatial Resolution

$C_{vb\varepsilon}$=coefficient for change of Brillouin frequency shift with strain=(0.048±2.2E-4)MHz/με

C_{vbT} =coefficient for change of Brillouin frequency shift with temperature=(1.11±0.1)MHz/K

$C_{Pb\varepsilon}$ =coefficient for change of Brillouin backscatter intensity with strain= (-2.1E-3±2.3E-4)%/με

C_{PbT} =coefficient for change of Brillouin backscatter intensity with temperature=(0.32±1.8E-2)%/K

{5.3}

5.7 Linewidth

Figure 5.27 reveals the linewidth within the control (not heated and not strained) section of the fibre for a 100ns pulsewidth.

The linewidth remains virtually unchanged along the unheated portion of the fibre length of fibre examined with a mean value of 89.67MHz and a RMS error of just 0.5MHz as shown in figure 5.28. However, the linewidth is seen to decrease by a mean value of 4.2MHz to 85.47MHz over the heated portion of the fibre for a 60°C rise above ambient. The RMS error is however fairly constant at 0.54MHz.

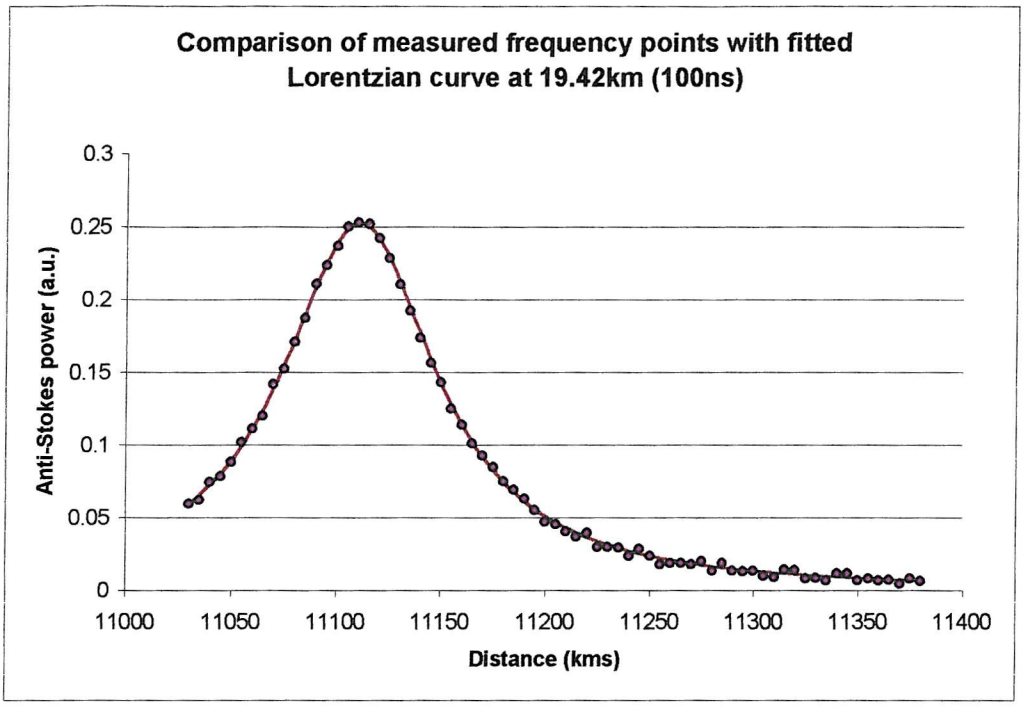

Figure 5.27 Anti-Stokes Linewidth Within Unheated and Unstrained Region Together With Associated Lorentzian Line-Fit (100ns).

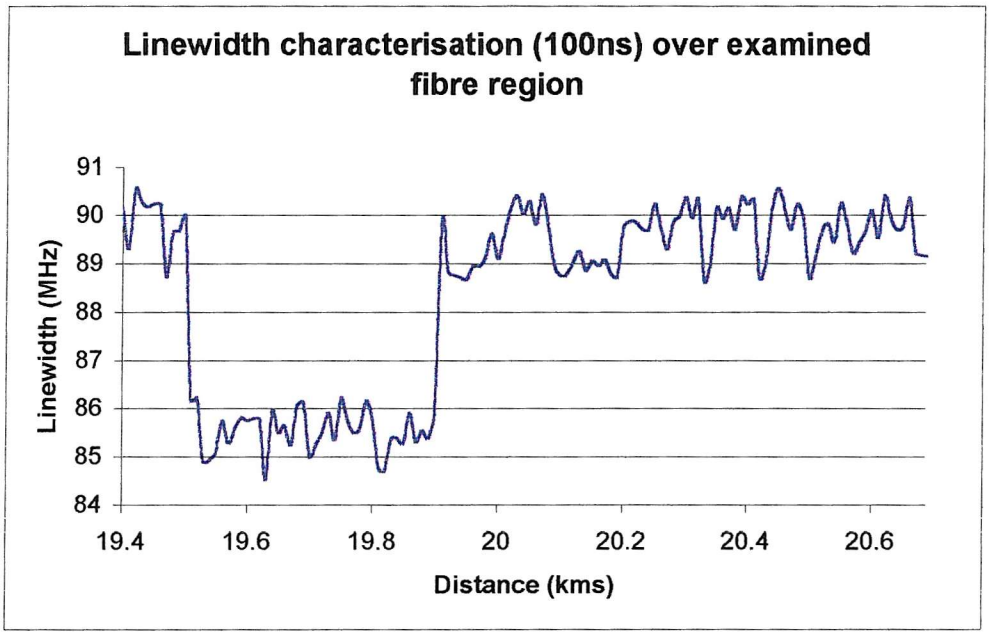

Figure 5.28 Change in Anti-Stokes Linewidth Along The Fibre Being Sensed (100ns).

The linewidths for three distances along the fibre using a 40ns pulsewidth are shown in figures 5.29 to 5.31. Figure 5.29 shows the linewidth at a distance in the control section (unheated and unstrained section) of the fibre. Figure 5.30 shows the linewidth at a distance in the heated region of the fibre with figure 5.31 demonstrating the linewidth

within the strained region of the fibre. Once again the unheated portion of the fibre being examined appears to show a linewidth virtually unchanged along the length of 1.29km, the mean value being 90.27MHz with an RMS error of 0.71MHz as shown in figure 5.32. Within the heated portion of the fibre, the linewidth changes once again in a decreasing fashion similar to the measurements made with a 100ns pulsewidth. However this time the decrease is just 3.5MHz to 86.77MHz for a 60°C rise in temperature above ambient with an RMS error of 0.77MHz.

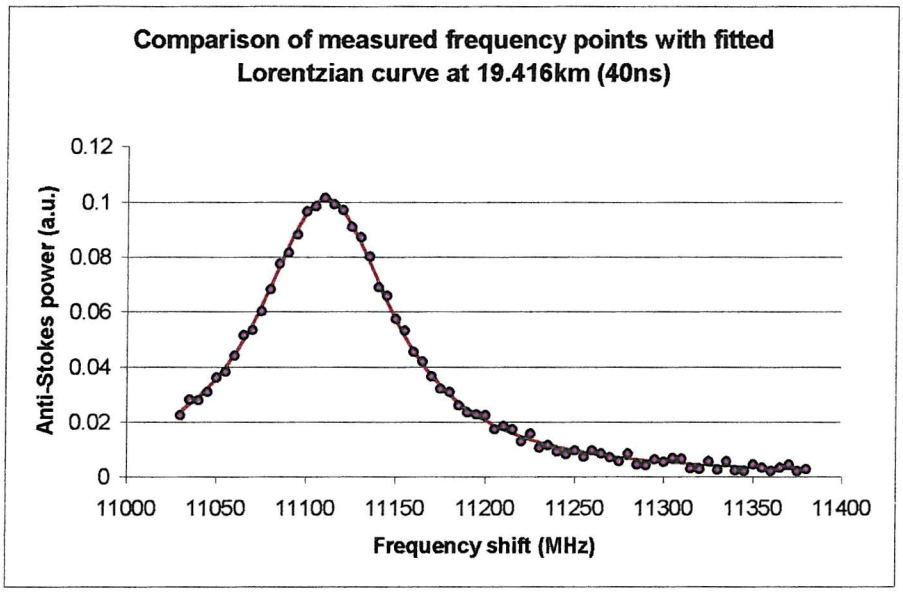

Figure 5.29 Anti-Stokes Linewidth Within Unheated and Unstrained Region Together With Associated Lorentzian Line-Fit (40ns).

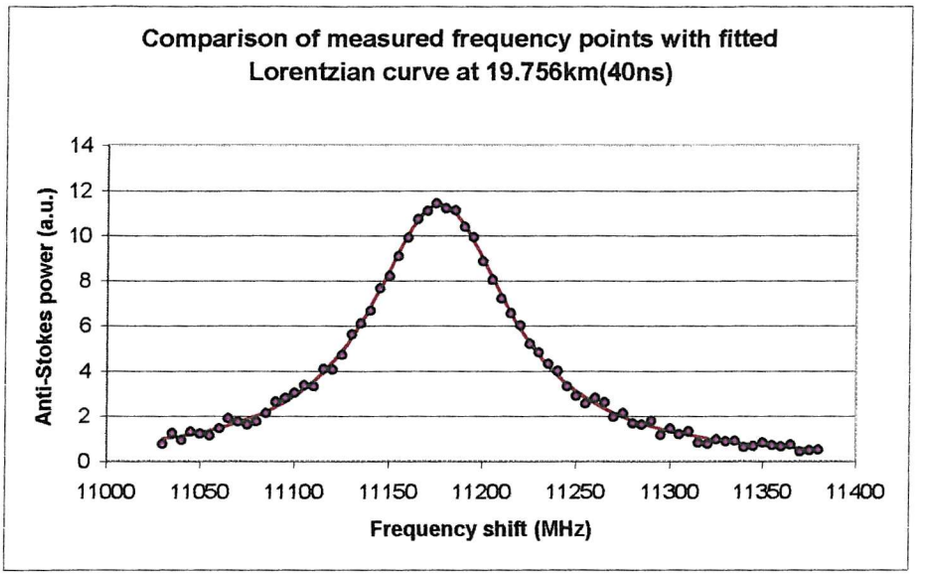

Figure 5.30 Anti-Stokes Linewidth Within Heated Region Together With Associated Lorentzian Line-Fit (40ns).

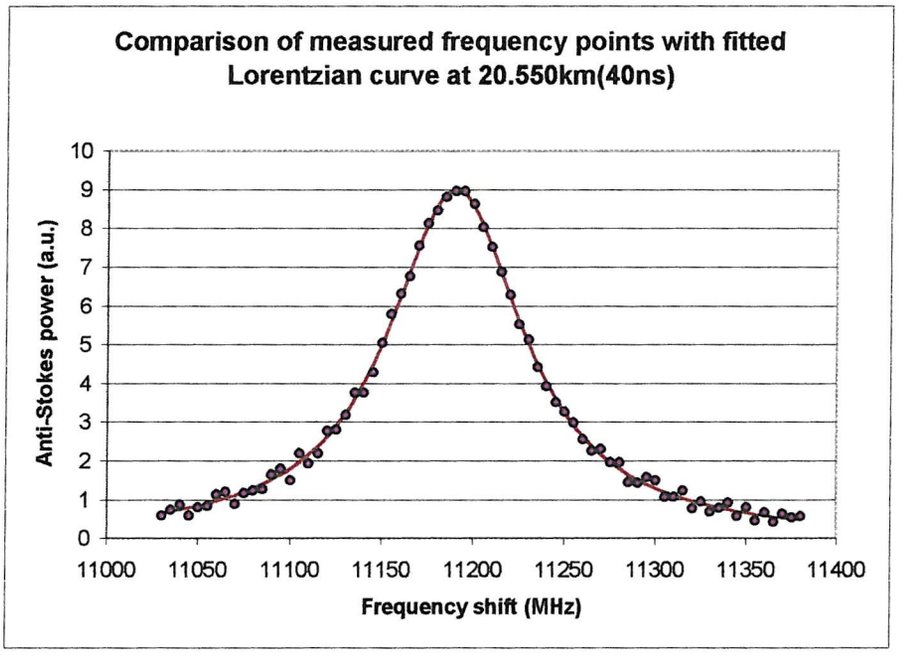

Figure 5.31 Anti-Stokes Linewidth Within Strained Region Together With Associated Lorentzian Line-Fit (40ns).

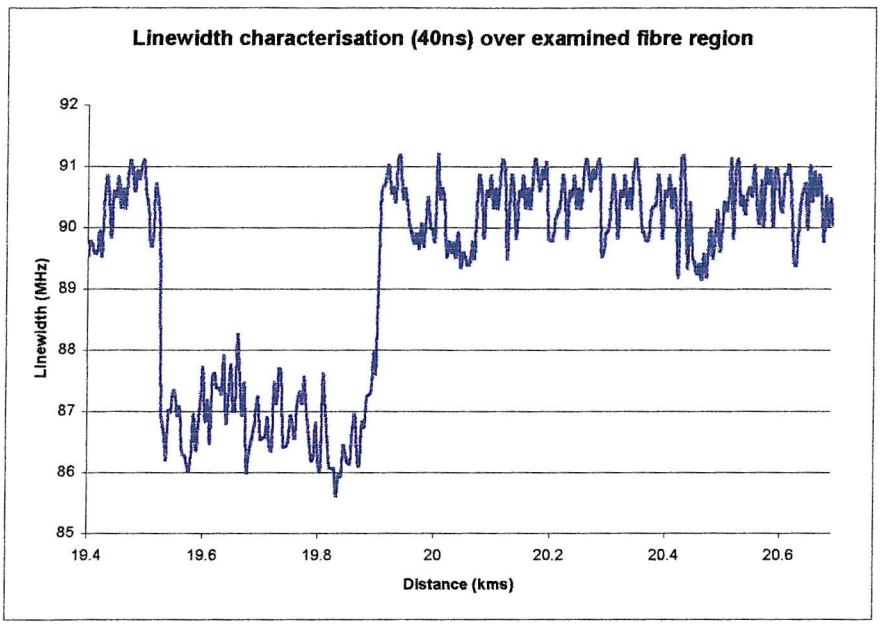

Figure 5.32 Change in Anti-Stokes Linewidth Along The Fibre Being Sensed (40ns).

Figures 5.33 and 5.34 below represent measurements of mean linewidth against temperature for a 100ns pulsewidth and 40ns pulsewidth respectively. The associated RMS errors are also included for each data point. Using linear regression, a line of best fit is placed on each graph with the results being that the 10m spatial resolution sensor demonstrates a reduction in linewidth with temperature of (–0.0677± 0.00488)MHz/K while the figure for the 4m spatial resolution sensor is (-0.0579±0.00299)MHz/K. This is a factor of 2 smaller than previous measurements made by Kurashima et al. in 1990 with values of –0.12MHz/K and –0.10MHz/K [6] and by previous research [1] with a value of –0.10MHz/K. This reduction in linewidth has been attributed to acoustic damping due to three-phonon interactions [7].

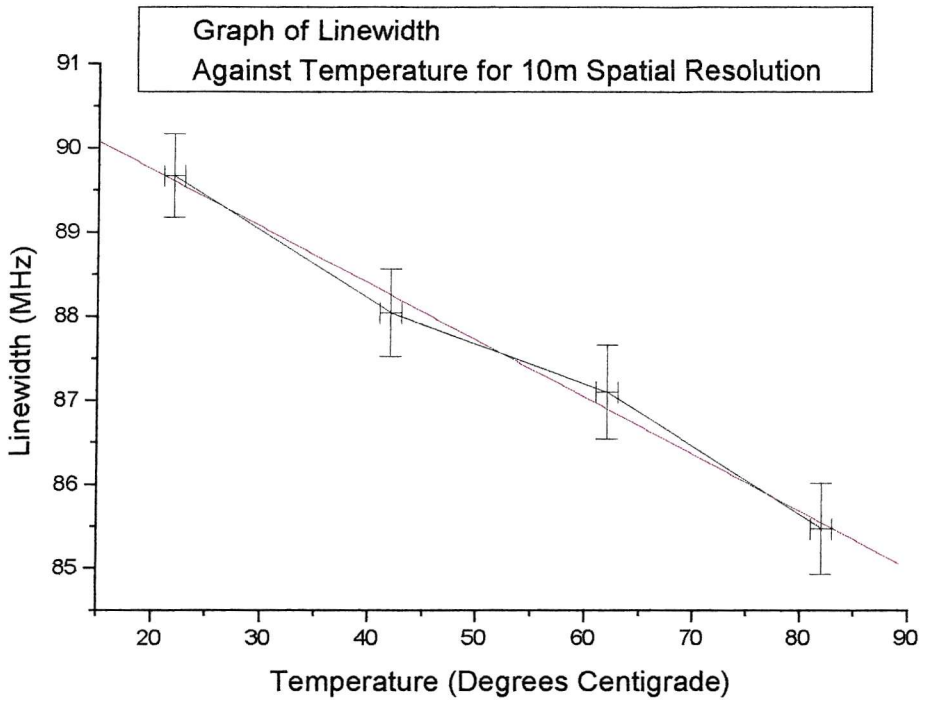

Figure 5.33 Anti-Stokes Linewidth vs Temperature (100ns).

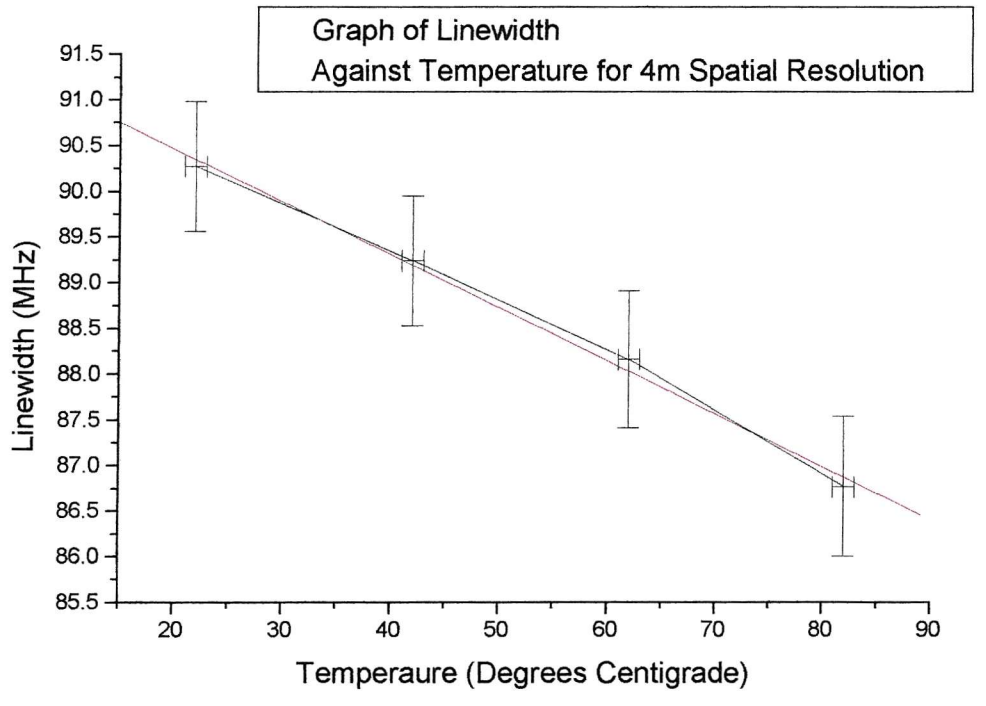

Figure 5.34 Anti-Stokes Linewidth vs Temperature (40ns).

5.8 Three-Dimensional Interpretation Of Results

The data used to generate the calibration curves can easily be adapted to give a three-dimensional interpretation of the sensing fibre results as shown in figures 5.35-5.38. In both spatial resolution cases the heated and strained sections are clearly distinct from the unheated and unstrained control sections of the fibre.

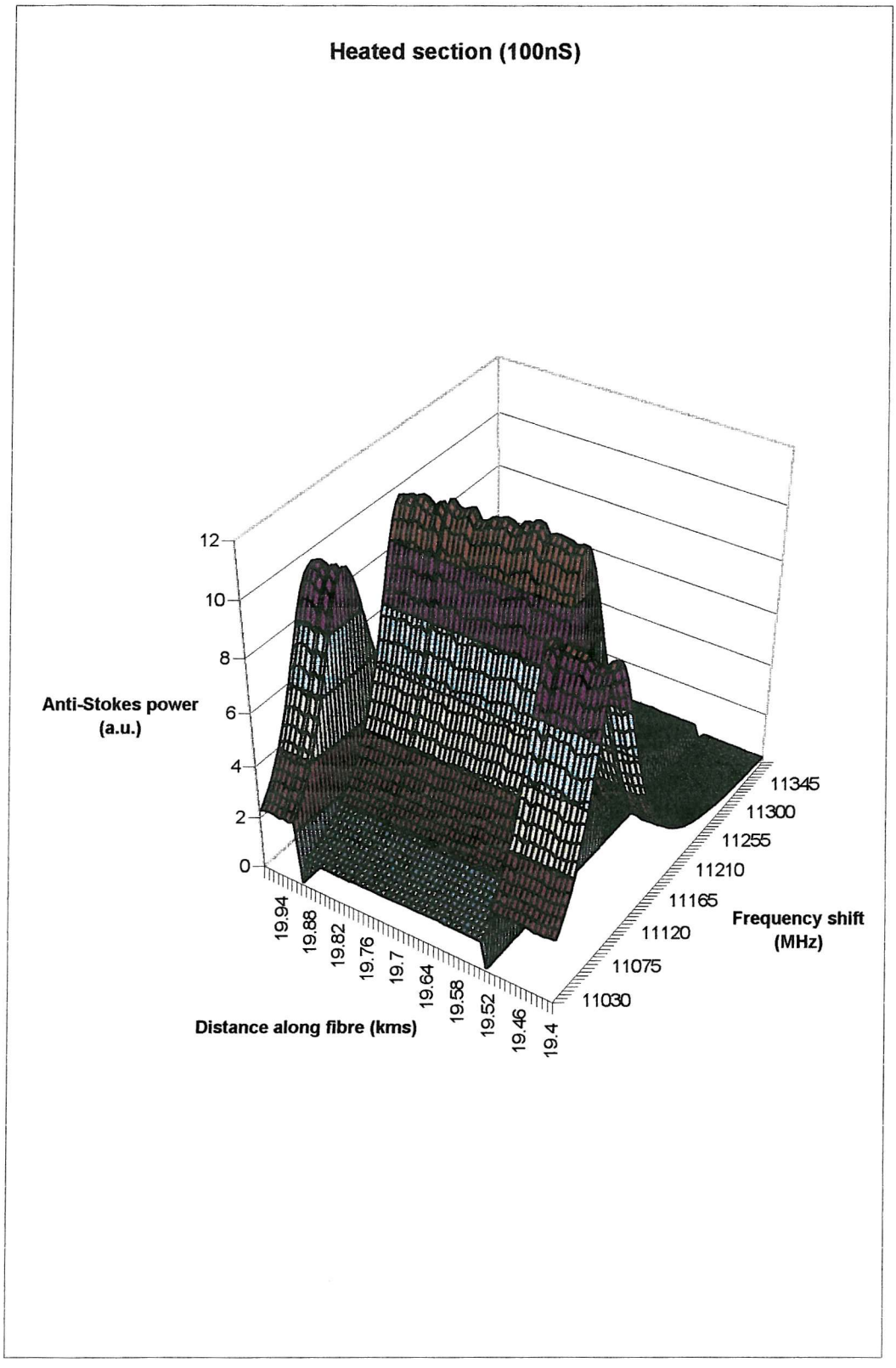

Figure 5.35 Three-Dimensional Representation Using 10m Spatial Resolution of the Anti-Stokes Spectrum at the Heated Section 19½ km Along the Sensing Fibre (Temperature at Heated Section is Ambient + 60K).

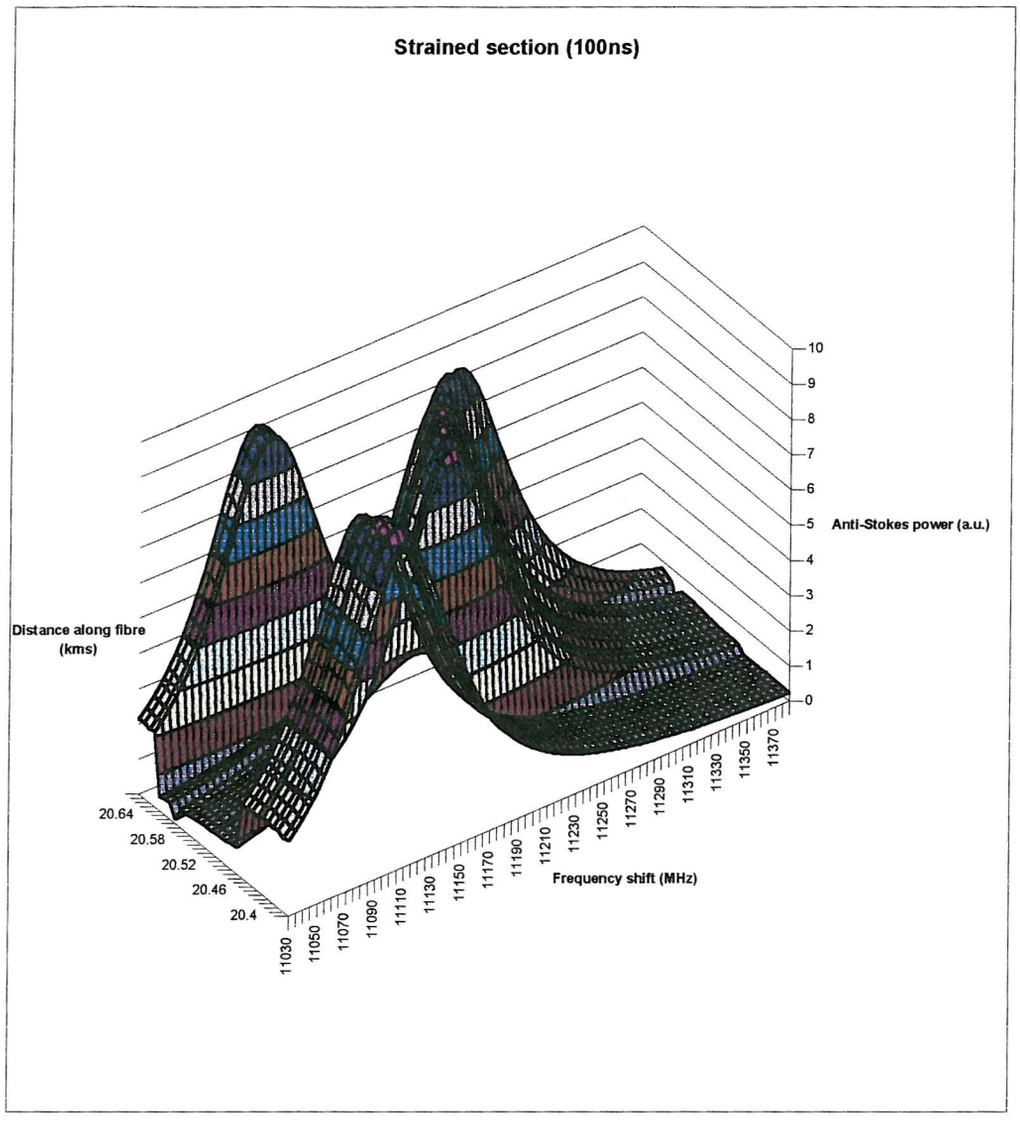

Figure 5.36 Three-Dimensional Representation Using 10m Spatial Resolution of the Anti-Stokes Spectrum at the Strained Section 20½ km Along the Sensing Fibre (Strain at Strained Section is 1935με).

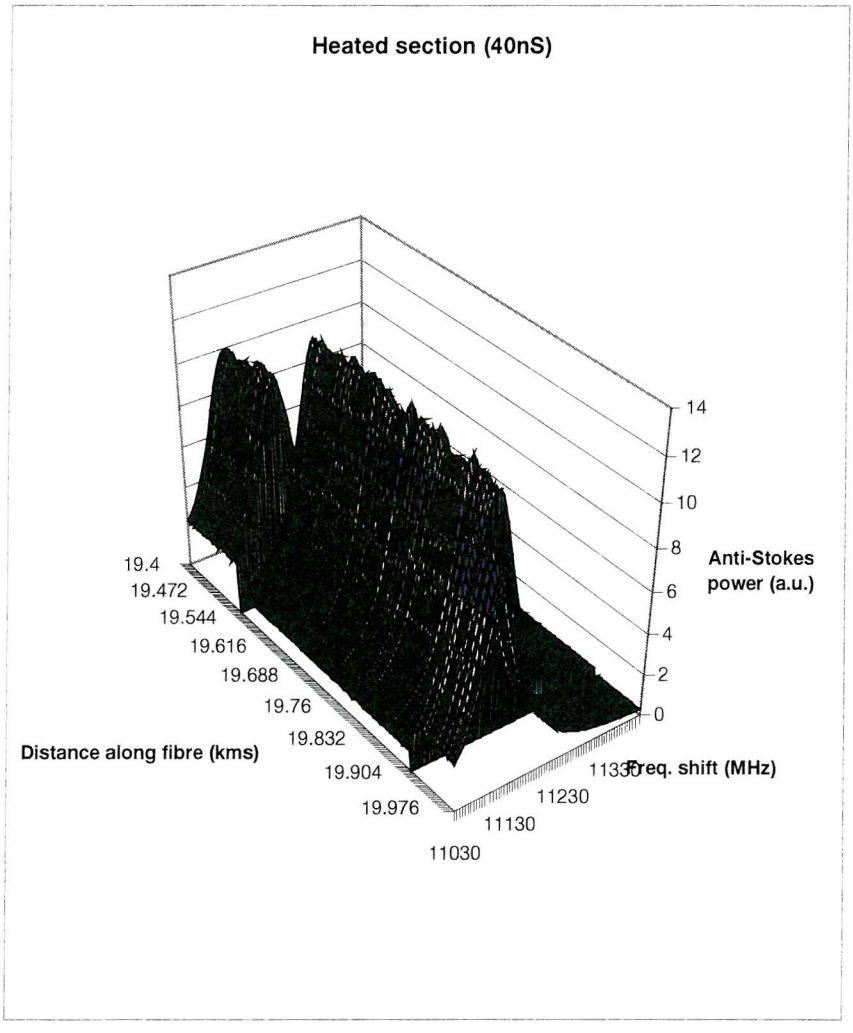

Figure 5.37 Three-Dimensional Representation Using 4m Spatial Resolution of the Anti-Stokes Spectrum at the Heated Section 19½ km Along the Sensing Fibre (Temperature at Heated Section is Ambient + 60K).

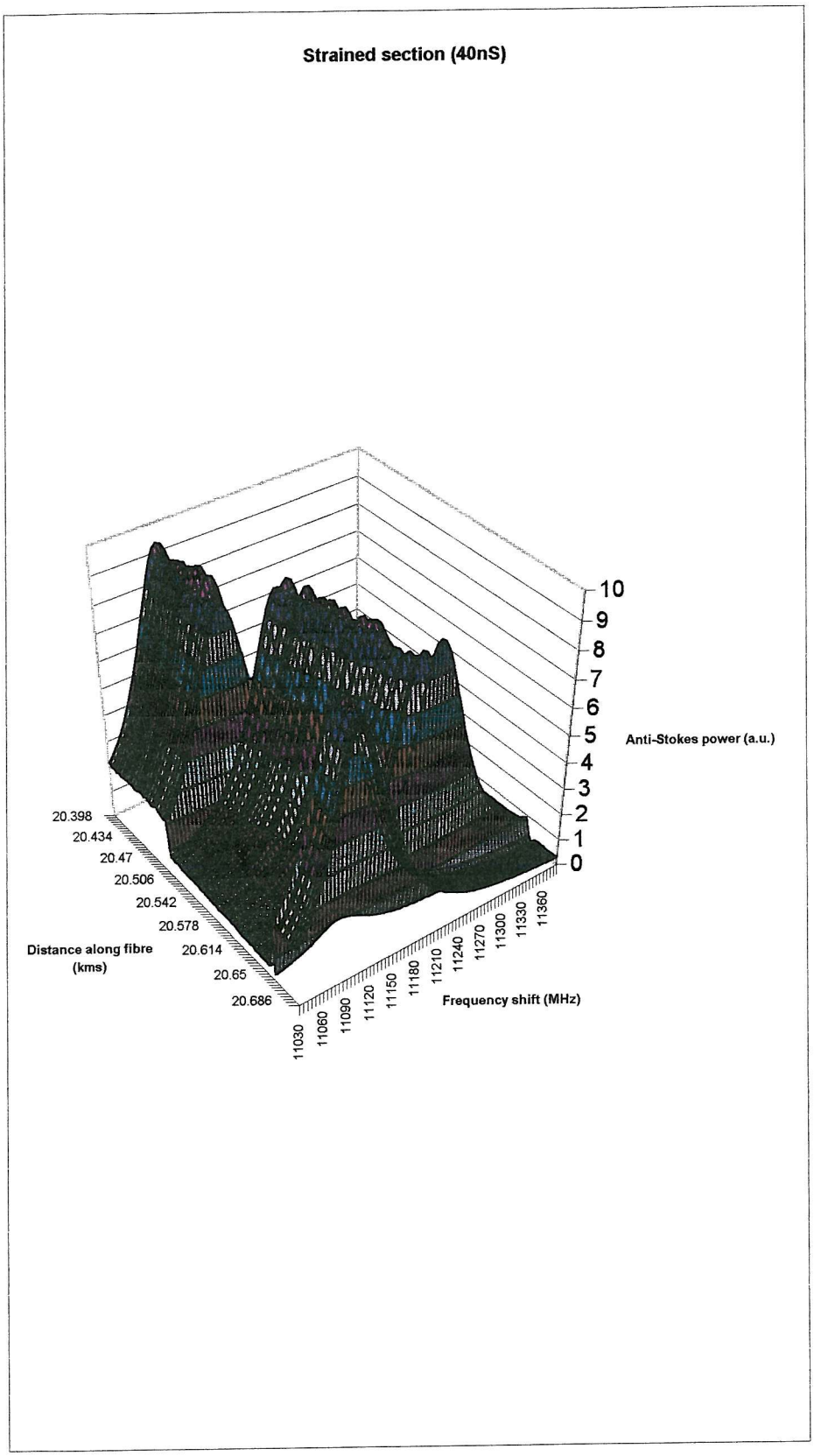

Figure 5.38 Three-Dimensional Representation Using 4m Spatial Resolution of the Anti-Stokes Spectrum at the Strained Section 20½ km Along the Sensing Fibre (Strain at Strained Section is 1935με).

5.9 Confirmation Of Spatial Resolution

Figures 5.39 and 5.40 demonstrate the spatial resolution for a 100ns pulsewidth and a 40ns pulsewidth respectively. The splice already mentioned at 20.3 km is highlighted in these figures and shows the spatial resolution of 10m and 4m using a Brillouin backscatter signal.

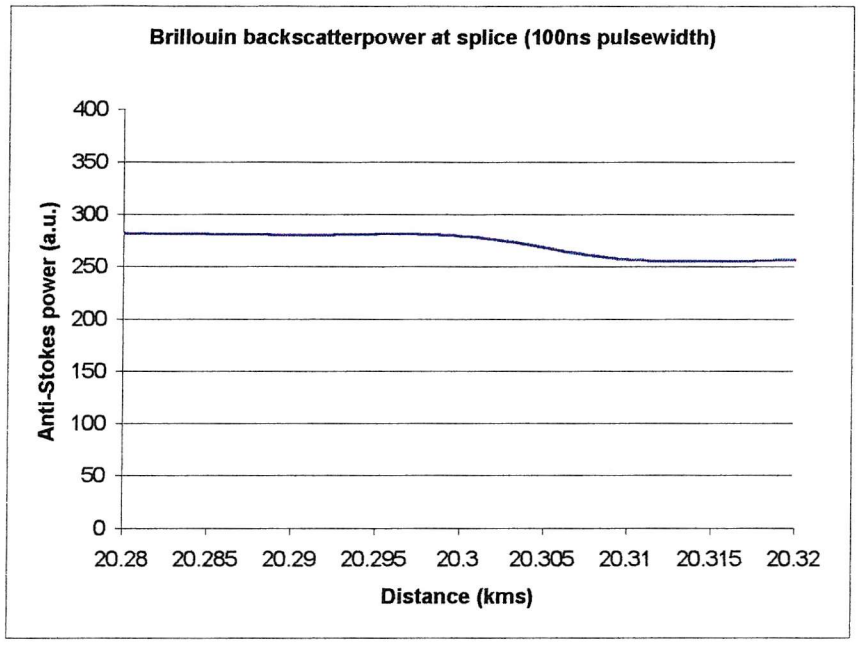

Figure 5.39 Graphical Representation of 10m Spatial Resolution.

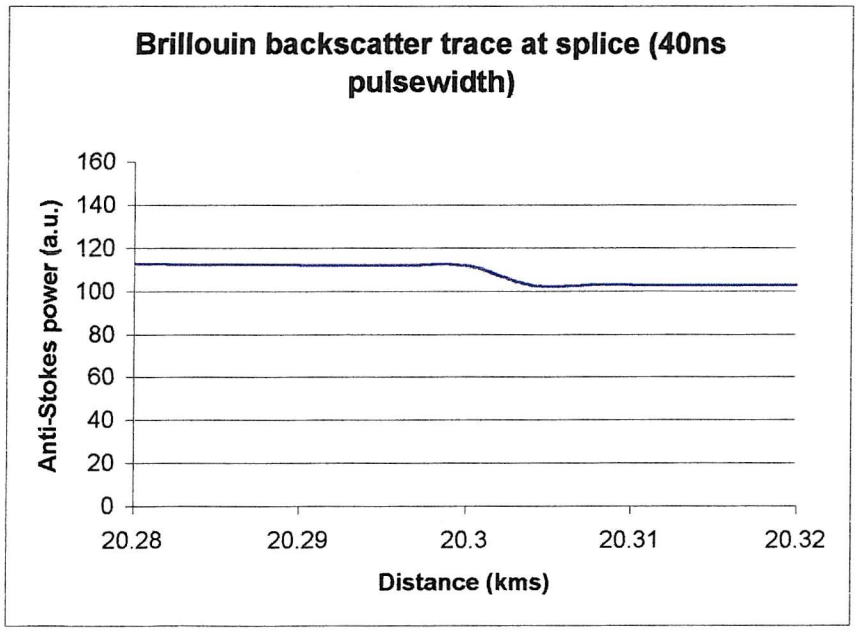

Figure 5.40 Graphical Representation of 4m Spatial Resolution.

Figures 5.41, 5.42, 5.43 and 5.44 show expanded plots of the Brillouin linewidth centre frequency and change in Brillouin intensity peak power and demonstrate 10m sensing and 4m sensing respectively.

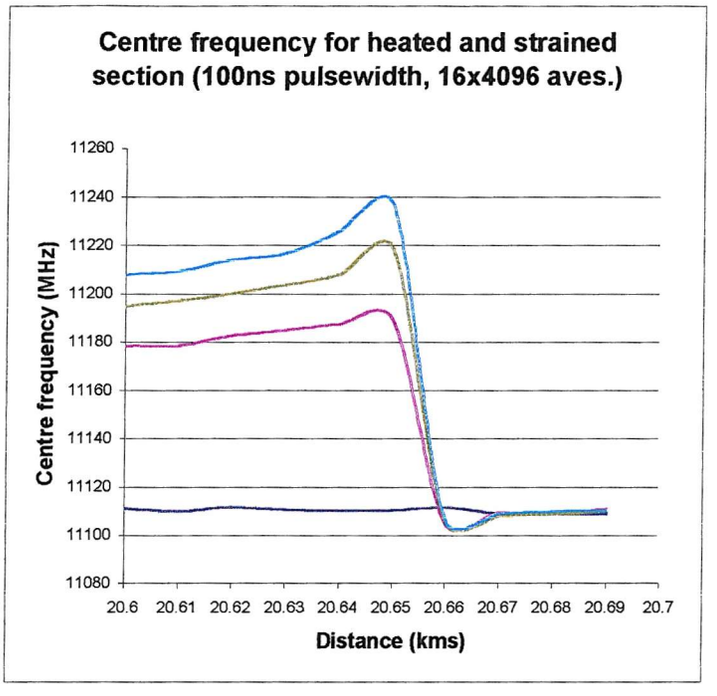

Figure 5.41 Graphical Representation of 10m Spatial Resolution Via Centre Frequency Measurement.

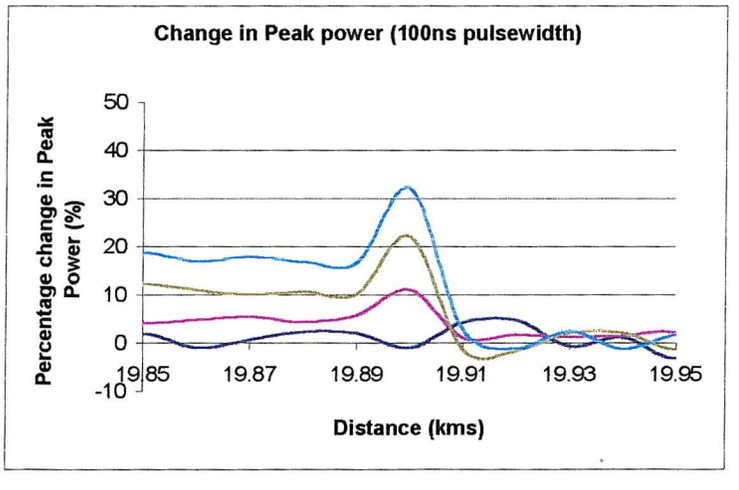

Figure 5.42 Graphical Representation of 10m Spatial Resolution Via Change in Peak Power Measurement.

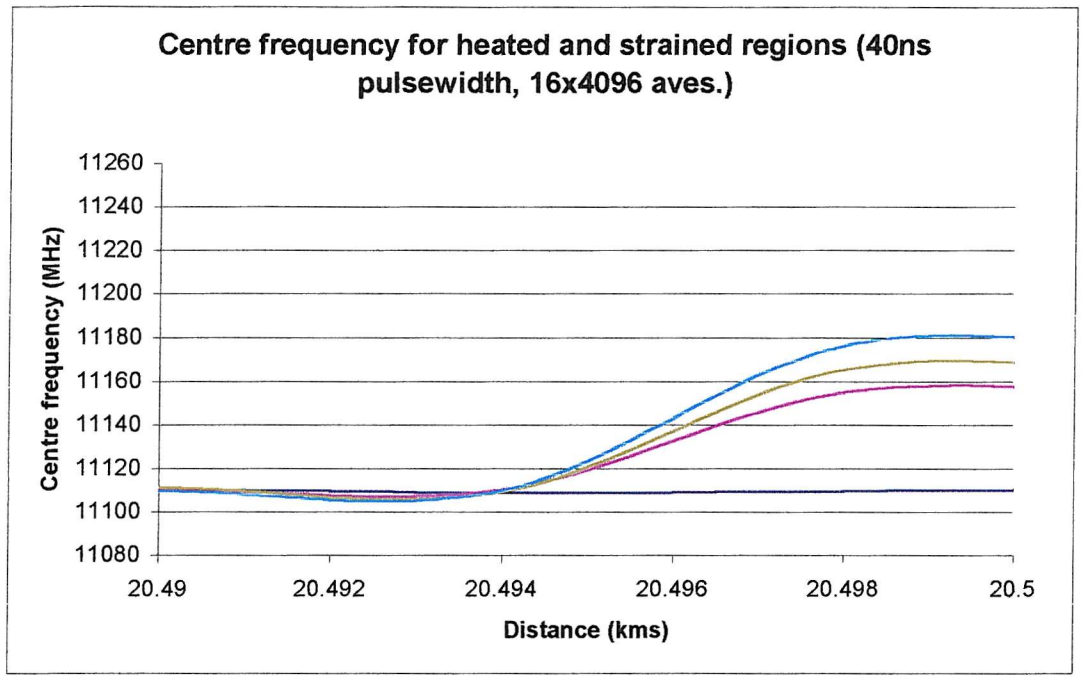

Figure 5.43 Graphical Representation of 4m Spatial Resolution Via Centre Frequency Measurement.

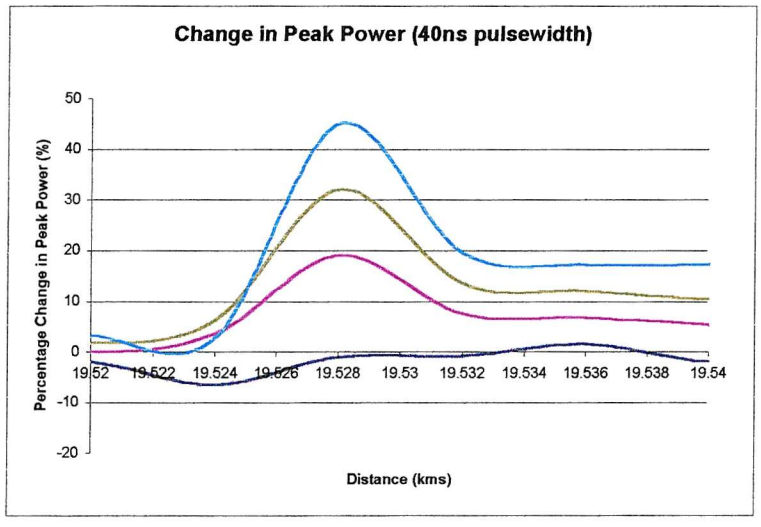

Figure 5.44 Graphical Representation of 4m Spatial Resolution Via Change in Peak Power Measurement.

5.10 Conclusions

This chapter has taken work in previous chapters and used this to show the development of a sensor with a final outcome being that simultaneous sensing results over a distance of 20kms have been detected and analysed.

The first part of this chapter has dealt with issues arising with the sensor before it has been deemed operational. This has included the development of a preamplifier within the optical section of the sensor together with a characterisation of the microwave section leading to a set of frequency-power scaling coefficients being developed.

A novel approach to obtaining a Rayleigh trace for normalisation of the anti-Stokes intensity data detected from the fibre section of interest has been demonstrated. Noise within the system has also been considered together with comparisons being made with modelled theory.

Following on from this, the sensor has been operated so as to demonstrate its ability to detect temperature and strain data with an improved spatial resolution to previous sensors of this type. The sensing has been centred on two sections 20km distant along the sensing fibre; one being heated in an oven while the other has been simultaneously strained using a system of pulleys and weights.

Respective temperature and strain resolutions of <7.3K and <190$\mu\varepsilon$ have been observed with the 10m spatial resolution sensor together with <9.5K and <240$\mu\varepsilon$ for the 4m spatial resolution sensor.

Calibration graphs of anti-Stokes frequency shift with temperature and strain have been obtained for both 10m and 4m spatial resolution using a curve fitting technique presented in previous work. Examples of the curve fitting process have been demonstrated for both spatial resolutions together with a graphical evolution of anti-Stokes linewidth with distance and temperature. Spatial resolution of the sensing that has taken place has been confirmed. Finally, three-dimensional representations of the data for both 10m and 4m spatial resolution have been generated and demonstrated

showing the effects of temperature and strain on the fibre in an easily identifiable manner.

Chapter Six takes the information generated in this chapter and subsequently draws conclusions from it.

5.11 References

[1] S.M. Maughan, 'Distributed Fibre Sensing Using Microwave Heterodyne Detection of Spontaneous Brillouin Backscatter', Doctor of Philosophy Thesis, Department of Electronics and Computer Science, *University of Southampton*, (September 2001)

[2] Agilent Inc., 'HPE4407B Specifications and Characteristics Manual', *Agilent Inc.*

[3] D.W. Marquardt, 'An algorithm for least-squares estimation of nonlinear parameters', *Journal of the Society for Industrial and Applied Mathematics*, Vol. 11, No.2, pp. 431-441, (June 1963)

[4] W.H.Press, S.A. Teukolsky, W.T.Vetterling and B.P. Flannery, 'Numerical Recipes in C- The Art of Scientific Computing' (Second Edition), *Cambridge University Press*, ISBN 0-521-43108-5 (1995)

[5] S.M.Maughan, Huai H.Kee and Trevor P.Newson, 'Simultaneous Distributed Fibre Temperature and Strain Sensor Using Microwave Coherent Detection of Spontaneous Brillouin Backscatter', IOP, *Measurement Science and Technology*, 12, pp. 834-842, (February 2001)

[6] T.Kurashima, T.Horiguchi and M.Tateda, 'Thermal effects of Brillouin gain spectra in single-mode fibers', *IEEE Photonics Technology Letters*, Vol.2, No.10, pp. 718-720, (1990)

[7] A.S.Pine, 'Brillouin Scattering Study of acoustic Attenuation in Fused Quartz', *Physical Review*, Vol. 185, No.3, pp. 1187-1193, (September 1969)

Chapter 6 Conclusions & Future Work

This chapter deals with summarising the results that have been taken in this research and comparing them with results obtained in prior work.
Finally, any improvements that could be made to the sensor are considered and included along with ideas for future work.

6.1 Summary & Conclusions

This research has been carried out with the principal objective of demonstrating that a novel approach to Brillouin backscatter detection can be applied to a distributed optical fibre sensor in order to improve the spatial resolution of subsequent detected data. This concept was based on removal of an electronic spectrum analyser, whose intermediate frequency bandpass filter effectively limted the spatial resolution to 20m, from a previous fibre sensor [1] and replacing it with purpose built microwave electronics in the form of a hybrid microwave superheterodyne receiver, a concept that is by no means new in terms of receiver design but, to the author's knowledge, new in that it has not been used in this way before.

This thesis has continued on from good progress made in the field of coherent detection of Brillouin backscatter in previous work conducted at the University of Southampton [1]. This previous research, however, only allowed for a limited spatial resolution to 20m hence necessitating the need for an appraisal and subsequent re-design of the sensor if this was to be improved upon. A set of coefficients were generated from this prior work pertaining to the effects of both temperature and strain on a length of telecommunications-standard optical fibre. As discussed within this thesis these coefficients determine the frequency shift of the anti-Stokes or Brillouin linewidth and the change in Brillouin backscatter intensity as functions of temperature and strain. With improved spatial resolutions of 10m and 4m having been observed using the microwave heterodyne receiver in the new fibre sensor design constructed in this thesis, table 6.1 allows for a comparison of the coefficients generated in previous work with those generated in the course of this research. RMS noise errors are also included in this figure as a useful guide to the performance of each sensor. Finally, the

derived temperature and strain resolutions are included so as to allow the overall performance of each sensor to be quantified.

	4m Spatial Resolution (140mW, 40ns Pulse Launched)	**10m Spatial Resolution (140mW, 100ns Pulse Launched)**	**20m Spatial Resolution (150mW, 200ns Pulse Launched) [1]**
Sensing Distance	20km	20km	27.4km
Data Averaging	65536	65536	12288
RMS Frequency Error on Temperature Measurement	±1.43MHz	±1.12MHz	±0.3MHz
RMS Intensity Error on Temperature Measurement	±3.3%	±2.3%	±1.56%
RMS Frequency Error on Strain Measurement	±1.43MHz	±1.15MHz	Not Given
RMS Intensity Error on Strain Measurement	±3.4%	±2.45%	±2.2% (Estimated)
$C_{vb\varepsilon}$	(0.048±0.0002)MHz/με	(0.048±0.0001)MHz/με	0.046MHz/ με
C_{vbT}	(1.11±0.1)MHz/K	(1.1±0.1)MHz/K	(1.07±0.06)MHz/K
$C_{Pb\varepsilon}$	(-0.0021±0.00023)%/με	(-0.0013±0.0002)%/με	(-0.0008±0.0005)%/με
C_{PbT}	(0.3±0.018)%/K	(0.30±0.01)%/K	(0.36±0.04)%/K
Derived Temperature Resolution	<9.5K	<7.3K	<4K
Derived Strain Resolution	<240με	<190με	<100με

Table 6.1 A Comparison of Coefficients Generated in This Thesis With Those From Previous Research.

where

$C_{vb\varepsilon}$=coefficient for change of Brillouin frequency shift with strain

C_{vbT} =coefficient for change of Brillouin frequency shift with temperature

$C_{Pb\varepsilon}$ =coefficient for change of Brillouin backscatter intensity with strain

C_{PbT} =coefficient for change of Brillouin backscatter intensity with temperature

The results in table 6.1 show that the new sensor compares favourably with its predecessor [1] in that measurements of strain and temperature have been readily obtained over a similar sensing distance and using a similar number of averages leading to a set of comparable frequency shift and intensity change coefficients with the derived strain and temperature resolutions being typically a factor of 2 worse. This could be attributed to a lower preamplification of 14dB being used in this thesis against 23dB previously although averaging was 5 times greater (65536) than previously used (12288). A 100ns pulsewidth would generate 3dB less Brillouin backscatter intensity than that seen for a 200ns pulsewidth used in [1] with a 40ns pulsewidth generating 7dB less backscatter intensity.

The results obtained in this research, as well as having improved on previous spatial resolutions obtained using coherent detection methods, do seem to agree well in value with those obtained in previous research conducted at the University of Southampton as well as with those from research using different detection techniques ($C_{vb\varepsilon}$=0.048MHz/με [2], C_{vbT} =1.1MHz/K [2], $C_{Pb\varepsilon}$ = -0.000903%/με [3], C_{PbT} =0.32%/K [4]).

Making use of the RMS errors found during the generation of figures 5.18, 5.19, 5.20, 5.21, 5.23, 5.24, 5.25 and 5.26 which are given in table 6.1, respective temperature and strain resolutions of <7.3K and <190με have been observed with the 10m spatial resolution sensor together with <9.5K and <240με for the 4m spatial resolution sensor, both over a sensing distance of 20km. Table 6.2 highlights the difference in temperature and strain resolutions between theoretically modelled and detected values.

Pulse power (mW)	Pulsewidth (ns)	Averages	Temperature Resolution, Strain Resolution (Modelled)	Temperature Resolution, Strain Resolution (Detected)
110	100	65536	±0.43K, ±140 με	Not Obtained
140	100	65536	±0.35K, ±110με	±7.3K, ±190με
140	40	65536	±0.6K, ±190με	±9.5K, ±240με

Table 6.2 Experimental Temperature and Strain Resolutions Using Modelled Theory and Detected Values for 20km Sensing.

The apparent worsening in temperature and strain resolution for detected values can be attributed to an over-simplified noise analysis in which local oscillator and Brillouin signal beat terms together with self-phase modulation have not been considered.

A comparison between modelled noise and that actually observed on the detected signal is made in table 6.3 for 20km sensing.

Pulse power (mW)	Pulsewidth (ns)	Averages	Noise (% of signal) (Theoretical)	Noise (% of signal) (Detected)
110	100	65536	0.13	Not Obtained
140	100	65536	0.1	2.45
140	40	65536	0.18	3.4

Table 6.3 Theoretical and Detected Noise for 20km Sensing Using the Microwave Heterodyne-Based Distributed Optical Fibre Sensor.

It can be observed from table 6.3 that the theoretically modelled noise is considerably lower than that actually seen during practical experimentation. This can be attributed once again to a rather over-simplified noise analysis whereby local oscillator and Brillouin signal beat terms together with self-phase modulation were not taken into consideration.

Previous research [1] has given self-phase modulation, which distorts the spectra, and four wave mixing of the higher narrow-band sensing pulse with residual ASE resulting in pump depletion, as limiting factors for the type of optical sensor used in this research using similar launch powers and pulsewidths. Neither of these non-linear effects, commonly seen as affecting frequency shift measurements disproportionately, has been observed during this thesis although it would be unwise to rule them out as limiting factors in this instance since neither had been considered during modelling and so were not being investigated before or during experimentation.

The new hybrid microwave heterodyne receiver design, as well as allowing for improved spatial resolution, also has two other distinct advantages over its predecessor.

The new receiver is totally modifiable in terms of changing the receiver bandwidth for various spatial resolutions due to its modular nature. It is also easily upgradeable as improved products can easily be interchanged with existing ones.

The rectified voltage obtained from the hybrid receiver was not squared for the analysis stage whereas previous work required this to be performed. This would save a considerable amount of data processing time for any large area optical fibre network analysis.

Previous research has detected an anti-Stokes linewidth of the order of 35MHz [1] through the use of a curve fitting algorithm mentioned in Chapter Five. Use of the same algorithm in this thesis has allowed for an anti-Stokes linewidth of the order of 90MHz to be observed. One theory to explain this is that of convolution of the bandpass filter used in the microwave receiver with the linewidth of the Brillouin backscatter signal. The intermediate frequency bandpass filter used in this thesis has a 3-dB bandwidth of 51MHz which together with a Brillouin full-width half-maximum linewidth of approximately 35MHz [1] would produce a convoluted Brillouin full- width half-maximum linewidth output of approximately 90MHz.

The explanation for the widened Brillouin linewidth output is demonstrated in figure 6.4.

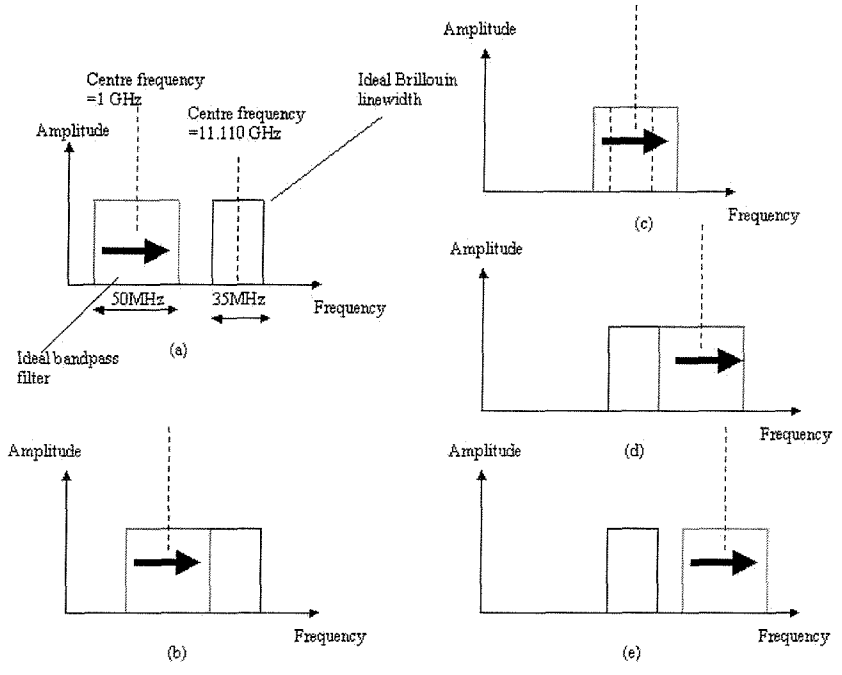

Figure 6.4 Process of Brillouin Linewidth Spectral Broadening Due to Bandpass Filter Function.

Figure 6.4 (a) shows an ideal bandpass filter function centred on 1GHz with a 50MHz bandwidth which is scanned across a 35MHz Brillouin linewidth centred on 11.110GHz in this instance, as is the case for no applied strain nor temperature, and which is represented as an ideal rectangular spectral form. Figure 6.4 (b), (c) and (d) demonstrate the movement of the filter as it scans across the Brillouin linewidth in the direction indicated and that the 1GHz intermediate frequency at the centre of the bandpass function 'sees' the Brillouin linewidth from when it is centred 25MHz (or half the filter bandwidth) below the lowest frequency of the Brillouin linewidth through to when the centre of the bandpass function is centred 25MHz (or half the filter bandwidth) above the highest frequency of the Brillouin linewidth. Figure 6.4 (e) completes the process by showing the bandpass filter having passed across the entire Brillouin linewidth spectrum.

This demonstrates how a spectrally broadened version of the optical Brillouin linewidth is observed at the output of the microwave receiver, the spectral broadening being equal to the bandwidth of the bandpass filter function. In the case of this thesis the 35MHz Brillouin linewidth [1] has been spectrally broadened by the 3-dB bandpass filter bandwidth of 51MHz to produce a Brillouin linewidth at the output of the fibre sensor of approximately 90MHz.

Summarising the linewidth characteristics of new and previous results produces table 6.5.

	4m Spatial Resolution (140mW, 40ns Pulse Launched)	**10m Spatial Resolution (140mW, 100ns Pulse Launched)**	**20m Spatial Resolution (150mW, 200ns Pulse Launched) [2]**
Sensing Distance	20km	20km	27.4km
Data Averaging	65536	65536	12288
Linewidth (Unheated)	(90.27±0.71)MHz	(89.67±0.5)MHz	35 MHz
Linewidth (Heated To Ambient + 60K)	(86.77±0.77)MHz	(85.47±0.54)MHz	Not Obtainable
$C_{\Delta bT}$	(-0.0579±0.0030)MHz/K	(-0.0677±0.0049)MHz/K	(-0.01)MHz/K

Table 6.5 A Comparison of Linewidths Observed in This Research With Those From Previous Work.

where

$C_{\Delta bT}$ is the coefficient of change in Brillouin linewidth as a function of temperature.

The values demonstrated through this research are in good agreement with those of previous research both at the university and in other establishments ($C_{\Delta bT}$ = -0.12MHz/K and –0.10MHz/K [5]).

One of the additional problems with improved spatial resolution sensing apart from that of less backscatter power being obtained due to a reduced sensing pulsewidth being launched is that of obtaining detectors fast enough to cope with the shorter time-varying intensity changes seen with the backscatter. Although the receiver used for Brillouin backscatter detection in this research has been able to cope adequately with this phenomenon, a novel approach using curve fitting techniques has been considered and utilised in order to obtain a Rayleigh trace for use in anti-Stokes intensity normalisation. This approach appears to have yielded some good results hence verifying its possibility of being incorporated in future work should fast enough optical detectors not be readily available.

6.2 Future Work

Apart from developing a better understanding of the bandpass transfer function dependence of the anti-Stokes linewidth observed as discussed in 6.1, many possibilities could be explored in terms of improving further still the spatial resolution or verifying the upgrade potential of the components that make up the new hybrid receiver. The sensing range of the sensor could also be improved by increasing the preamplification employed as, in this research, the idea behind the incorporated preamplifier was to merely nullify the loss along the optical return path of the detector.

One important area of the design that requires attention is the time taken in gathering useable data. The system that was used during this thesis was taking around 24 hours per temperature or strain setting in order to obtain useable data. One way of reducing this time would be to design an active scanning algorithm to allow the system to hone in on an anti-Stokes linewidth without the need to scan across a wide range of frequencies as was the case in this research. Another possibility would involve the use of reducing the dead time between backscatter being received and the next pulse being sent down the sensing fibre. Taking this idea to the extreme while assuming the same physical parameters as in this research,

Length of sensing fibre= 20km
Number of averages= 65536
Frequency scan range= 500MHz

Frequency step size=5MHz

Average velocity of light in the fibre = $2x10^8$ m/s

Hence time taken for pulse to travel down fibre and for backscatter to return= $2x10^{-4}$s

Hence time to take 65536 averages at one frequency assuming no time lost between receiving backscatter and sending next pulse= 13.1s

Hence time taken to scan 500MHz range in 5MHz steps= 1310s (approx. 22mins)

This is in effect the absolute limit for the minimum sweep time using the new sensor. The average velocity of light according to the average refractive index in the fibre is the fundamental limiting factor which dictates this minimum sweep time.

The packaged component nature of the hybrid receiver lends itself well to field-trialling, something that the previous receiver [1] has struggled with due to its bulkiness.

An ability to move out of laboratory conditions and into those of an outdoor environment while maintaining a good accuracy of temperature and strain sensing should prove conclusively whether the design covered in this thesis has a position in today's distributed optical fibre sensor market.

6.3 References

[1] S.M. Maughan, 'Distributed Fibre Sensing Using Microwave Heterodyne Detection of Spontaneous Brillouin Backscatter', Doctor of Philosophy Thesis, Department of Electronics and Computer Science, *University of Southampton*, (September 2001)

[2] T.R.Parker, M.Farhadiroushan, V.A.Handerek and A.J.Rogers, 'A Fully Distributed Simultaneous Strain and Temperature Sensor using Spontaneous Brillouin Backscatter', *IEEE Photonics Technology Letters*, Vol.9, No.7, pp.979-981, (1997)

[3] K.De Souza, P.C.Wait and T.P.Newson, 'Characterisation of Strain Dependence of the Landau-Placzek ratio for distributed sensing', *Electronics Letters*, Vol.33, No.7, pp 615-616, (1997)

[4] P.C.Wait and T.P.Newson, 'Landau-Placzek ratio applied to Distributed Fibre Sensing', *Optics Communications*, Vol.122, No.4-6, pp141-146, (1996)

[5] T.Kurashima, T.Horiguchi and M.Tateda, 'Thermal effects of Brillouin gain spectra in single-mode fibers', *IEEE Photonics Technology Letters*, Vol.2, No.10, pp. 718-720, (1990)